EES Catalysis

REVIEW ARTICLE

View Article Online
View Journal

Cite this: DOI: 10.1039/d5ey00306g

Alkali metal-doped g-C_3N_4: a multifunctional photocatalytic platform for solar-induced energy conversion and environmental restoration

Pratikshya Dash, Sulagna Patnaik, Sonali Panda, Bhagyashree Priyadarshini Mishra and Kulamani Parida *

Alkali metal doping has emerged as a powerful strategy to unlock the full photocatalytic potential of graphitic carbon nitride (g-C_3N_4) by modulating the structural and electronic parameters. Notably, incorporating alkali metal ions into the crystal lattice of g-C_3N_4 serves as an effective strategy to modulate its crystalline structure, enhance photon-harvesting capabilities, improve surface area, and optimize photocatalytic performance, all while retaining environmental compatibility. This review summarizes recent developments in alkali metal doping of g-C_3N_4, focusing on design strategies, structural modifications, and the resulting alterations in electronic and physicochemical properties. DFT calculations, theoretical modelling, and various characterization techniques were systematically reviewed for structural elucidation and optical modification after alkali metal ion doping in g-C_3N_4. We also provide concrete case studies by reviewing the structure–activity relationships of various alkali metal-doped g-C_3N_4-based photocatalysts having potential applications in artificial photosynthesis, ranging from solar fuel production, biomass conversion, organic transformation, and pollutant degradation to other miscellaneous applications, mainly supported by the in-depth photocatalytic mechanism. Finally, we conclude by highlighting the research gap and future perspectives. We believe this review is intended to serve as a comprehensive reference for both academic researchers and industrial practitioners engaged in the rational design of alkali-doped g-C_3N_4-based photocatalytic systems.

Received 26th October 2025,
Accepted 24th December 2025

DOI: 10.1039/d5ey00306g

rsc.li/eescatalysis

Broader context

The growing global energy demand and concerns over future energy security necessitate the transition toward sustainable alternatives such as semiconductor photocatalysis. This emerging approach enables solar-to-sustainability by harnessing artificial photosynthesis for next generation clean fuel production and environmental detoxification. Thus, the development of efficient, robust, and economically viable semiconductor photocatalysts derived from earth-abundant precursors is of paramount importance. In this review, we present a systematic evaluation of the emergence of alkali doping in g-C_3N_4, which has attracted considerable attention owing to its low cost, non-toxicity and sustainable and straight-forward synthesis approach. We critically examine and provide a comprehensive assessment of the incorporation of various alkali metal ions such as, Li^+, Na^+, K^+ *etc.*, into the interlayer cavities or lattice sites of the g-C_3N_4 framework, which induces significant structural, electronic, and optical modulation to accelerate charge carrier separation for efficient solar fuel production and environmental detoxification. Besides, this review also highlights the existing research gaps and future prospects in the advancement of semiconductor photocatalysis, ultimately contributing to the development of sustainable energy technologies for energy and environment security. We believe this review systematically addresses the synthesis–structure–activity correlations and can be an effective guiding tool for dopant selection in the fabrication of g-C_3N_4-based next-generation photocatalysts.

1. Introduction

The global energy demand is anticipated to increase exponentially, as a consequence of rapid advances in industrialization and population expansion, with projections indicating a 2-fold rise by 2050 relative to the present consumption scenario.[1–3] Concurrently, CO_2 emissions due to the overexploitation of fossil fuels pose a serious threat to global warming and need immediate intervention. Achieving carbon neutrality depends on promoting eco-sustainability and advancing renewable energy technologies. In the contemporary era, achieving sustainable development necessitates the adoption of clean and renewable energy technologies to mitigate escalating environmental challenges. Among

Centre for Nano Science and Nano Technology, Institute of Technical Education and Research, Siksha 'O' Anusandhan University, Bhubaneswar-751030, India.
E-mail: kulamaniparida@soa.ac.in, paridakulamani@yahoo.com;
Fax: +91 674 2350642; Tel: +91 674 2351777

diverse energy alternatives, solar energy has become a leading contender owing to its inexhaustibility and renewable nature for meeting future global energy needs.[4–6] Due to its potential as an environmentally sustainable solution for global energy challenges, solar energy production has attracted considerable research attention.[7,8] Solar fuel production, a critical aspect of solar energy utilization, focuses on converting abundant feedstocks into valuable chemical fuels. More broadly, the utilization of solar energy towards various artificial photosynthesis applications represents a broader framework by harnessing the renewable precursors to drive essential photochemical reactions. This encompasses solar fuel production (mainly emphasizing processes like H_2 production, CO_2 reduction, H_2O_2 synthesis, and N_2 fixation), alongside other ancillary applications such as organic and inorganic pollutant degradation, biomass conversion, organic transformations, and NO_x removal.

Semiconductor-based heterogeneous photocatalysis has garnered widespread research interest in the current era due to its potential to harness solar energy efficiently.[9–11] Considerable efforts have been made by the researchers to design advanced semiconductor-based photocatalysts to enhance their potential applications.[12–14] An ideal semiconductor photocatalyst must possess (i) a strong absorption of light across a broad spectrum, (ii) abundant surface-active sites to facilitate reactions, (iii) suppressed recombination of charge carriers to prolong their lifetime, (iv) appropriate CB and VB potentials to drive redox reactions, and (v) low-cost fabrication along with long-term photostability.[15,16] To date, a good number of semiconductor-based photocatalytic materials have emerged to address energy issues and environmental threats.[17–20] Amongst these photocatalysts, g-C_3N_4 stands out as a prominent choice and has been extensively studied due to its advantageous features such as cost-effectiveness, metal-free, easy and facile fabrication, robustness, visible light responsiveness, and suitable band edge potential for surface redox reactions.[21,22] Despite meeting several essential criteria for an efficient photocatalyst, pristine

Pratikshya Dash

Pratikshya Dash completed her MSc degree in Chemistry at Sambalpur University, Sambalpur, Odisha, India. She qualified GATE 2021. She is currently pursuing her PhD under the supervision of Prof. Kulamani Parida at the Centre for Nano Science and Nano Technology (CNSNT), Institute of Technical Education and Research (ITER), Siksha 'O' Anusandhan (Deemed to be University). Her current research interests are focused on the development of mesoporous graphitic carbon nitride-based nanomaterials for solar energy conversion applications.

Sulagna Patnaik

Dr Sulagna Patnaik completed her master's degree in chemistry at NIT, Rourkela. Then, she joined as a lecturer in chemistry at Rayagada Autonomous College, Odisha. She is presently working as a reader at the Maharshi College of Natural Science, Odisha, and completed her PhD at Siksha 'O' Anusandhan University, Bhubaneswar, Odisha. Her research work is focused on the development of modified g-C_3N_4-based photocatalysts for hydrogen energy production and pollution abatement.

Sonali Panda

Sonali Panda holds an MSc degree in Chemistry from Utkal University, Bhubaneswar and is a University Gold Medalist. She has qualified with both the GATE and CSIR-UGC NET. Currently, she is a research scholar under the supervision of Prof. Kulamani Parida at the Centre for Nano Science and Nano Technology (CNSNT), Institute of Technical Education and Research (ITER), Siksha 'O' Anusandhan (Deemed to be University). Her research focuses on the design and development of multi-metallic MOFs for sustainable energy conversion applications.

Bhagyashree Priyadarshini Mishra

Dr Bhagyashree Priyadarshini Mishra received her MSc degree from Ravenshaw University, Odisha, India. She completed her PhD at Siksha 'O' Anusandhan University, Odisha, where she worked in the field of photocatalytic hydrogen evolution and H_2O_2 production. She joined the research group of Prof. Venkata Krishnan in 2024 as a post-doctoral researcher under the National Postdoctoral Fellowship (NPDF) 2024. Her current research focuses on the development of effective photocatalysts for nitrogen fixation applications.

g-C_3N_4 often suffers from intrinsic drawbacks such as sluggish charge separation, limited surface-active sites, low specific surface area, poor electrical conductivity, and modest redox potential, which restrict its performance in photocatalytic and electrocatalytic processes. As a result, rational modification strategies have become central to unlocking its potential in sustainable energy conversion and environmental remediation. Among the various modification pathways, such as elemental doping, defect engineering, heterojunction construction, surface functionalization, nano-structuring by increasing porosity and surface area, non-metal/carbon doping, vacancy engineering, and single-atom loading, alkali-metal doping (Li^+, Na^+, K^+, Rb^+, and Cs^+) has gained particular attention.[23–25] In this regard, we have recently reported a review article highlighting that the strategic nano-structuring can expose the isolated active sites for better photocatalytic activity. Moreover, the structural modification strategies, such as elemental doping, further aid the promotional impact by optimizing the microstructure and optoelectronic properties.[26,27] Doping serves as an effective strategy to introduce foreign elements into the g-C_3N_4 lattice, enabling modulation of its surface and electronic features. The introduction of metallic or non-metallic dopants alters the band gap energy and tunes the band edge potential, thereby broadening the light absorption, enhancing photocurrent generation, and modifying photo-reactivity.[28–30] Due to its adaptability for flexible *in situ* doping approaches and favorable biocompatibility, ion doping has been extensively studied to engineer g-C_3N_4-based heterostructures.[31–33] In the case of anionic doping, the introduced species typically occupy either substitutionally or interstitially, which can modulate both the textural and electronic structures. In contrast, cationic dopants induce orbital hybridization between the dopant's atomic orbital and the g-C_3N_4 molecular orbital, which leads to achieving the optimized VB and CB positions.[34–37] Cationic dopants can further modify the electronic properties by band gap narrowing, improving light harvesting efficiency and accelerating the charge carriers' mobility. Common cationic dopants include alkali, transition, and noble metals, which impart distinctive physicochemical functionalities and strengthen surface interactions in the doped system. This doping is readily achieved through thermal polymerization or condensation, wherein the g-C_3N_4 precursors are simply mixed with the appropriate metal salts, either in the solid-state mixture or in solution-based systems, to obtain uniformly doped systems.[31–37]

Alkali metal cations interact strongly with the heptazine nitrogen framework, creating local electronic perturbations that are difficult to achieve through heavier dopants or structural modifications alone. Their incorporation can widen interlayer spacing, enhance π-electron delocalization, and promote charge polarization, collectively leading to improved charge separation and more efficient migration of photo-generated carriers. Moreover, alkali-metal doping frequently induces subtle structural distortions and introduces shallow donor states, which modulate the band structure without significantly compromising chemical integrity. These effects can shift the conduction and valence band positions to better match key redox reactions relevant to water splitting, CO_2 reduction, nitrogen fixation, pollutant oxidation, and antibacterial disinfection. In some cases, small cations (*e.g.*, Li^+) also facilitate proton or ion transport at the catalyst interface, which is beneficial for hydrogen-evolution and proton-coupled reactions. The presence of alkali metal ions can also tune surface basicity and adsorption behaviour, thereby facilitating the activation of molecules such as O_2, H_2O, and CO_2, while the modulated band potentials promote the formation of reactive intermediates during the photocatalytic processes.[26,38]

Alkali metal doping offers several advantages, such as environmental benignity and low toxicity. Incorporating these ions introduces structural vacancies or defects within the lattice, which strategically alter electronic properties. The specific choice of dopant and its concentration further influences charge distribution dynamics, mitigates photo-corrosion, and governs overall catalytic performance. Furthermore, alkali-doped g-C_3N_4-based intercalated systems induce non-uniform charge distribution, thereby suppressing electron–hole recombination and amplifying charge separation efficiency. They are also extensively recognised as effective electronic promoters in various catalytic applications due to their exclusive properties.[39–44]

Collectively, these structural and electronic modifications explain why alkali-treated g-C_3N_4 often shows a higher photocatalytic activity than the pristine material. For instance, Sun *et al.* demonstrated a facile thermal polymerization method to fabricate K^+ doped g-C_3N_4 for efficient rhodamine B degradation, which is attributed to the small grain size, dispersed active sites, intensified optical response in the visible spectrum, and lowered band gap due to the K^+ doping.[42] Similarly, a systematic investigation of various alkali metal ion (Li^+, Na^+, or K^+)

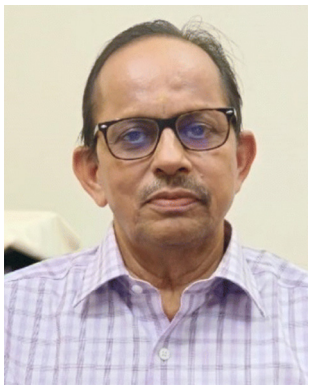

Kulamani Parida

Prof. Kulamani Parida is a globally distinguished scientist in the areas of materials science, catalysis and nanotechnology. He superannuated as a Chief Scientist and a Professor of Academy of Scientific and Innovative Research (AcSIR) at CSIR-IMMT, Bhubaneswar in 2014. His adoration for chemistry and passion for research couldn't let Prof. Parida to sit idle after retirement. With the same devotion and dedication, Prof. Parida (Director) started the 'Centre for Nano Science and Nano Technology', a research unit of Siksha 'O' Anusandhan (deemed to be university), Bhubaneswar. His research interests include the design and development of advanced materials encompassing fine chemicals, energy generation/storage, and environmental applications. He has published more than 550 research articles and review articles in renowned international journals. He has a citation count of 39593 to his credit with an h-index of 108 and i10-index of 489. For more details: https://kmparidaimmt.weebly.com/.

doped g-C_3N_4 systems revealed that they exhibited stronger absorption in the visible region, larger surface area for exposed active sites, and reduced band gap, which cumulatively optimized the microstructure and optoelectronic features for efficient hydrogen production.[45] Haripriya *et al.* demonstrated that the appropriate alkali metal (Li, Na, and K) doped g-C_3N_4 can control the defect densities, achieving an optimized band structure for efficient photocatalytic H_2O_2 production.[46] Moreover, the co-doping of alkali metals with other photoactive species can also lead to promotional activity in photocatalysis. For instance, Liang *et al.* developed Bi and K co-doped g-C_3N_4, which demonstrated enhanced visible light harvesting capability and improved band alignment by shifting the conduction band towards more negative energy levels, facilitating the photocatalytic oxygen reduction reaction.[47] Moreover, the co-doping reduces the energy barrier for redox reactions by improving the charge transfer process. Alkali metal-containing g-C_3N_4 systems can also form effective composite photocatalysts with other photoactive species and regulate the crystallinity, microstructure, and charge dynamics in the composite photocatalyst. Also, dual and multi-functional behaviour can be achieved, which is beneficial for the complex photocatalytic reactions.[24,38,48] The effective interfacial contact in the alkali-doped g-C_3N_4-based composite can significantly boost the charge transfer process to enable efficient redox reaction by complete utilization of maximum charge carriers.[49,50] The synthesis of alkali metal-doped catalysts neither requires post-synthesis purification steps nor relies on hazardous chemicals; therefore, it is regarded as an inherently sustainable process. The impact of alkali metal ion doping on the structural, morphological, and electronic properties in the case of other photocatalytic materials, such as titanates, is well established in the literature. Bem *et al.* demonstrated that the substitution of H^+ ions by Na^+ results in contraction of the inter-layer distance of titanate nanotubes.[51] Furthermore, Qamar and co-workers elucidated the stabilizing effect of studied Na^+ ions on the titanate framework.[52] Even doping of sodium ions has also been reported to drive a structural phase transformation from layered titanate to anatase.[53]

In the literature, several review articles mainly focus on the prevailing aspects of synthesis methodologies, structural modifications, and various photocatalytic applications of doped g-C_3N_4 systems. For instance, a recent review article written by Khan *et al.* focused on the recent advancements in metal and non-metal doped g-C_3N_4, comprising the fundamentals, photocatalytic mechanisms, and factors affecting photocatalysis due to the doping and co-doping.[26] Similarly, another recent review article also demonstrated the effect of s-block, p-block, and transition metal dopants on the crystal structure of g-C_3N_4 to achieve the optimal band alignment for better light harvesting phenomena.[29] Our group also demonstrated the role of anion doping in modulating the band edge potential and simultaneously highlighted the various effective synthesis strategies, nature of dopants, and doping sites in g-C_3N_4 for energy- and environment-related applications.[54] Similarly, a few more reviews have been reported in the literature, mostly focused on the overall doping phenomena in the g-C_3N_4 structure.[26,28,55,56] Nonetheless,

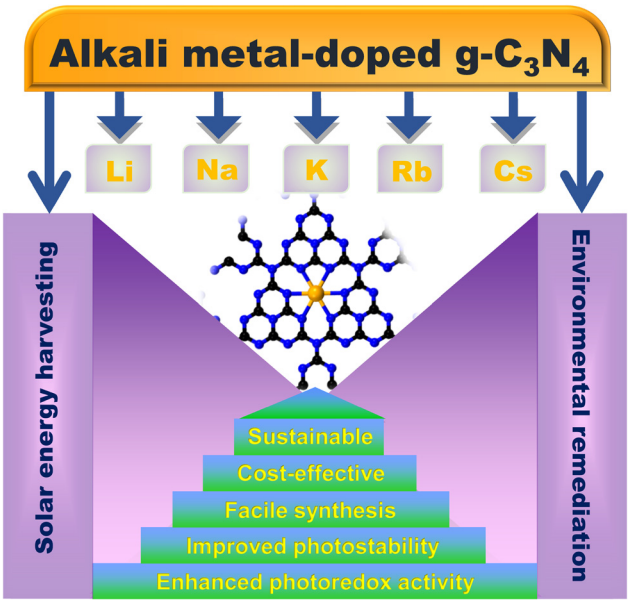

Fig. 1 Schematic illustration of alkali-doped g-C_3N_4 highlighted with characteristic features towards energy conversion and environmental remediation.

systematic and comprehensive studies that explicitly rationalize the effect of alkali metal doping on the photocatalytic activity of the g-C_3N_4 crystal lattice still remain underexplored to date. The advent of alkali metal-doped g-C_3N_4 has revolutionized the field of g-C_3N_4 structural modifications by imparting novel physicochemical properties. Therefore, this review systematically summarizes the comprehensive assessment of how alkali metals influence the physicochemical, optoelectronic, and structural attributes of g-C_3N_4 photocatalysts for various efficient artificial photocatalytic applications. We further discuss the criteria for selecting appropriate alkali metals to rationally design high-performance alkali-doped g-C_3N_4 photocatalysts. The performance of these alkali-doped g-C_3N_4 systems across diverse artificial photosynthesis applications, such as solar fuel production, biomass conversion, organic transformation, pollutant degradation, and other miscellaneous applications, has been systematically reviewed using various characterization techniques, DFT calculations, and in-depth mechanistic analyses. Fig. 1 presents various alkali metal dopants incorporated in the g-C_3N_4 lattice matrix, developed *via* an economical, sustainable, and facile approach leading to enhanced structural and optical modulation, improved photostability, and superior redox reactivity for diverse energy harvesting and environmental remediation applications. Overall, this review aims to provide a key fundamental reference for researchers who are focused on advancing alkali metal-doped g-C_3N_4 materials for efficient and sustainable solar energy conversion.

2. Alkali metal-doped g-C_3N_4

Alkali metal-ion doping is a facile, non-interfering strategy that upgrades nearly any g-C_3N_4 modification approach and can

Table 1 Comparative assessment of alkali doping over heterojunction construction, non-metal doping, and single-atom catalysis

Criteria	Alkali-metal doping	Heterojunction	Non-metal doping	Single-atom catalysts
Synthesis complexity	Very simple, (impregnation/ thermal treatment)	High (requires precise interface engineering)	Moderate	Very high (atom trapping, complex supports)
Cost effectiveness	Low-cost alkali salts; inexpensive processing	High (multiple materials + step-wise fabrication)	Low-moderate	Very high (noble metals, advanced synthesis)
Electronic structure tuning	Strong modulation of charge density *via* ionic/ electrostatic effects	Strong but interface-dependent	Moderate; depends on substitution sites	Excellent, but limited to isolated atoms
Defect/active site creation	Easily generates oxygen vacancies, cyano defect and surface basicity	Depends on junction quality	Creates substitutional defects	Creates highly active isolated sites but fewer in number
Scalability	Highly scalable industrially	Limited scalability; complex architectures	Good	Challenging, delicate synthesis
Stability under reaction conditions	Good thermal/chemical stability	Interface may degrade	Generally stable	Stability of isolated atoms is often problematic (migration/sintering)
Environmental concerns	Minimal	Depends on materials used	Minimal	Possible issues with metal leaching

significantly resolve the limitations of the bulk g-C_3N_4 (Fig. 6). It provides a unique combination of cost-effectiveness, ease of synthesis, enhanced interlayer spacing, precise electronic tuning, and internal-field-driven charge separation. It is completely distinguishable from more complex and expensive methods like heterojunction construction, non-metal doping, or incorporation of a single-atom catalyst (Table 1).

Various alkali metal ions (Li^+, Na^+, K^+, *etc.*) preferably intercalate into the nitrogen pot of the g-C_3N_4 framework, cause a distinct modification in the electronic band structure, create defects and vacancies, and improve the crystallinity for efficient photocatalysis. The charge redistribution in the interlayer of pristine g-C_3N_4 is absolutely necessary to achieve improved photocatalysis, which can be carried out by intercalating the alkali metal ions into the intrinsic graphitic sp^2-hybridized network composed of tri-*s*-triazine units.[39,57,58] For example, Li *et al.* unraveled the crucial role of the interlayer electron transfer mechanism for alkali metals (K, Rb, and Cs) intercalated in carbon nitride (CN).[59] The doping of alkali metals could inhibit random charge transfer across the CN planes in order to enable the directional flow of electrons (e^-) between the adjacent layers. Consequently, the alkali metal intercalation facilitates the charge redistribution within the crystal lattice, thereby effectively enhancing the charge carrier separation to execute efficient redox reaction. Nguyen and co-workers demonstrated that incorporating single alkali metal dopants into g-C_3N_4 can reduce its vertical ionization potential and increase the electron affinity and Lewis acidity. Furthermore, the alkali-doped g-C_3N_4 systems possessed a lower band gap relative to the undoped g-C_3N_4, which is due to the electron donation from the metal atom to g-C_3N_4.[60] We first discuss the theoretical modelling and DFT calculations, which elucidate the preferred doping sites of alkali metals within the g-C_3N_4 lattice and the resulting changes in electronic band structure. Additionally, we systematically reviewed the design strategies to incorporate alkali metals and the characterization techniques used to probe the induced structural modifications. Moreover, the influence of doping on the electronic properties is also comprehensively reviewed. The doping can create localized charge densities to promote the superior charge carrier mobility; thus, the CB and VB levels adjust and realign for efficient photo redox reaction. The appropriate alkali doping also tends to increase the surface basicity of the g-C_3N_4, promoting the easy activation and adsorption of the organic molecules/reactants for the efficient photocatalytic reactions. Furthermore, the beneficial aspects of co-doping can further induce the defect-mediated active sites by promoting N vacancies in g-C_3N_4.[61–63] Overall, alkali metal doping can introduce additional electronic states, reduce the band gap energy, and induce a redshift in the absorption edge, thereby enhancing light-harvesting efficiency in the visible-light region. Therefore, this section delves into a more detailed analysis of the crystal and lattice parameters of alkali doped g-C_3N_4 in terms of DFT and theoretical investigations, reviews the promising and economic design strategies, highlights the optoarchitecture behavior of g-C_3N_4, and the effect of co-doping (Fig. 2).

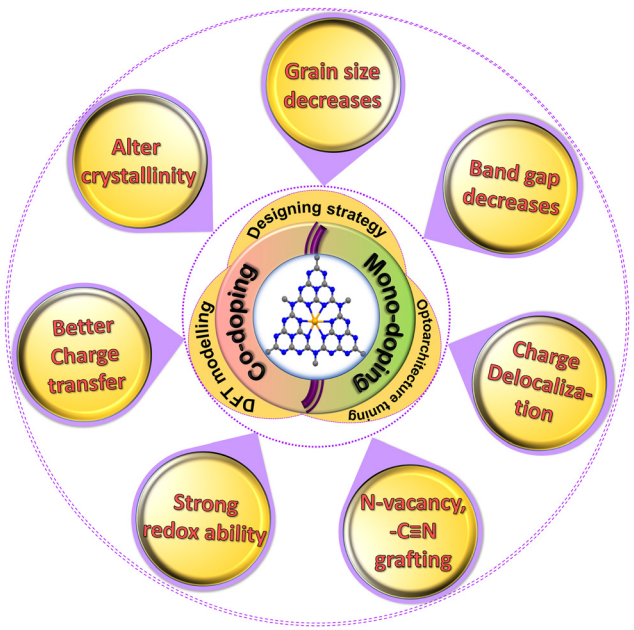

Fig. 2 Schematic illustration of the effect of alkali-doping in the g-C_3N_4 matrix.

2.1. DFT calculations and theoretical modelling to unveil the effect of alkali metal doping within the g-C_3N_4 matrix

As discussed above, the incorporation of alkali metals in the g-C_3N_4 framework induces notable variations in its micro-electronic structure, which was analyzed using the plane-wave ultrasoft pseudopotential simulations. The energy states of the configurations were estimated by the generalized gradient approximation (GGA) and local density approximation (LDA) methods.[64] The alkali metal ions are preferably incorporated in the large cavity, designated as the F position over other possible binding sites designated as A, B, C, D and E in g-C_3N_4 layers (Fig. 3a). Furthermore, the DFT calculations estimated the formation energy, charge transfer, bandgap energy and related work function values, which suggested the creation of the n-type Schottky junctions at the interface of g-C_3N_4 and the alkali metals (Table 2). Moreover, the band edge potential and the corresponding band structure were significantly altered due to the redistribution of HOMO and LUMO energy levels after the alkali metal doping.

Alkali metals preferably adopt interstitial doping rather than substitutional doping, due to their comparatively larger ionic radii relative to C and N atoms. For example, Xiong *et al.* presented a DFT calculation using the "Vienna *ab initio* simulation package" (VASP5.3), and the most stable configuration of K and Na-doped g-C_3N_4 (CN-K2 and CN-Na2, respectively) was determined using the PBE exchange–correlation functional, used within the spin-polarized GGA method.[39] Despite the analogous chemical nature of K and Na atoms, they impart distinct charge distribution within the CN framework. Moreover, the interplanar spacing in CN is sufficient to host alkali metal atoms, enabling their incorporation *via* ion–dipole interaction. DFT calculations suggested that the Na-atom has an almost negligible effect on the crystal structure due to its small atomic radius (1.86 Å) and confined within the planar cavity of CN; however, K-atoms with a relatively larger atomic radius (2.32 Å) are intercalated within the interlayer of CN, forming a bridging connection that enhances the interlayer charge transport efficiency. Moreover, the distance of the nitride cavities oriented at the centre of the nearest heptazine moieties and the interlayer spacing of CN were found to be 7.11 and 3.14 Å, respectively. Therefore, the most stable optimized crystal structure of CN is that obtained by the interstitial doping of Na in CN-Na2 and the interlayer insertion of K in CN-K2, as shown in Fig. 3b–f.

Table 2 Calculated formation energy, charge transfer, theoretical band gap, and work functions for different alkali metal-doped g-C_3N_4 photocatalysts

Dopant	Formation energy (eV)	Charge transfer Δq (e)	Band gap (eV)	Work function (eV)
Li–g-C_3N_4	−4.477	+0.09	0.74 (GGA-PW91) 0.59 (LDA-CAPZ)	5.94
Na–g-C_3N_4	−4.144	+0.75	0.78 (GGA-PW91) 0.61 (LDA-CAPZ)	5.57
K–g-C_3N_4	−3.603	+1.26	0.82 (GGA-PW91) 0.65 (LDA-CAPZ)	5.32

Thereafter, Nnadiekwe *et al.* demonstrated an in-depth theoretical investigation of the band structure of alkali-doped g-C_3N_4 systems.[65] Optimization of the bulk g-C_3N_4 and the alkali metal ion-doped g-C_3N_4 (Li^+–g-C_3N_4, Na^+–g-C_3N_4, and K^+–g-C_3N_4) sheets was carried out using the B3LYP hybrid functional. Furthermore, structural geometries and electronic interactions between g-C_3N_4 and the alkali metal ions were optimized using Pople's split valence 6-31G(d) and the LANL2DZ basis sets, respectively. It is obvious that the alkali metal cation, when doped in g-C_3N_4, can lead to a change in the structural properties and experience a change in the chemical and electronic features. The optimized geometries of the pristine g-C_3N_4, M^+(Li^+, Na^+, and K^+)–g-C_3N_4 are

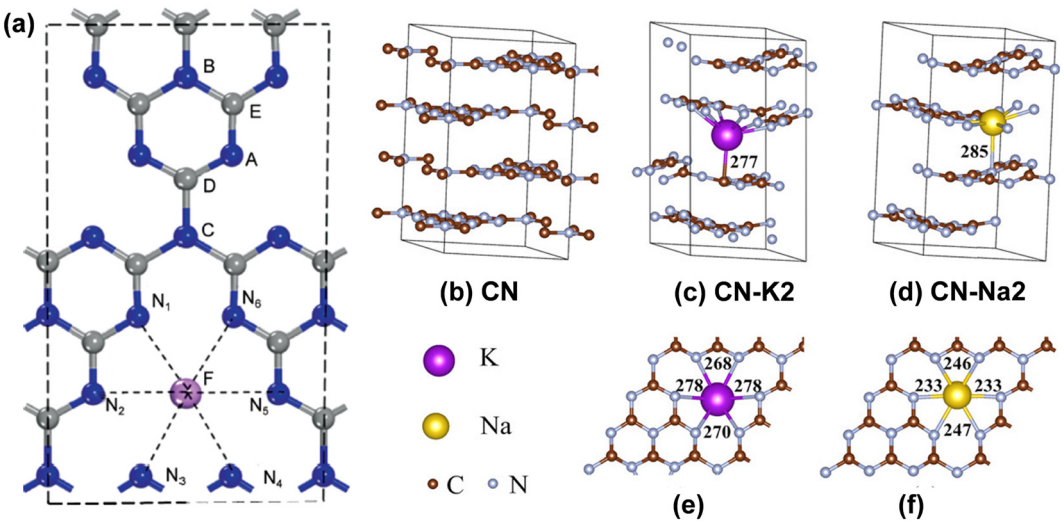

Fig. 3 (a) Top views of the six doped configurations of alkali metals adsorbed on g-C_3N_4. Reproduced with permission from ref. 64. Copyright 2016, Elsevier. Crystal structures of CN (b), CN-K2 (c), and CN-Na2 (d). (e) and (f) Top views of CN-K2 and CN-Na2. Reproduced with permission from ref. 39. Copyright 2016, American Chemical Society.

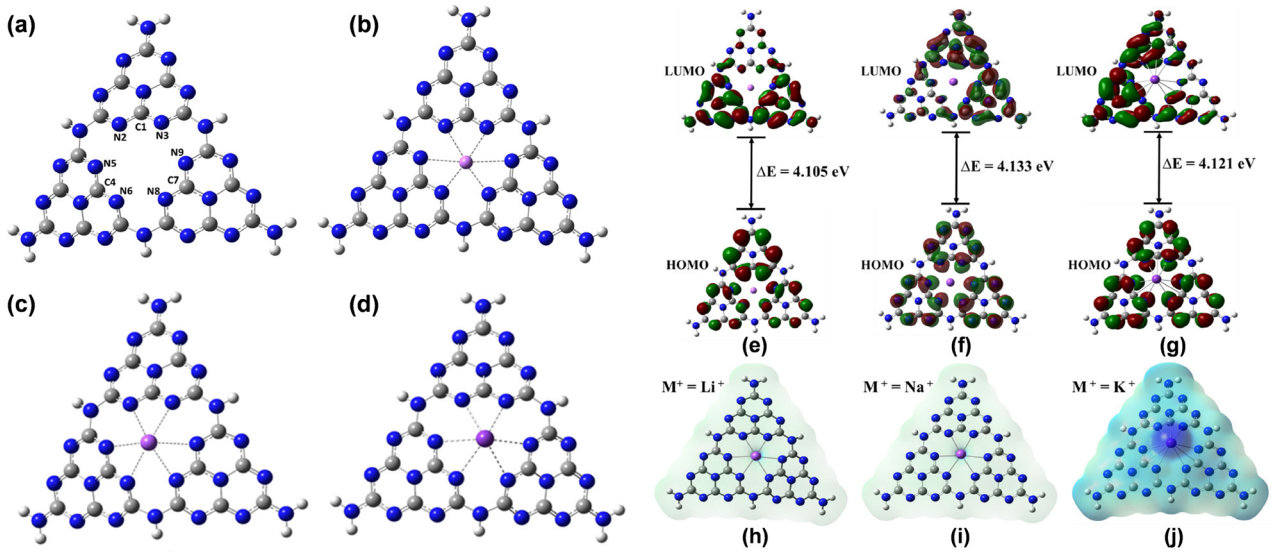

Fig. 4 Illustration of the optimized configuration of (a) g-C_3N_4, (b) Li^+–g-C_3N_4, (c) Na^+–g-C_3N_4, and (d) K^+–g-C_3N_4, calculated frontier molecular orbitals and electrostatic charge surface distribution of Li^+–g-C_3N_4 (e) and (h), Na^+–g-C_3N_4 (f) and (i), and K^+–g-C_3N_4 (g) and (j). Reproduced with permission from ref. 65. Copyright 2023, Elsevier.

presented in Fig. 4a–d. It is understood that the unit cell having central voids is appropriate to host the alkali metal ion. Various structural properties, such as the bond lengths and bond angles in the N–M^+–N vicinity of alkali metal ion-doped g-C_3N_4, were estimated to comprehend the types of interaction between the alkali metal ion and electron-rich nitrogen atoms. However, the calculation results revealed that the M^+–N distance increased in the order Li^+–g-C_3N_4 < Na^+–g-C_3N_4 < K^+–g-C_3N_4, but the N–M^+–N angles of Li^+–g-C_3N_4 and Na^+–g-C_3N_4 complexes did not differ remarkably. In contrast, K^+–g-C_3N_4 exhibited different characteristics with a longer M^+–N bond, which caused a noticeable distortion in the planarity of g-C_3N_4 sheets. The electronic configuration was analyzed by calculating and optimizing the frontier orbital arrangements of the HOMO and the LUMO. It was reported that the K^+ ion could slightly delocalize the LUMO due to the different structural properties. In contrast, the electron-deficient nature of Li^+–g-C_3N_4 can be understood from the charge distribution maps, suggesting the lowest HOMO–LUMO energy gap with maximum charge potential, compared to Na^+–g-C_3N_4 and K^+–g-C_3N_4, respectively (Fig. 4e–j).

Zhang *et al.* demonstrated an in-depth DFT calculation to estimate the electronic structure of bulk g-C_3N_4 (CN) and K^+ doped g-C_3N_4 (KCN).[66] Band structures, density of states, work functions, and Fermi levels of CN and KCN were determined by the CASTEP module analysis method using the Materials Studio software. The structure optimization was achieved by generalized gradient approximation (GGA) and the Perdew–Burke–Ernzerhof (PBE) functional analysis. An optimized structure of CN and KCN is demonstrated in Fig. 5a, suggesting the intercalation of K^+ in the heptazine cavity of the cyano-bonded CN structure. Furthermore, the total and partial density of states (TDOS and PDOS) of CN and KCN are presented in Fig. 5b and c, suggesting that the VB maxima of CN and KCN are predominantly contributed by N 2p orbitals, whereas the CB minima are constructed by the contribution of C 2p and N 2p orbitals. However, the K doping in KCN modified the CB minima, leading to a noticeable variation in the band gap. Furthermore, the work function and Fermi level of CN and KCN were estimated by GGA-PBE functional simulation. The lower wavefunction and higher Fermi level value of KCN relative to CN suggested that the intercalation of K^+ facilitates the formation of abundant photoexcited charge carriers for better photocatalytic reaction (Fig. 5d and e). Zhu *et al.* synthesized triazine-based Li-doped g-C_3N_4 derived *via* the thermal condensation of melamine.[67] Owing to the relatively small dimension of the nitride cavities, Li-atoms more preferably accommodate as single atoms rather than forming clusters. Furthermore, GCMC simulations were employed to obtain the optimized configuration of Li-doped g-C_3N_4. DFT simulation revealed Li-N bond lengths ranging from 1.82 to 2.01 Å. However, the co-existence of N–N and Li–N bonds exerted repulsive as well as attractive interactions, respectively, thereby suffering the crystal distortion within the g-C_3N_4 framework.

2.2. Design strategies of alkali metal-doped g-C_3N_4

The design principle of g-C_3N_4 with alkali metal-doping includes a cost-effective, sustainable, single-step co-condensation approach, generally utilizing hydroxides or halides of corresponding alkali metal ions as primary dopant sources.[39–41,68–70] Conventionally, the N-rich precursor of g-C_3N_4 and the chosen alkali metal source are calcined together under controlled heating to synthesize the alkali metal-doped g-C_3N_4. In some instances, disodium ethylenediaminetetraacetate (2Na-EDTA) can also be used to achieve both the Na doping and the additional C, N source to modify the CN framework.[71] The doping mechanism is strongly governed by the ionic radius of the dopant. Small alkali cations (Li^+ and Na^+) preferentially occupy intralayer cavities, forming strong interactions with heptazine units. This interaction generates localized

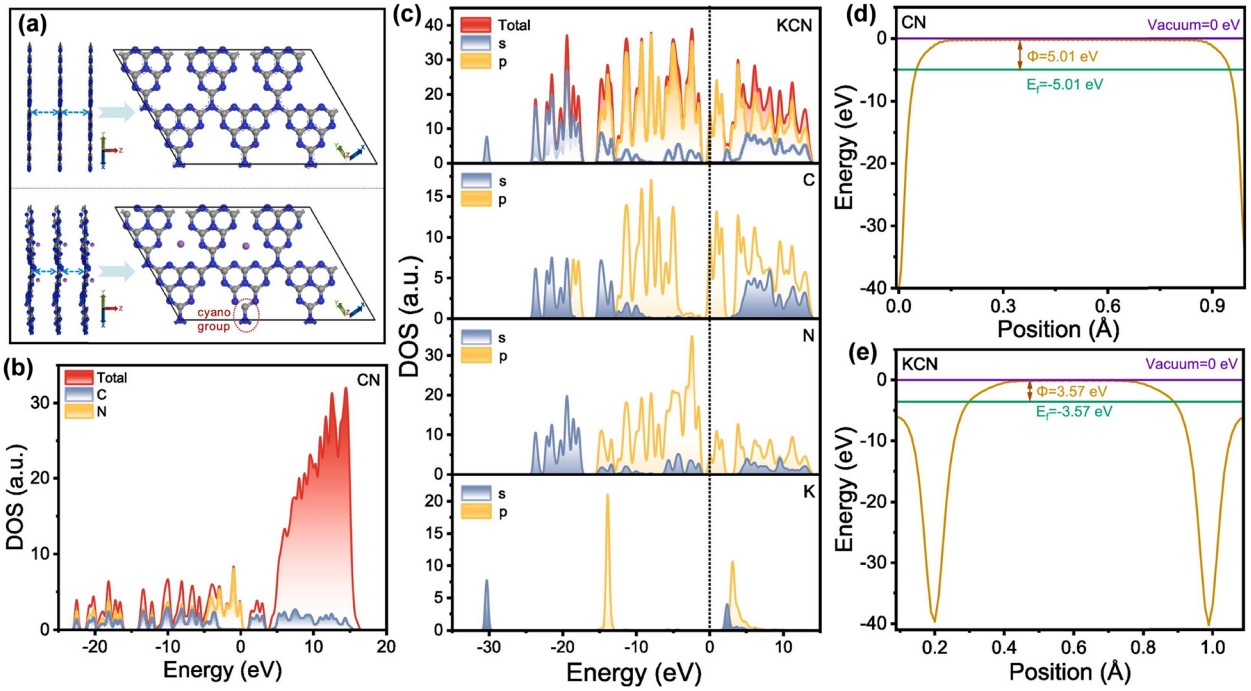

Fig. 5 Theoretical representation of (a) interlayer and in-plane crystal structures, electronic density of states (b) and (c), and electrostatic potential distribution (d) and (e) of CN and KCN. Reproduced with permission from ref. 66. Copyright 2024, Elsevier.

polarons, enhancing charge carrier mobility and electronic conductivity. In contrast, larger ions (K^+ and Cs^+) are incorporated into interlayer spaces, acting as structural bridges that facilitate interlayer charge transport, promoting exfoliation and intercalation. The incorporation of alkali metal ions within the g-C_3N_4 framework can occur *via* two possible ways, as shown in Fig. 6: (i) co-condensation of alkali metal salts (KCl, $KHCO_3$, KBr, LiOH, *etc*) with N-rich precursors of g-C_3N_4 during thermal polymerization and (ii) post-synthesis treatment, which involves the intercalation *via* molten salt treatment (*e.g.*, heating g-C_3N_4 with alkali metal

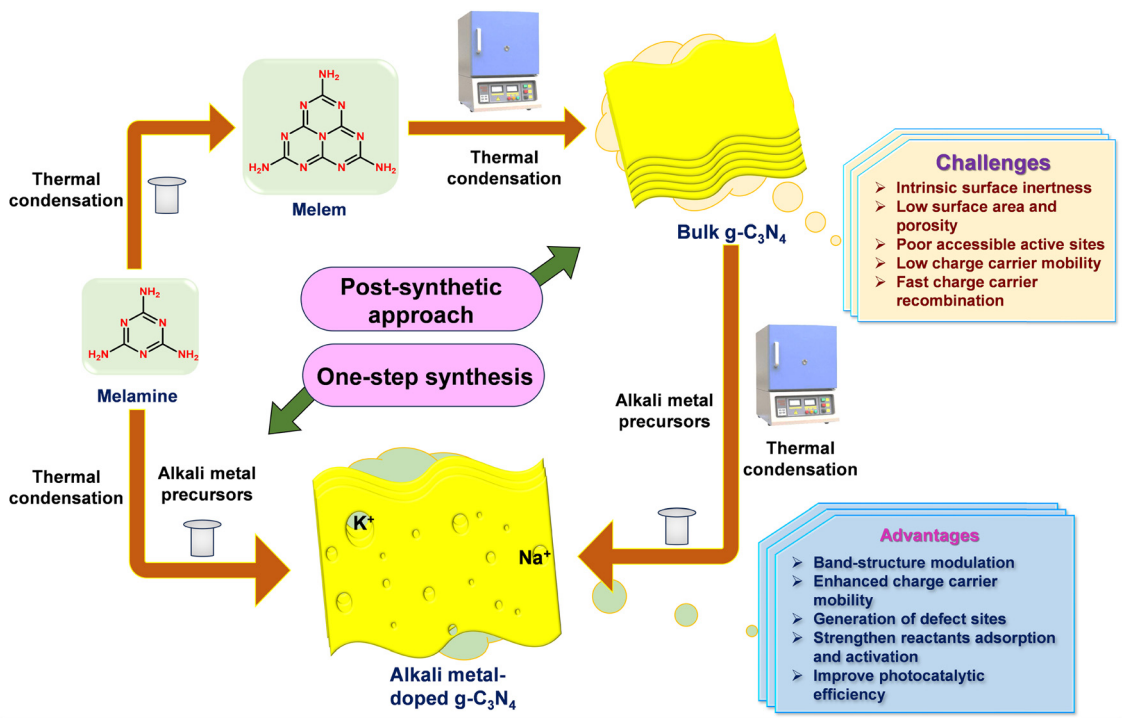

Fig. 6 Direct and step-wise synthesis of alkali metal-doped g-C_3N_4.

precursors).[26,72–77] For example, Dong *et al.* synthesized alkali metal-doped g-C_3N_4 (CN–M, M = Li, Na, K) *via* co-pyrolysis of melamine with the respective metal chlorides.[72] The structural and compositional features confirmed the successful alkali doping. XRD exhibited weakened and shifted diffraction peaks, indicating interlayer intercalation and framework disruption upon alkali metal incorporation. FT-IR spectra revealed the emergence of a –C≡N band and decreased N–H stretching, confirming substitution and defect generation. SEM and TEM demonstrated that Na and K doping produced nanosheets with increased roughness and network-like morphology, while Li showed a minimal morphological change. The BET adsorption isotherm demonstrated a reduced surface area and enlarged pore sizes for CN–M, suggesting structural disorder induced by doping. XPS confirmed the presence of dopant elements, surface N vacancies, and increased –C≡N functionalities, while shifts in C 1s and N 1s binding energies indicated electron redistribution from host N atoms to metal ions.

In contrast to the one-step co-condensation process of alkali metal doping, the post-synthetic modification strategy follows thermal annealing, enabling simultaneous structural exfoliation and alkali metal doping within the g-C_3N_4 matrix. The synergistic effects of exfoliation and doping endow more accessible active sites and improve the textural features, leading to superior photoresponsive performance. For instance, Li-doped g-C_3N_4 (Li/g-C_3N_4) was fabricated *via* a simple two-step impregnation process from melamine and LiOH as precursors.[69] Lithium incorporation levels at 2.7, 5.0, and 9.0 wt% were confirmed by ICP-MS. The XRD analysis revealed an increase in the interlayer spacing upon Li incorporation, indicating reduced crystallinity and structural distortion. FT-IR spectra further confirmed Li doping; it was found that the amine-related band at nearly 3344 cm^{-1} was reduced after Li doping, indicating H substitution by Li atoms along with the enhanced band at 2174 cm^{-1} arising from the formation of controlled defect sites. Morphological changes by Li introduction were evident from SEM and HRTEM analyses, where pristine g-C_3N_4 transformed from smooth nanosheets to wrinkled and rock-like structures at higher Li loadings. In a separate study, an ultrathin porous g-C_3N_4 (MCN) was constructed by thermally polymerizing melamine and urea. Urea served as a porogen to create a porous framework. Subsequently, K-doped MCN (denoted as KMCN) was then prepared by hydrothermal recalcination of MCN and KOH as precursors.[74] The successful synthesis of KMCN was evidenced by PXRD, XPS, and FT-IR spectroscopy. XRD data revealed that the porous structure of MCN remained intact after K incorporation. Moreover, a noticeable decrease in the intensities of (100) and (002) diffraction peaks of MCN was observed, suggesting the defect creation due to incomplete polymerization. Furthermore, the FT-IR analysis revealed that the peak around 3300 cm^{-1} was somewhat reduced, indicating the substitution of H by K^+ in –NH_2 groups, resulting in the creation of N–K linkage. Again, XPS analysis supported the successful doping of K^+. The disappearance of two N 1s peaks near 400.9 and 399.5 eV in KMCN and the appearance of an additional peak around 400.7 eV (C-N3) demonstrated the deprotonation effect caused by K-doping. Additionally, K 2p peaks at 295.2 eV and 292.8 eV suggest the successful doping of K^+ and N–K bond formation (Fig. 7a–c). The morphological analysis revealed that after K doping and recalcination, the smooth surface of g-CN becomes rough, porous, and a stacked pimple-like structure (Fig. 7d–g). The BET surface area and the pore volume of KMCN were found to be 50.1 $m^2\ g^{-1}$ and 0.32 $cm^3\ g^{-1}$, suggesting the existence of mesopores in the structure.

Similarly, Hu *et al.* reported a post-synthesis strategy for fabricating gradient K-doped g-C_3N_4 (KCN) through sequential

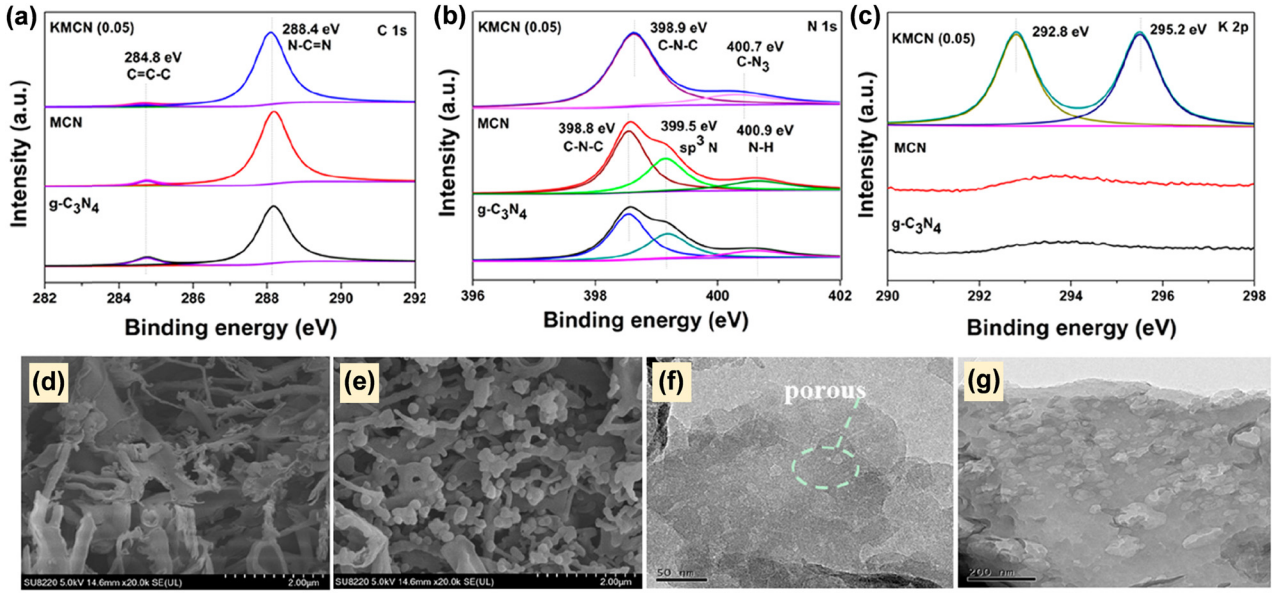

Fig. 7 XPS spectra of (a) C 1s, (b) N 1s, and (c) K 2p of g-C_3N_4, MCN, and KMCN, SEM (d) and (e) and TEM (f) and (g) images of MCN and KMCN. Reproduced with permission from ref. 74. Copyright 2018, American Chemical Society.

thermal treatment.[75] Initially, bulk g-C_3N_4 (CN) was synthesized by pyrolysis of melamine at 550 °C. This CN material was then thoroughly mixed with KCl and subjected to secondary calcination at 550 °C under a N_2 atmosphere (Fig. 8a). The initial polymerization at moderate temperature led to the formation of a defective layer structure with $-NH_2$ and –NH groups (Fig. 8b and e). Upon subsequent high temperature treatment, the hydrogen bonds were removed, the heptazine units were distorted, and the n–π* electronic transition was activated (Fig. 8c and f). Furthermore, K^+ incorporation introduced $-C\equiv N$ functionalities (Fig. 8d and g) and created a compositional gradient, leading to variation in band structure. Structural analysis revealed that K^+ intercalation into the heptazine framework reduced the basal spacing, as evidenced by a distinct shift in the (002) XRD diffraction peak from 27.8° (pristine CN) to 28.2° (KCN). Morphological characterization further demonstrated that the introduction of K^+ ions fragmented the simple plate-like particles of CN to smaller, irregular plate-like particles of KCN, resulting in a reduced crystallinity. HRTEM analysis confirmed the absence of discernible lattice fringes in KCN, indicating its lower crystallinity. N_2 physisorption analysis indicated improved textural properties in KCN, showing type IV isotherms with increased surface area relative to CN.

The supramolecular self-assembly of g-C_3N_4 precursors is a template-free method, which leads to the production of highly porous g-C_3N_4. This efficient synthesis approach involves the formation of supramolecular aggregates *via* the self-assembly of g-C_3N_4 precursors such as melamine, cyanuric acid, urea, *etc.*, through hydrogen bonding. The resultant supramolecular aggregates coupled with alkali precursors to form alkali-doped porous g-C_3N_4-based photocatalysts.[76,77] For instance, Lu *et al.* fabricated K-doped g-C_3N_4 porous nanosheets (CM-K) through supramolecular self-assembly, followed by a chemical cross-linking copolymerization method.[76] At first, the supramolecular precursor (MCA) was formed by treating melamine and cyanuric acid in ethanol *via* an H-bonded self-assembly process. The resultant MCA precursors were copolymerized with potassium hydrogen phthalate (KHP) through the cross-linking phenomenon, followed by acid–base interaction. Finally, the resultant precursor was calcined to obtain CM-K (Fig. 9a), having a more pronounced BET surface area of 127 $m^2\ g^{-1}$ with abundant mesoporous channels. The resultant CM-K material exhibited a hollow box structure with enriched porosity and higher pore volumes, which can be attributed to the gas bubble formation during the thermal decomposition of the

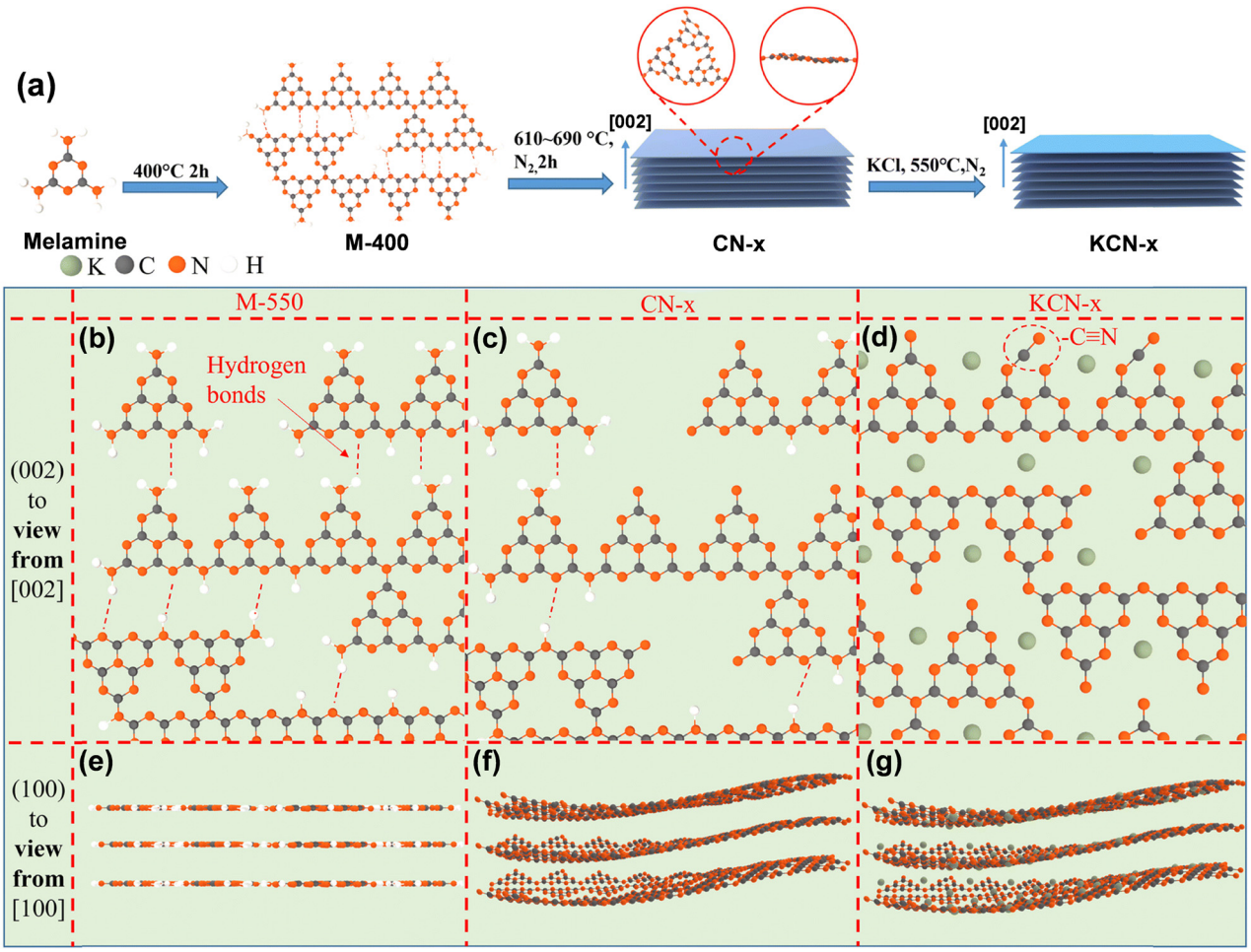

Fig. 8 (a) Schematic representation of the formation mechanism of CN samples. Structural evolution viewed from the [002] direction (b)–(d) and the [100] direction (e)–(g). Reproduced with permission from ref. 75. Copyright 2025, Royal Society of Chemistry.

supramolecular complex, and the addition of KHP led to inadequate crystal growth, which formed a more porous structure with numerous adsorptive sites (Fig. 9b–e). HRTEM EDX elemental mapping confirmed the uniform nanoscale distribution of K throughout the g-C_3N_4 framework (Fig. 9g–j), and the magnifying aberration-corrected high-angle annular darkfield scanning transmission electron microscopy (AC HAADF-STEM) recorded the bright spots, which correspond to the existence of K single atoms in the periphery of the crystalline triazine motif in CM-K_{12}, resulting in successful K-single atom doping in g-C_3N_4 (Fig. 9e and f). Moreover, the resultant porous CN framework provided an appropriate micro-environment to ideally host the K atoms and acted as a suitable support matrix to stabilize K-single atoms in g-C_3N_4 interlayers *via* forming K–N coordination. The K-single atom doping was further confirmed from the K 2p XPS and Fourier-transform extended X-ray absorption fine structure (FT-EXAFS), which suggested that the K–N binding sites existed in CM-K. Furthermore, FT-EXAFS also confirmed that the oxidation state of K is between 0 and 1, which suggests the movement of e^- from 'K' to the g-C_3N_4 matrix. As a result, a greater number of e^- incorporated into the π-conjugated structure of CM-K_{12}; therefore, it exhibited a stronger Lorentzian line intensity than CM in EPR analysis (Fig. 18a). Thereafter, another example reported the construction of K-doped tubular g-C_3N_4 (TCN-K) *via* supramolecular self-assembly of melamine, cyanuric acid, and potassium acetate as precursors.[77] XRD analysis revealed that there is a minor shift in the (002) peak towards a higher angle in TCN-K, indicating a decreased interlayer stacking distance due to K^+ doping. TCN-K exhibited a uniform porous tubular morphology with a diameter of ~80 nm, and K^+ incorporation did not disrupt the tubular structure, as confirmed by morphological investigation by SEM and TEM. The BET isotherm of TCN-K possessed a significantly higher surface area (62.1 $m^2\ g^{-1}$) and pore volume (0.378 $cm^3\ g^{-1}$), offering more abundant active sites, compared to TCN. XPS peaks of C and N exhibited no characteristic shifts after K^+ doping, suggesting interstitial doping rather than substitutional doping. Moreover, a distinct doublet peak for K $2p_{3/2}$ at 293.1 eV and K $2p_{1/2}$ at 295.3 eV was observed in TCN-K, which provided direct evidence for the successful incorporation of K into the TCN lattice.

Considering all the discussed examples in this section, g-C_3N_4 with successful alkali metal doping exhibits multifunctional properties, including electronic tuning through electron redistribution and defect creation, along with increased active-site accessibility and structural optimization that promotes porosity.

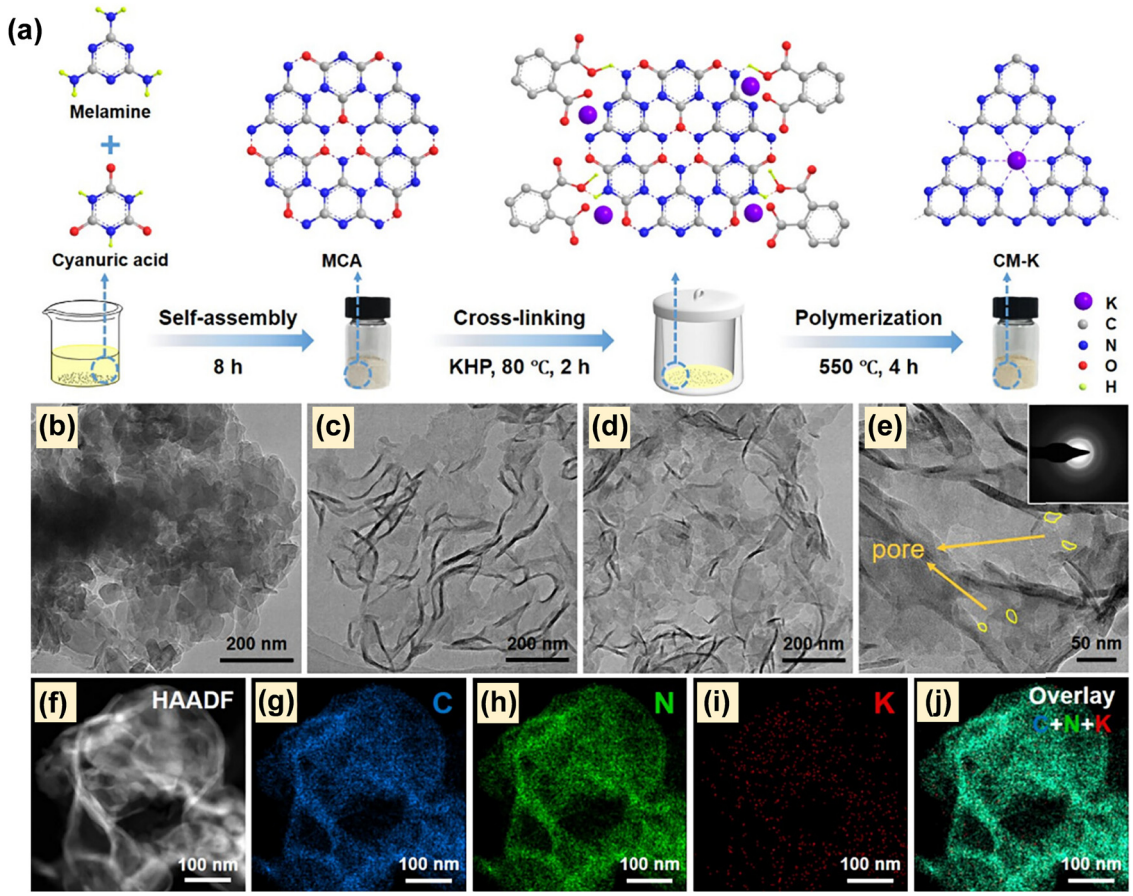

Fig. 9 (a) Diagrammatic overview of the CM-K sample preparation route, TEM images of (b) CN (bulk g-C_3N_4), (c) CM (porous g-C_3N_4), and (d) CM-K, (e) HRTEM image of CM-K with the corresponding SAED present in the inset, (f) HAADF-STEM image of CM-K along with the EDX elemental distribution maps for (g) C, (h) N, (i) K, and (j) their composite overlay. Reproduced with permission from ref. 76. Copyright 2024, American Chemical Society.

2.3. Alkali metal-induced structural and optoelectronic modulation in g-C_3N_4

The structural and optoelectronic modifications induced in g-C_3N_4 upon alkali metal doping are discussed in this section. The incorporation of alkali metal cations (Li^+, Na^+, K^+, *etc.*) within the interlayer cavities of g-C_3N_4 can interrupt its ideal stacking order, leading to modifications of the crystal parameters and significantly altering the structural configuration. Consequently, more lattice defect sites and structural distortion arise, leading to higher surface and exposure of abundant active sites. Moreover, the doping of alkali metals modulates the electronic parameters by optimizing the charge distribution to create favorable electron transport channels that promote efficient charge transfer process. Due to the charge redistribution, shallow donor states are created, resulting in band gap narrowing with redshift in light absorption for better light harvesting.[78–82] Jiang *et al.* demonstrated that these alkali metal atoms are introduced as dopants; they modulate the electronic structure by shifting the CB and VB positions and inducing intra-band defects. This electronic modulation arises from the interaction between the isolated atomic orbitals of the dopant and molecular orbitals of g-C_3N_4, resulting in tuning of band edge alignments, depicted in Fig. 10a.[45] The optical and electronic characteristics of g-C_3N_4 differ according to the nature and concentration of the dopant. Several theoretical studies revealed that the introduction of Li atoms into the crystal structure of g-C_3N_4 significantly influences its electronic structure as Li atoms preferably occupy open-hollow sites in g-C_3N_4, forming three Li–N bonds with adjacent N-atoms having bond lengths of 1.82–2.01 Å.[82] This Li-doping induced structural distortions due to the close proximity of N–Li, which enhances the N–N repulsion effect. Notably, it was also indicated that introducing an odd number of Li atoms into the g-C_3N_4 framework induces metallic behaviour, whereas doping with an even number of Li atoms alters the electronic configuration by broadening the band gap. Furthermore, Li incorporation enhances the optical absorption but reduces the thermodynamic stability of g-C_3N_4. Additionally, with an increase in Li concentration, the work function gradually decreased in Li-doped g-C_3N_4. In a separate study, Ma *et al.* developed Ag-loaded, Li-doped g-C_3N_4 *via* a straightforward and economical calcination approach by using melamine, CH_3COOLi, and $AgNO_3$ as precursors.[83] Li^+ ions with different concentrations were doped into the interlayer voids of g-C_3N_4 (Li(x)–CN, where x = 0.05, 0.10, 0.15, 0.25%), forming a Li–N bond, as confirmed by XPS analysis. The Li deposition led to inhibition of the long-range crystal growth as evidenced by the PXRD analysis. Moreover, Li doping narrowed the band gap from 2.45 eV to 1.99 eV and extended visible light absorption with a red shift, accompanied by deepening of the color of the synthesized samples with increasing Li concentration (Fig. 10b and c). Furthermore, Li(x)–CN demonstrated a significant PL quenching, indicating highly suppressed charge recombination and improved charge separation. Additionally, Ag deposition caused improved visible light harvesting *via* the SPR phenomena. This dual incorporation of Li and Ag in g-C_3N_4 successfully tuned its optical features and ultimately ameliorated the photocatalytic activity.

Similarly, Zhang and co-workers synthesized Na-doped g-C_3N_4 samples (Na(x)–CN, where x = 0.02, 0.05, 0.1, and 0.2 M of NaOH) *via* calcination of dicyanamide and NaOH, where Na atoms occupied interstitial regions.[84] SEM analysis revealed partial fragmentation of the in-plane structure of g-C_3N_4, resulting in smaller crystallites by Na-doping. The XRD patterns indicated that there is a slight shift in the (002) diffraction peak towards the lower angle in Na(0.05)–CN, consistent with an increase in interlayer distance due to interstitial Na-doping, resulting in a decrease in grain size. BET isotherm analysis of Na(0.05)–CN demonstrated a type IV isotherm, signifying the existence of mesoporous architecture further confirmed from the hysteresis loop in the low-pressure range ($0.4 < P/P_0 < 0.9$) originated due to the intra-aggregate porosity and an additional loop at higher pressure in the range of $0.9 < P/P_0 < 1$, corresponding to the presence of larger mesopores in Na(0.05)–CN (Fig. 11a). The SSA of Na(0.05)–g-CN increased to 33.5 $m^2\ g^{-1}$ and provided a larger number of active sites for light absorption to carry out photocatalytic reactions. This increased SSA might be due to Na-doping, hindering the g-CN crystal growth. The XPS analysis further confirmed interstitial Na incorporation, evidenced by peak shifting towards

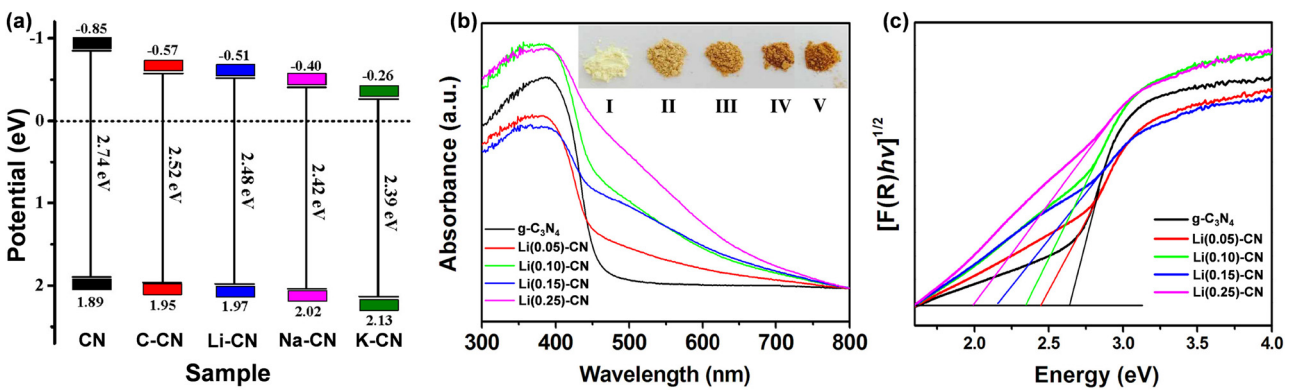

Fig. 10 Illustration of (a) the band structure of g-CN and alkali metal-doped g-CN. Reproduced with permission from ref. 45. Copyright 2017, Elsevier. (b) UV-vis absorption spectrum and (c) band gaps of all the synthesized samples with different Li concentrations. Reproduced with permission from ref. 83. Copyright 2017, Elsevier. (for interpretation of the references to color in this figure legend, the reader is referred to the web version of this article).

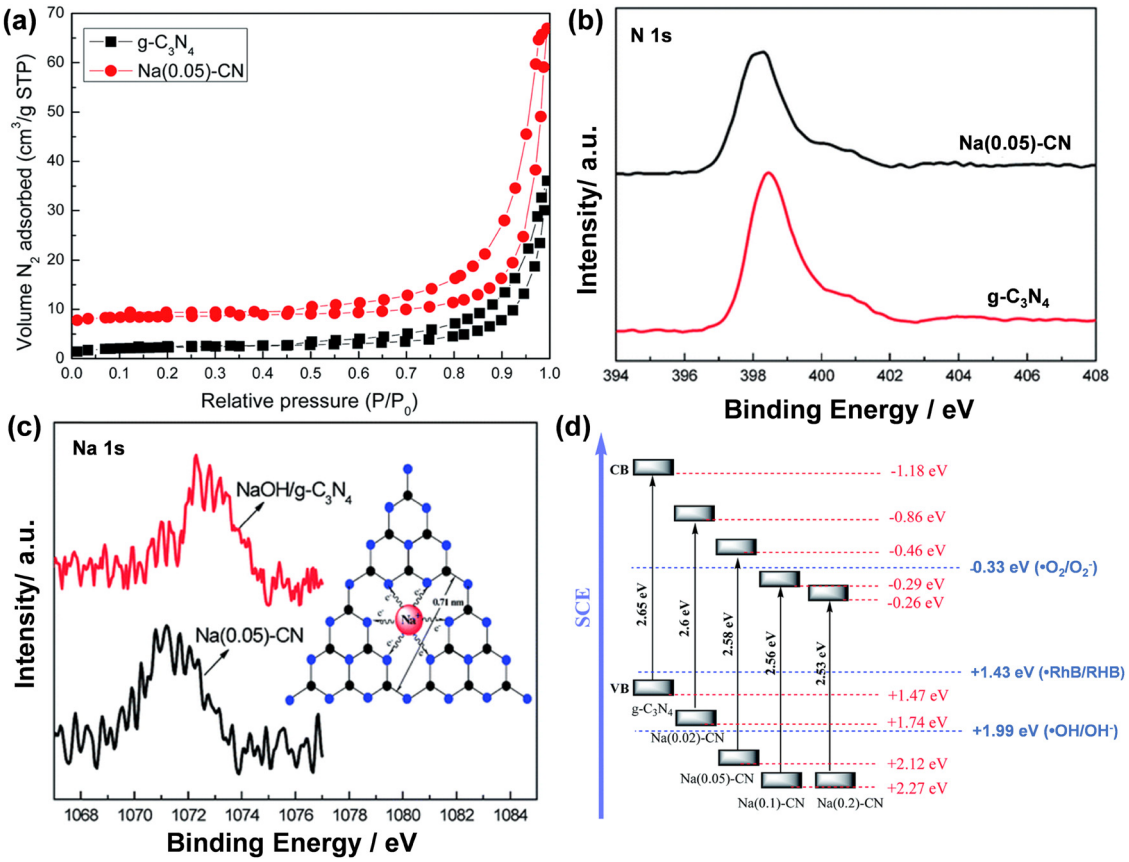

Fig. 11 (a) BET adsorption isotherm of g-C_3N_4 and Na(0.05)–CN, (b) N 1s, (c) Na 1s XPS spectra (possible doping site of Na^+ (inset)) of Na(0.05)–CN, and (d) band gap structures of the prepared materials. Reproduced with permission from ref. 84. Copyright 2014, Royal Society of Chemistry.

lower binding energy for N 1s in Na–g-CN, mediated by robust interaction between N atoms and Na atoms (Fig. 11b and c). Due to the electronegativity of the N atom, a shift of e^- occurred from Na towards the N atom. Moreover, the Na 1s binding energy suggested that Na ions are coordinated within the C–N framework through N-bridging interactions. Hence, in Na(0.05)–g-CN, the availability of electron pairs on the N-atom contributes significantly to the redistribution of electron density and modulates the electronic structure. UV-vis spectral analysis suggested a red shift in the absorption edge, accompanied by a band gap reduction from 2.65 eV for bulk g-CN to 2.58 eV for Na(0.05)–g-CN. With increasing Na concentration, the CB and VB edges were gradually altered (Fig. 11d). Also, PL and electrochemical analyses confirmed the Na doping and subsequent structural modifications and optimized band alignment exhibited an enhancement in the separation kinetics of photogenerated charge carriers. In another study, Sudrajat *et al.* fabricated Na-doped g-C_3N_4 through solid-state thermal polycondensation of a mixture of urea, NaCl, and NH_4Cl.[85] It has been reported that during synthesis, exfoliation occurred and several edge defects were found. The XRD analysis revealed that the (002) and (100) peak intensities decreased, indicating lower crystallinity and exfoliation of g-C_3N_4, confirming an increase in interlayer spacing by Na doping. Moreover, an increase in Na content was found to inhibit the polymeric condensation process. By Na doping, the morphology of undoped g-C_3N_4 was disrupted to smaller, thinner nanosheets, evidenced by SEM and TEM analyses. These structural changes resulted in an increase of SSA to 27.6 $m^2\ g^{-1}$ for the highest Na-doped sample and also led to a reduction in band gap, altering band edge potentials. The incorporation of Na tuned the band alignment by reducing the band gap and facilitating a shorter charge carrier migration path within Na–g-C_3N_4. Due to this, there was a redshift in the PL emission and a marked quenching of the PL intensity, signifying the effective charge carrier separation.

A similar example of Na-doped g-C_3N_4 was reported by Guo and co-workers. They synthesized a deprotonated Na-doped g-C_3N_4 (Na–CN) material *via* solid-state reaction involving mechanochemical blending of melamine and NaCl in a weight ratio of 1 : 10, followed by small tablet creation and thermal treatment within a quartz tube.[86] This process facilitated a strong interaction between precursors, enabling Na^+ insertion into the g-C_3N_4 crystal lattice. PXRD analysis suggested an expansion of the lamellar spacing due to the larger radius of Na^+ ions, indicating that the Na^+ ions could potentially replace the terminal protons and interact with the surrounding N atoms in Na–CN (Fig. 12a and b). TEM investigation showed that the lamellar morphology assembled into a stacked structure with an interplanar distance of 1.180 nm in Na–CN (Fig. 12c). After deprotonation, the remaining e^- were delocalized over adjacent C-atoms and resulted in the origination of

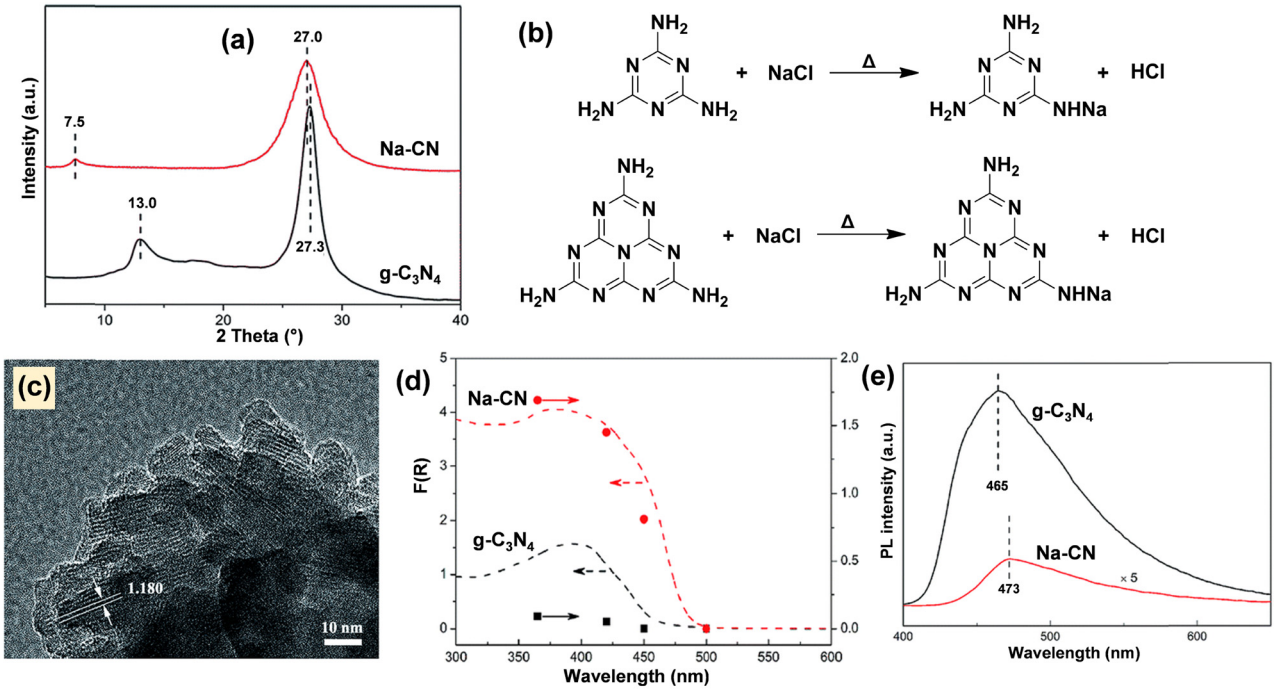

Fig. 12 (a) XRD patterns of g-C_3N_4 and Na–CN, (b) schematic depiction of synthesis of Na–CN, (c) TEM of Na–CN, (d) UV-vis DRS, and (e) PL spectra of the synthesized samples. Reproduced with permission from ref. 86. Copyright 2016, Royal Society of Chemistry.

defect levels within the band gap. The UV-vis spectra revealed a redshifted absorption edge (483 nm) after modification, with a decreased band gap to 2.57 eV, which is 0.12 eV less than pristine g-C_3N_4 (Fig. 12d). Mott–Schottky analysis further elucidated the electronic structure of Na–CN, indicating that the valence band maxima (VBM) position after deprotonation remained unaltered, while the conduction band minima (CBM) potential of Na–CN shifted to −1.19 V, compared to pristine CN (−1.31 V), which is a declination by *ca.* 0.12 V. Moreover, a marked suppression of the PL signal suggested an enhanced localization of e^- at the terminal surface sites of Na–CN. Additionally, the observed redshifts of the emission peak indicated the existence of intermediate electronic states within the band structure (Fig. 12e). The intensified transient photocurrent (TPC) generation indicated a superior separation efficiency of photoinduced carriers, which further supported the PL observations.

K^+ doping, analogous to Na^+ incorporation, modifies the g-C_3N_4 framework and enhances its optoelectronic features. The introduction of K^+ ions leads to reduced crystallite size, diminished recombination rate, enhanced charge kinetics, and improved surface properties and structural modification. Considering the favorable aspects of K^+ doping, numerous research groups have investigated K-doped g-C_3N_4 systems for diverse photocatalytic applications.[87–94] For example, Li *et al.* developed an eco-friendly K-doped g-C_3N_4 composite supported on biochar *via* a calcination-impregnation approach employing dicyanamide, KOH, and biochar as precursors.[87] K-doping disrupted crystallinity and reduced the particle size, while biochar provided a high surface area and induced porosity. K-doping caused a red shift in the absorption edge, resulting in band gap narrowing and modulation of electronic structure, while improving charge carrier separation efficiency. Wang and coworkers reported a series of K-doped g-C_3N_4 (denoted as K–CN-10) photocatalysts, fabricated through thermal polymerization using thiourea and KBr. The formation mechanism of K–CN-10 is depicted in Fig. 13a.[88] Upon K^+ intercalation, the –NK bonds were formed with the tri-*s*-triazine units, resulting in weakening of the (002) XRD peak intensity, with peak shifting from 27.4° to 28.3°, indicating a reduction in the interplanar distance. The strong interaction of K^+ ions with the g-C_3N_4 ring improved the π-conjugation by lowering the interlayer energy barrier and simultaneously promoting a higher extent of polymerization. K^+ incorporation in g-C_3N_4 altered its morphology. Both SEM and TEM images unveiled that K–CN-10 exhibited an anisotropic 2D lamellar structure with mesoporous channels (Fig. 13b and c). The formation of this mesoporous framework was further confirmed from N_2 sorption isotherms, which displayed a type-IV isotherm accompanied by H3 hysteresis loops, suggesting that the synthesized material possesses slit-like pores arising from the aggregation of plate-shaped particles. K^+ modification in g-C_3N_4 reduced its band gap, thereby improving its light absorption ability and simultaneously prolonging the lifetime of photoexcitons, leading to a restrained recombination rate. Thereafter, Zhang and coworkers fabricated a K-doped g-C_3N_4 photocatalyst *via* a thermal condensation process employing dicyanamide and potassium iodide (KI) as starting materials.[89] Upon K-doping, the resultant material exhibited a redshift with a reduced band gap of 2.64 eV (K-C_3N_4). Band structure analysis suggested that the VB position of K-C_3N_4 exhibited an anodic shift due to the K-doping.

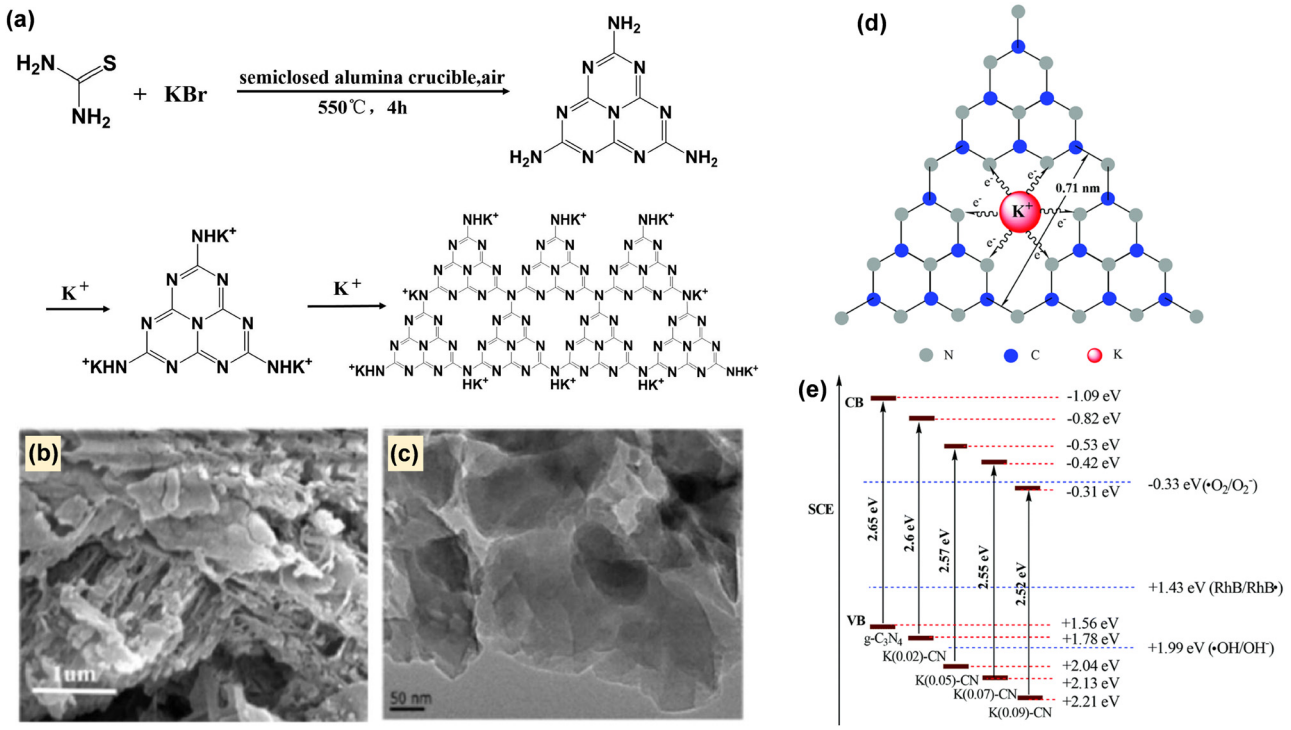

Fig. 13 (a) Schematic representation of the stepwise synthesis and (b) and (c) SEM and TEM pictures of K–CN-10. Reproduced with permission from ref. 88. Copyright 2018, Elsevier. (d) Illustration showing the possible doping sites of K^+ in K(x)–CN and (e) band structures of g-C_3N_4 and K(x)–CN (where x corresponds to the concentration of KOH, x = 0.02, 0.05, 0.07, and 0.09 M). Reproduced with permission from ref. 90. Copyright 2015, Royal Society of Chemistry.

Furthermore, the reduced PL intensity of K-C_3N_4 suggested the slow recombination of the photogenerated charge carriers, thereby enhancing charge separation. The EIS Nyquist plot of K-C_3N_4 exhibited a smaller arc radius than g-C_3N_4 due to the charge redistribution and enhanced interfacial charge transfer induced by K-doping. Consequently, K-C_3N_4 indicated a photocurrent response that was nearly four times higher relative to undoped g-C_3N_4. In a separate study, K-doped g-C_3N_4 (K–CN) was constructed by Hu *et al.* by calcining dicyanamide and KOH.[90] The interplanar spacing (0.71 nm) in g-C_3N_4 can accommodate K^+ ions through ion–dipole interaction, as depicted in Fig. 13d. The introduction of K^+ induces structural distortion in g-C_3N_4, causing an enhancement in surface energy. K^+ doping caused a shift of the optical absorption edge towards a longer wavelength, resulting in band gap reduction from 2.65 eV to 2.52 eV in g-C_3N_4. Moreover, K-doping also led to changes in the electronic state upon the hybridization of the K's atomic orbital and the C_3N_4's molecular orbital, enabling tuning of VB and CB potentials. At an optimum K^+ doping concentration (0.05%), the VB potential became more positive (from + 1.56 eV to + 2.21 eV), while the CB potential became less negative (shifting from −1.09 to −0.31 eV) (Fig. 13e). XPS analysis revealed that K doping caused the change in the electron density on the N atom; as a result, a minor negative shift was observed in N 1s and K 2p binding energy, which evidences the presence of a strong –NK interaction in K–CN. Because of the electron transfer from K to N atoms, the electron density is more localized on the N-atom, thereby leading to a modification in the g-C_3N_4 band structure.

As mentioned in the DFT section, Xiong *et al.* investigated the comparative electronic properties of K and Na-doped g-C_3N_4 synthesized through a calcination process. In this system, K atoms were incorporated within the interlayer spaces, acting as bridges between the layers and extending π-electron delocalization, while Na atoms were introduced into the planar framework of g-C_3N_4, resulting in an enhancement of charge density in the graphitic plane.[39] Although both dopants enhanced the light absorption by narrowing the band gap, their structural differences led to divergent photocatalytic activity. Both K and Na doping induced a downshift in both the VB and CB levels. The more positive VB potential in K-doped g-C_3N_4 improved the oxidation capability of the photogenerated holes (h^+), thereby imparting superior photocatalytic efficiency compared to Na-doping. This variation in activity was attributed to the distinct atomic radii of the respective alkali metal dopants. High-temperature treatment induced structural deformation, leading to the formation of $–NH_2$ groups at the edge of the g-C_3N_4 sheets. The accommodation of alkali metal ions was facilitated by these electron-rich $–NH_2$ groups. DFT calculations of CN-Na-2 and CN-K-2 samples further confirmed stable doping configurations, with K occupying the interlayer space and Na in the π-conjugated planes. Moreover, Na-doping preserved the crystal structure, while K-doping caused crystal lattice contraction due to its larger size. The electronic location function (ELF) profiles of both K-and Na-doped synthesized samples, illustrated in Fig. 14a and b. In the case of CN-K-2, the ELF values for K–C and K–N bonds were below 0.15, suggesting

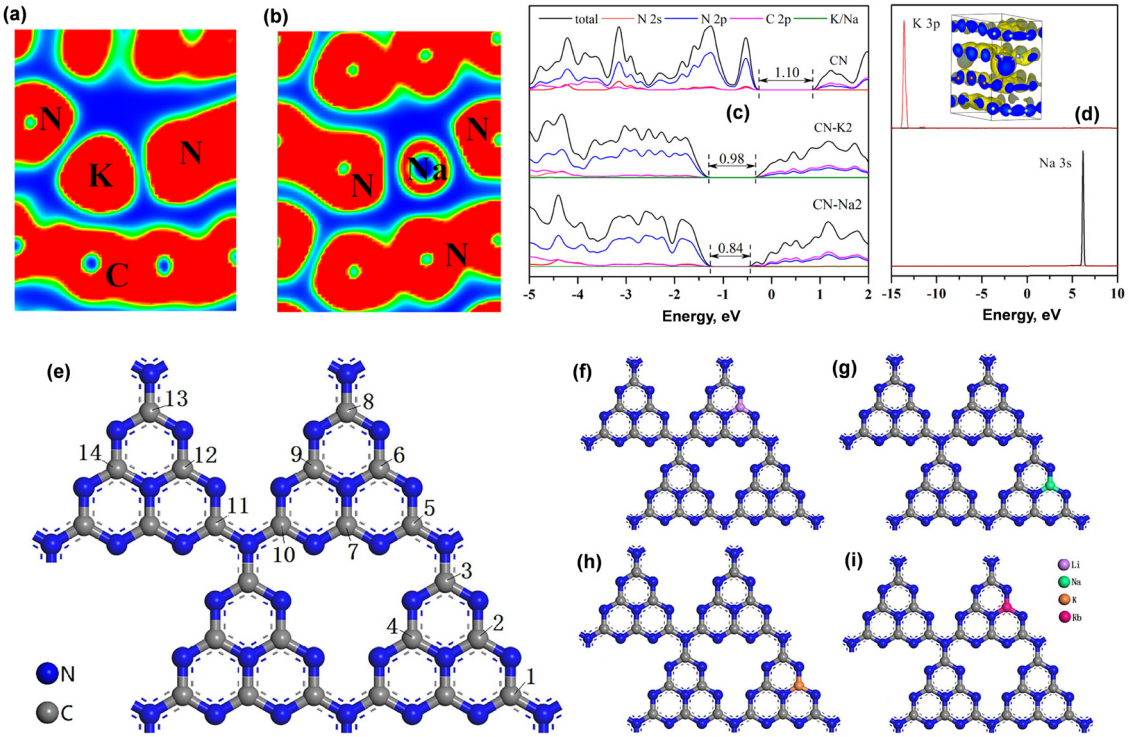

Fig. 14 (a) and (b) ELF analysis of CN-K2 and CN-Na, (c) DOS of CN, CN-K2, and CN-Na2, and (d) contribution of Na and K atoms to DOS (inset: partial charge density around the doping K 3p in CN-K2). Reproduced with permission from ref. 39. Copyright 2016, American Chemical Society. (e)–(i) Optimized structural configuration of bulk g-C_3N_4, Li–g-C_3N_4, Na–g-C_3N_4, K–g-C_3N_4 and Rb–g-C_3N_4, respectively. Reproduced with permission from ref. 96. Copyright 2020, Elsevier.

a weaker covalent bonding. Meanwhile, the Na–N interaction experienced an even lower ELF value, supporting ionic interaction. These distinctions in charge localization suggested that variations in bonding nature influence the photocatalytic performance of the two doped materials. Furthermore, the compositional analysis of the band energies (VB and CB) of g-C_3N_4, CN-Na2, and CN-K2 was estimated by density of states (DOS) analysis, which underscored that the CBM and VBM of all three photocatalysts were constructed by the combination of C 2p and N 2p (Fig. 14c and d). Although Na and K did not contribute to the construction of the band structure, considering their electron-donating ability to the g-C_3N_4 framework, they narrowed down the band gap energy from 1.1 eV for g-C_3N_4 to 0.84 eV and 0.98 eV for CN-Na2 and CN-K2, respectively. The intercalated K atoms facilitated the charge transport channels between the layers, extending the π-conjugated system, reducing electronic localization, and significantly enhancing the charge carrier separation and mobility. This was confirmed by increased photocurrent, smaller EIS arc radius, quenched PL intensity, and prolonged charge carrier lifetime. However, Na doping increased the in-plane electron density but did not create interlayer bridges, which resulted in a higher recombination of photogenerated charge carriers.

Xu *et al.* fabricated different alkali metal-doped g-C_3N_4 (GCN-M, M = Na, K, Rb, Cs) photocatalysts through a simple calcination method.[95] Structural characterization revealed that alkali dopant incorporation disrupted the in-plane long-range order and decreased the interlayer distance and crystallinity, as evidenced by the disappearance of the (100) characteristic diffraction peak in the PXRD pattern. It has been reported that the alkali cations interfere with the formation of hydrogen bonds that typically connect the polymeric melon strands within the plane. The introduction of –C≡N and hydroxyl (–OH) groups originated due to the alkali metal doping, as evidenced by FT-IR and XPS analyses, resulting in the optimization of the electronic structure. All the alkali-doped synthesized materials possessed low SSA, including Na-doped g-C_3N_4 (GCN-Na = 1.92 $m^2\ g^{-1}$), K-doped g-C_3N_4 (GCN-K = 7.43 $m^2\ g^{-1}$), and Cs-doped g-C_3N_4 (GCN-Cs = 6.15 $m^2\ g^{-1}$), except Rb-doped g-C_3N_4 (GCN-Rb = 38.77 $m^2\ g^{-1}$). UV-vis absorption spectra revealed a significant red shift in the absorption edges for the alkali metal modified samples (GCN-Na, GCN-K, GCN-Rb, and GCN-Cs), indicating enhanced visible light harvesting ability with the corresponding optical band gaps of 2.73 eV, 2.69 eV, 2.59 eV, and 2.72 eV, respectively. The effect was most pronounced for Rb^+ and K^+, demonstrating that the larger cations have a more pronounced effect on the structural variation, which altered the band edge potential, *i.e.*, both CB and VB positions shifted upwards. The PL intensity was drastically quenched in the alkali metal-doped samples and followed the trend GCN-K > GCN-Rb > GCN-Cs > GCN-Na, which indicated an effective decline of radiative recombination. Furthermore, the EIS Nyquist plot demonstrated that GCN-K has a shorter arc radius, indicating a reduced charge transfer resistance. In contrast, Zhang and

colleagues demonstrated that Rb-doped g-C_3N_4 exhibited the highest photoactivity compared to Li, Na, and K-doped g-C_3N_4.[96] This superior photocatalytic performance can be ascribed to the fine-tuned structural variation and optimized band alignment achieved due to Rb doping. Although all the synthesized alkali metal-doped samples exhibited a significantly enhanced photo-absorption response in UV-vis spectroscopy, Rb-doped g-C_3N_4 demonstrated an extended absorption range of 500–1100 nm. Furthermore, the band gap energy of Rb-doped g-C_3N_4 was markedly decreased to 2.0 eV compared to the bulk g-C_3N_4 (2.65 eV). Computational modeling and calculated doping energies further revealed the most favorable carbon substitution sites in alkali metal-doped g-C_3N_4, as presented in Fig. 14e–i. Both the experimental observation and DFT study also demonstrated that the extended absorption edges were led by K and Rb dopants, compared to Li and Na.

2.4. Effect of co-doping

Additionally, co-doping with synergistic elements presents a powerful strategy to engineer the photophysical properties of g-C_3N_4 relative to the mono-doping systems. Combining alkali metal ions with other metals or non-metals has emerged as a sophisticated approach for altering the electronic structure, optical properties, and surface chemistry of g-C_3N_4.[58,97–104] The synergy arises from the complementary roles where alkali metals primarily enhance the textural features of g-C_3N_4, thereby facilitating the incorporation of secondary dopants and modulating the electronic environment. This synergistic interplay leads to improved charge separation dynamics, broadened spectral response, and superior photocatalytic performance. Various alkali metal ions containing functionalized co-doped g-C_3N_4 systems are known to improve interlayer van der Waals interaction and enhance charge separation.[98,104–106] Even some metal cations, through interlayer intercalation, accelerate charge transfer between the layers, resulting in the aggregation of localized e^- and thus favor the formation of active species for various photo-redox reactions. Therefore, the influence of alkali metal co-doped g-C_3N_4 systems has been investigated in this section. For instance, K, P co-doped g-C_3N_4 grafted with the –C≡N group (MPCN) was synthesized by a dual-step synthesis method involving copolymerization of urea and hexachlorocyclotriphosphazene (HCCP), followed by subsequent treatment in molten KCl medium (Fig. 15a).[107] The co-incorporation of P and K shifted the (100) XRD peak of MPCN from 13.1° to 11.5°, indicating an expansion of in-plane structural periodicity and a shift in the (002) plane, which suggested an increase in the interlayer spacing (Fig. 15b). The successful K^+ intercalation and –C≡N group grafting was evidenced by FTIR and XPS analyses (Fig. 15c–f). From FT-IR spectra, the peaks at 1000 cm^{-1}, 1153 cm^{-1}, and 2180 cm^{-1} correspond to the N–K bond, asymmetric vibration of the K–CN_2 group, and the –C≡N group of MPCN, respectively (Fig. 15c). From XPS analysis, the peak intensity of C 1s spectra at 286.4 eV significantly enhanced after the K doping, demonstrating the influence of the alkali group in the creation of –C≡N linkages in MCN and MPCN. Additionally, the C 1s peak shifted to a higher binding energy in MPCN compared to CN and MCN, indicating reduced charge density at the carbon atom due to P substitution (Fig. 15d, h and i). The absence of a discernible P–C signal at nearly 131.5 eV confirmed that P predominantly replaced the C atom rather than the N atom in the CN matrix. The 2p of P exhibited two peaks around 132.8 eV and 133.8 eV corresponding to P–N and P═N binding sites, respectively, suggesting the successful P doping (Fig. 15g). The K^+ intercalation reduced the band gap in MPCN, and the conjugation between the chromophoric –C≡N group and C═C bonds of the heptazine ring in MPCN extended the visible light absorption, causing a red shift in UV-vis spectra. PL analysis demonstrated that P, K co-doping, along with terminal –C≡N grafting, significantly quenched the PL intensity by inhibiting the charge recombination process. Similar to the above example, the synergistic

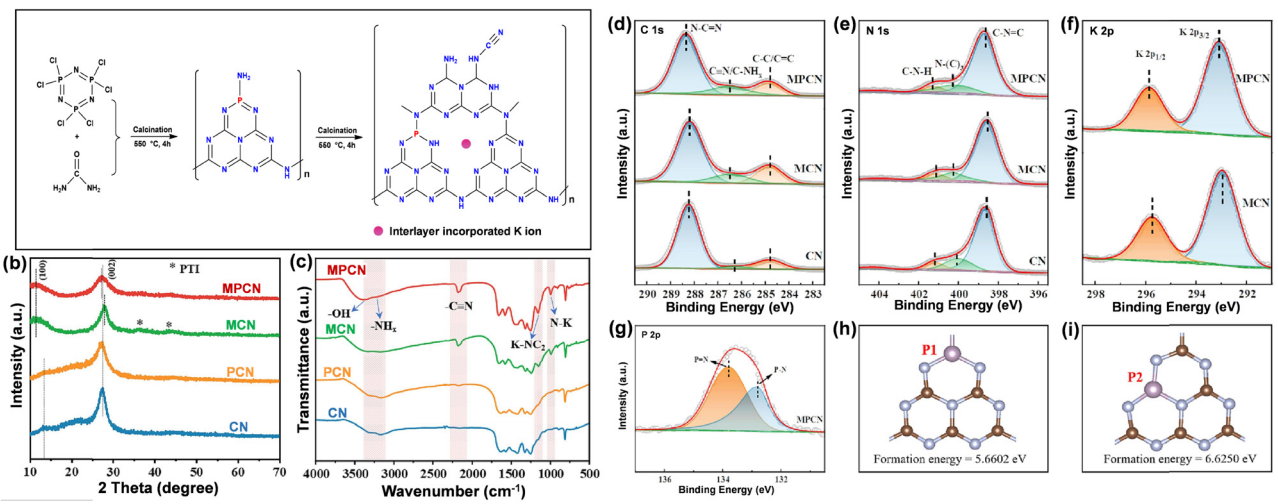

Fig. 15 (a) Diagrammatic sketch of MPCN formation, (b) XRD, (c) FT-IR of CN, PCN, MCN, and MPCN, XPS spectra of (d) C 1s, (e) N 1s, (f) K 2p, and (g) P 2p of CN, MCN and MPCN samples, (h) and (i) optimized atomic model of PCN illustrating two possible substitutional sites. Reproduced with permission from ref. 107. Copyright 2023, Elsevier.

incorporation of B and K into g-C_3N_4 nanosheets reduced the band gap, extended visible-light absorption, and adjusted the charge transport channels.[108] These changes improved the electron distribution and transfer, which effectively inhibits the charge carrier recombination.

Thereafter, Liang *et al.* fabricated K, Bi co-doped g-CN (designated as Bi/K–g-CN) *via* a one-step thermal polycondensation approach.[47] The synthesized Bi/K–g-CN possessed a layered porous morphology with higher SSA, larger pore diameter, and availability of numerous active sites, confirmed from SEM (Fig. 16a–d) and BET sorption analyses. EDS mapping revealed the homogeneous distribution of both K and Bi dopants in the g-CN structure (Fig. 16e–h), and the incorporation of these dopants caused N-defects, which led to a change in its electronic structure. N_2 sorption analysis identified a type IV adsorption isotherm and H3-type hysteresis loops for Bi/K–g-CN, suggesting the formation of a porous structure, and the SSA was found to be more than that of undoped g-CN. XPS analysis indicated a higher C/N ratio in Bi/K–g-CN (1.25) relative to pristine g-CN (0.73), attributed to a higher number of N-defects. Furthermore, the DFT calculations revealed the optimized configuration of g-CN, K–g-CN, Bi–g-CN, and Bi/K–g-CN (Fig. 16i–l). The larger ionic radii of Bi and K caused significant lattice distortion in g-CN, which led to the removal of N atoms to form N-defect sites. Moreover, the optical absorption of Bi/K–g-CN exhibited a redshift and reduced band gap energy compared to all the synthesized photocatalysts. The band structure analysis further confirmed the dual doping, resulting in the more negative CB and VB edge potential compared to g-CN, and thereby minimizing the photocatalytic reaction threshold for enhanced photoactivity. The synergistic effect of this co-doping created charge heterogeneity, optimized the band position, and improved charge separation.

In another study, Wang *et al.* reported the fabrication of Na, Cl-co-doped g-C_3N_4 *via* a simple calcination route employing dicyanamide and NaCl as precursors.[109] The incorporation of an optimal NaCl (0.5) content resulted in a highly crystalline material characterized by sharp PXRD peaks and a slim lamellar morphology. XPS analysis indicated the Na 1s signal at 1071.8 eV, corresponding to Na^+ species, and the Cl 2p peaks at 197.9 and at 199.6 eV, suggesting the coordination of Cl^- with

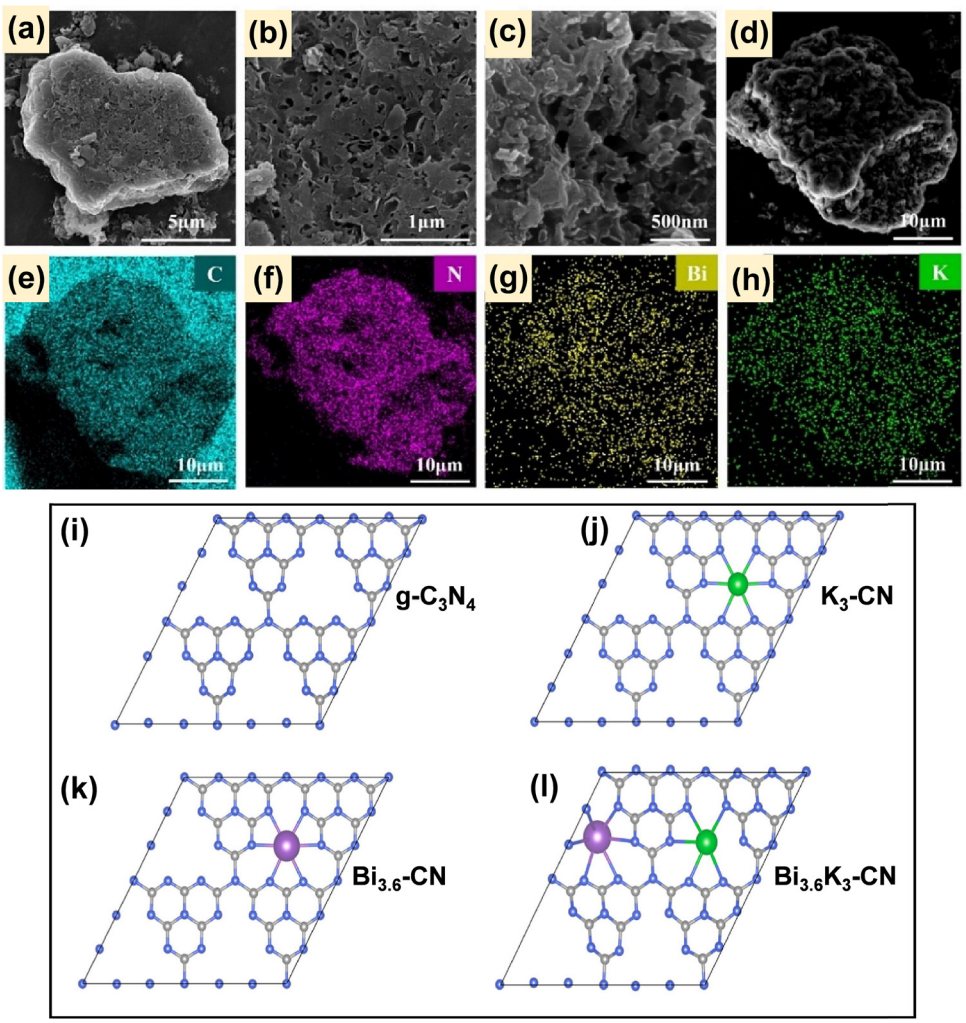

Fig. 16 (a)–(d) SEM pictures, (e)–(h) EDX profile of Bi/K–g-CN, and (i)–(l) theoretical structural models of all the prepared materials. Reproduced with permission from ref. 47. Copyright 2024, Elsevier.

the C and N-atoms, confirming the co-existence of Na and Cl atoms in the g-C_3N_4 framework. After co-doping, the absorption edge was found to be red-shifted, and the band gap energy was reduced from 2.76 eV to 2.67 eV, attributed to the structural and textural modification. Mott–Schottky analysis verified n-type behavior with a positively shifted band potential responsible for enhanced oxidizing ability. The co-doping exhibited a remarkably diminished PL emission intensity, suggesting a suppressed charge carrier recombination, while the photocurrent responses also corroborated with PL results, demonstrating improved charge separation and migration efficiency. In a related study, Na and S-co-doped g-C_3N_4 was successfully constructed through a simple one-step pyrolysis approach.[110] The incorporation of Na and S atoms induced structural disruption in the layered structure of g-C_3N_4, as evidenced by PXRD analysis. The presence of Na and S in the synthesized material was corroborated from FT-IR and XPS analysis, attributed to the Na–N, C–S, and C═S bond formation. Furthermore, the synthesized material exhibited a red shift in the optical absorption edge, suggesting narrowing of the band gap and thereby enhancing the light-harvesting capability.

To conclude, all alkali metal-doped g-C_3N_4 systems have been proven to exhibit significantly higher efficiency as visible-light-active photocatalysts relative to pristine g-C_3N_4. However, the K-doped g-C_3N_4 photocatalysts have been extensively investigated in the literature for various artificial photosynthesis applications due to their tailored electronic and optical characteristics. The enhanced photoresponsive features in alkali metal-doped systems arise from their easily tunable band structure, which generates suitable redox potentials to facilitate diverse photoredox reactions. Furthermore, the co-doping represents a promising approach that deliberately introduces structural disorder, irregular stacking of adjacent g-C_3N_4 layers, and high density of defects, leading to local charge redistribution and optimization of the electronic properties. Table 3 summarizes the synthesis methods, precursors, type of dopant, BET surface area, and band gap of some reported alkali metal-doped g-C_3N_4 photocatalysts.

3. Applications of alkali metal-doped g-C_3N_4

Alkali metal-modified g-C_3N_4 demonstrates versatile applicability in photocatalysis, with several notable applications described below.

3.1. Solar fuel production

Solar fuel production *via* artificial photosynthesis over a suitable photocatalyst proceeds through a defined sequence of fundamental steps. The initial step requires adsorption of reactant molecules on the photocatalyst surface, then, upon irradiation of incident photons, electron–hole pairs are generated in the photocatalyst, where photon energy ($h\nu$) must meet or exceed its bandgap energy (E_g). Subsequently, the photogenerated e^- get promoted from the VB to the CB, leading to their effective separation and migration to the semiconductor surface. The final step involves the surface redox reactions to generate sustainable fuels. However, some of the charge carriers may undergo recombination, including both bulk and surface recombination.[124–126] Consequently, the overall quantum yield critically depends on the efficacy of charge separation and the successful migration of charge carriers to surface-active sites for productive redox chemistry.

Alike g-C_3N_4, alkali metal-doped g-C_3N_4 is a two-dimensional polymeric semiconductor predominantly comprising earth-abundant carbon and nitrogen, featuring a framework constructed from interconnected tri-*s*-triazine units linked *via* planar tertiary amine linkages. Possessing a narrow optical band gap, alkali metal-doped g-C_3N_4 exhibits significant absorption within the visible light spectrum, extending to higher wavelengths. Its appropriate structural framework and electronic band structure provide sufficient thermodynamic driving force for various types

Table 3 List of alkali metal-doped g-C_3N_4 systems synthesized using various precursors

Photocatalysts	Precursors	Dopant	Synthesis method	Surface area ($m^2\ g^{-1}$)	Bandgap energy (eV)	Ref.
KCNN	Urea, KCl	K	Thermal polymerization	68	2.50	61
Li/g-C_3N_4	Melamine, LiOH	Li	Impregnation method	—	2.51–2.68	69
Rb–CN	Melamine, $RbNO_3$	Rb	Calcination	—	2	96
CN-BK	Melamine, KI, H_3BO_3	K, B	Thermal polymerization	81	2.51	108
10% K-CCN	Dicyandiamide, KOH	K	Thermal polymerization	17.7	2.54	111
AMCN/RF	Urea, KCl, NaCl, resorcinol, formaldehyde	K, Na	Calcination, sonication	—	2.07–2.13	112
$Na_{(0.3)}$–CN	Melamine, Na_2CO_3	Na	One-step calcination	7.8	2.34	113
g-C_3N_5:K0.01	3-Amino-1,2,4-triazole, KBr	K	Calcination	—	1.9	114
RbGCN10	Dicyanamide, RbCl	Rb	Calcination	10.2	2.71	115
CoPc/K/Na/PCN-2	Dicyandiamide, KCl, NaCl	K, Na	Ionothermal polycondensation followed by a hydrothermal method	11.5	2.63	116
CN-80PK	Dicyandiamide, K_2HPO_4	K, P	Thermal polymerization	38	2.62	117
$Na_{1.2}$–$P_{0.2}$–CN	Melamine, NaOH, $NH_4H_2PO_4$	Na, P	Thermal polymerization	—	2.61	118
Li/P–g-C_3N_4	Melamine, LiCl, ADP	Li, P	Calcination	14.1	2.19	119
Pd/K–gC_3N_4	Cyanamide, KCl, $PdCl_2$	K, Pd	Calcination	—	2.7	120
Ag/OKCN-6	Urea, $K_2C_2O_4{\cdot}H_2O$, Ag(acac)	K, O, Ag	Thermal polymerization	—	2.54	121
CeO_2/K/Na/CN	Urea, KNO_3, $NaNO_3$	K, Na	Two-step calcination	60	—	122
GCNML	Urea, LiCl, $Mg(NO_3)_2{\cdot}6H_2O$	Li, Mg	Calcination	84	2.58	123

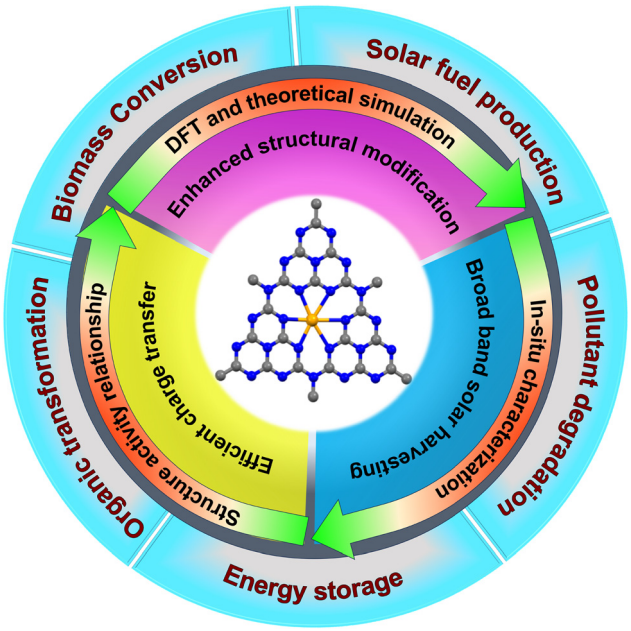

Fig. 17 Schematic depiction of alkali metal-doped g-C_3N_4 with modified structural and optoelectronic features for multi-dimensional applications.

of solar fuel generation, which includes photocatalytic water splitting, CO_2 reduction, H_2O_2 generation, and N_2 fixation as discussed below. Moreover, the structure–activity relationship to underline the mechanistic investigations was also accomplished by in-depth DFT calculations along with theoretical modellings and *in situ* characterization (Fig. 17).

3.1.1. Photocatalytic H_2 production. The photocatalytic H_2 production *via* the H_2O splitting reaction associates with a huge thermodynamic barrier, which requires a Gibbs free energy of $\Delta G^\circ = 237.13$ kJ mol^{-1} (eqn (1)) and a photon energy of 1.23 eV to accomplish the reaction. This process comprises two half-cell reactions, photocatalytic H_2 and O_2 evolution, as shown in eqn (2) and (3):

Overall water splitting (OWS) reaction

$$2H_2O + h\nu \rightarrow 2H_2 + O_2, \quad \Delta G^\circ = 237.13 \text{ kJ mol}^{-1} \tag{1}$$

Photocatalytic H_2 evolution

$$4H^+ + 4e^- \rightarrow 2H_2, \quad \Delta E^\circ = 0 \text{ V} \tag{2}$$

Oxygen evolution reaction (OER)

$$2H_2O \rightarrow 4H^+ + 4e^- + O_2, \quad \Delta E^\circ = 1.23 \text{ V} \tag{3}$$

As indicated by eqn (2) and (3), the band edge potentials of the photocatalyst must align to satisfy the thermodynamic requirement of the OWS reaction. *i.e.*, the CB potential and VB potential are essentially more negative than 0 V *vs.* NHE, and more positive than 1.23 V *vs.* NHE, respectively. During photocatalysis, the H_2O oxidation is carried out by photogenerated h^+ at the VB, generating protons (H^+), which subsequently get reduced to H_2 by photogenerated e^- at the CB of the photocatalyst. Although the VB position of many photocatalysts thermodynamically satisfies the requirement for water oxidation, the OER remains kinetically sluggish owing to its $4e^-$ and $4H^+$ transfer mechanism involving high-energy surface intermediates (eqn (3)). The large overpotential of 1.23 V (eqn (3)) and slow interfacial hole transfer lead to pronounced charge recombination and limited OER efficiency.[127] These challenges can be addressed by using suitable sacrificial agents that selectively trap the h^+ and liberated H^+ at the VB. This enhances charge separation, prolongs the lifetime of CB e^- and facilitates H^+ reduction for H_2 evolution. This process selectively suppresses the high-energy-demanding H_2O oxidation at the VB, while the e^- and H^+ donor nature of the sacrificial agent promotes the efficient H_2 production at the CB *via* the photocatalytic H_2 evolution process.[128–131]

Alkali metal-doped g-C_3N_4-based photocatalytic systems are suitable since they promote efficient charge transfer and effective utilization of photogenerated carriers for enhanced H_2 production relative to pristine g-C_3N_4.[45,76,132–135] Moreover, the change in the free energy for the water splitting reaction is reduced by alkali doping in the g-C_3N_4 crystal lattice. Towards this, Sun *et al.* reported K-doped g-C_3N_4 nanosheets (CNK), prepared by thermal calcination of melamine pre-treated with KOH, which exhibited an enhanced photocatalytic H_2 generation of 919.5 mmol h^{-1} g^{-1}, approximately 13 times superior to bulk CN.[132] The K-doping caused a red shift in visible light absorption, narrowing the band gap of CNK, which modified the band structure by up-shifting the CB edge. Incorporation of K atoms in g-C_3N_4 interlayers suppressed the photogenerated charge carriers' recombination, confirmed by PL spectra. The enhanced photocatalytic performance was ascribed to the increased surface area, which offers abundant surface-active sites, and optimized band edges that favor efficient photoreduction processes. Coupling K-doped g-C_3N_4 with TiO_2 nanobelts (TCN-K) substantially boosted the hydrogen evolution efficiency, primarily owing to optimized charge transport facilitated by the interfacial linkages of K-atoms.[133] Analogous to the previous example, a similar observation in the reduction of band gap, accompanied by improved light harvesting, was reported after K-doping. The incorporated K atoms were chemically bonded to both C and N atoms in the g-C_3N_4 framework, improving interlayer charge transfer. Furthermore, the K-intercalation and 1D TiO_2 nanobelts in TCN-K synergistically improved light absorption, separation and migration of photoinduced charges, reduced electron localization, and extended π-conjugation. As a result, the TCN-K composite exhibited a H_2 evolution rate of 50 μmol h^{-1} g^{-1}, approximately 2.5 times higher than that of CN-K (without TiO_2, 19 μmol h^{-1} g^{-1}).

Similarly, Lu *et al.* demonstrated that effective H_2 production could be accomplished by fabricating the K single atom in g-C_3N_4 (CM-K_{12}).[76] UV-vis analysis and total density of states (TDOS) calculation revealed that the incorporation of K within the g-C_3N_4 framework resulted in a red shift of light absorption and a narrower band-gap with a more optimized band structure, respectively (Fig. 18b and c). The efficient separation and migration of photogenerated charge carriers were dominated in CM-K_{12}, as evident from the PL and EIS Nyquist plot. Furthermore, DFT calculation also revealed that the CM-K surface

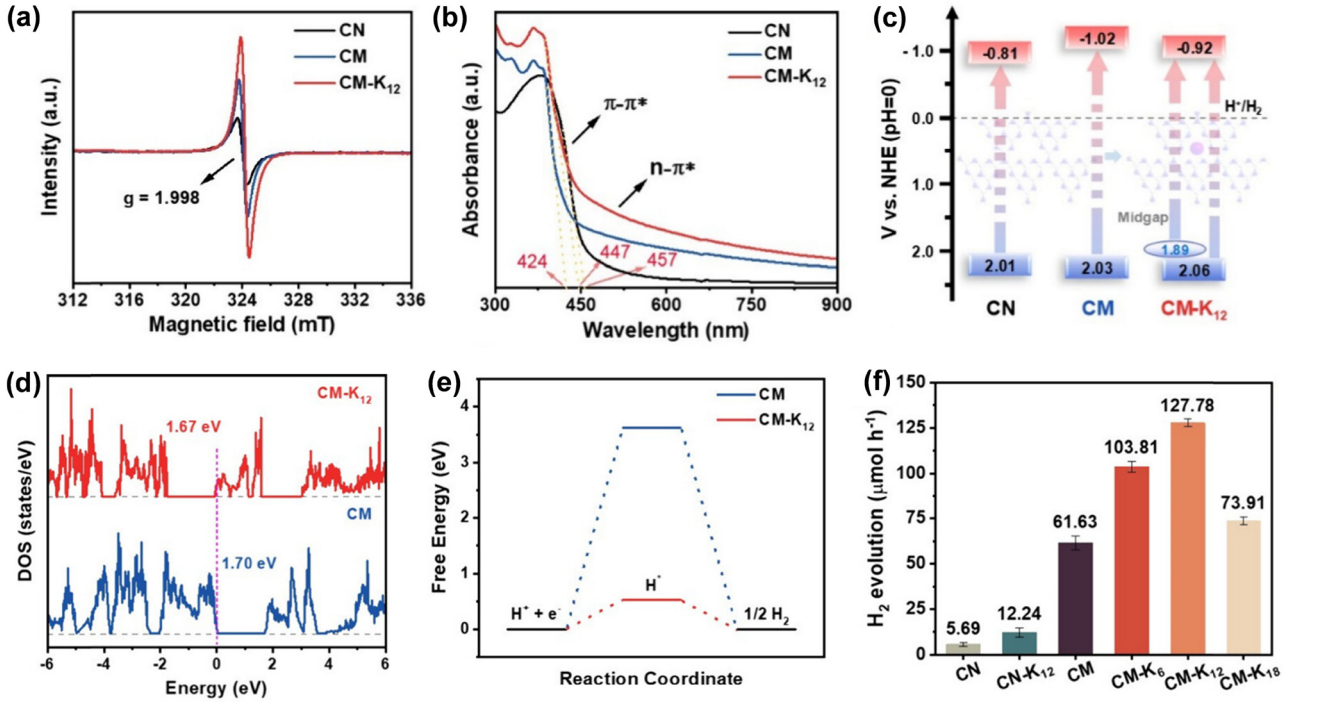

Fig. 18 (a) EPR spectra, (b) UV-vis DRS absorption spectra, (c) corresponding band structure, (d) calculated TDOS of CM and CM-K_{12}, (e) Gibbs free energy profile for photocatalytic H_2 production through the generation of H* over CM and CM-L_x. Charge density difference maps for CM-K_{12}, and (f) H_2 evolution performance of the prepared photocatalysts, where CN-K_x denotes K-single atom doped porous g-C_3N_4 with x = 6, 12, 18 corresponding to the amount of KHP precursor added. Reproduced with permission from ref. 76. Copyright 2024, American Chemical Society.

possessed higher electron density compared to CN and CM because of K-doping, thereby dramatically enhancing the H_2O adsorption ability and also lowering the activation energy barrier of H^+ adsorption to facilitate better H_2 evolution (Fig. 18d and e). All these findings signified CM-K as a superior photo-responsive photocatalyst which satisfies the thermodynamic requirement for the H_2 evolution and therefore exhibited an excellent hydrogen production of 127.78 μmol h^{-1} under visible light irradiation, representing nearly 23-fold higher compared to pristine g-C_3N_4 (Fig. 18f).

Thereafter, Guo *et al.* reported that Na-doped, deprotonated g-C_3N_4 (Na–CN) exhibited significantly enhanced photocatalytic performance, achieving 31.5 μmol of H_2, delivering a higher AQY of 1.45% and 15.2 μmol of O_2 evolution within 1 hour under visible light illumination in the absence of scavengers.[86] This performance markedly surpassed that of pristine g-C_3N_4, which showed a very low H_2 evolution rate (an AQY of 0.05% at 420 ± 15 nm). The significant boost in photoactivity was attributed to improved optoelectronic properties arising from deprotonation and Na doping, which facilitated more efficient charge transfer and prevented the formation of the kinetically unfavorable H_2O_2 intermediate that typically hinders photocatalytic performance (Fig. 19a). The enhanced H_2 evolution highlights the pronounced effect of deprotonation on overall water-splitting reaction under sacrificial-agent-free conditions, along with outstanding photostability and reproducibility. This improvement in the photocatalytic activity can be attributed to the accelerated transfer of photogenerated h^+ to surface-adsorbed –OH species, facilitating O_2 evolution. Similarly, the photocatalytic H_2 evolution behavior of K-doped g-C_3N_4 using Pt as a cocatalyst and triethanolamine as the sacrificial agent was investigated by Wang and coworkers.[88] The optimized K-doped material exhibited the hydrogen evolution of 1337.2 μmol g^{-1} h^{-1} under visible light irradiation, markedly surpassing the pristine g-C_3N_4 (239.8 μmol g^{-1} h^{-1}) (Fig. 19b). The band edge potential was altered by varying the doping percentage. The optimized K doping in the K–CN-10 sample improved the band structure and achieved the required CB potential, appropriate for efficient H_2 evolution. The photocatalyst also exhibited excellent stability and reusability, maintaining consistent activity and no photoelectronic structural change over four successive cycles (Fig. 19c).

In a systematic comparative study on alkali metal-doped g-C_3N_4 for photocatalytic hydrogen production under visible-light illumination, Jiang *et al.* evaluated the impact of Li, Na, and K doping on the photocatalytic H_2 evolution of g-C_3N_4.[45] Among all the alkali metals tested, Na-doped g-C_3N_4 demonstrated the best performance, achieving a hydrogen evolution rate of 18.7 μmol h^{-1}, nearly 3.7 times higher relative to pristine g-C_3N_4 and approximately twice that of K-doped g-C_3N_4. This outstanding performance of Na–g-C_3N_4 was ascribed to its finely tuned microstructure, improved light-harvesting ability, and optimized band structure, which together enabled superior charge carrier separation and enhanced charge transfer ability. Electrochemical analyses confirmed that Na doping led to the highest photocurrent response and the lowest charge transfer resistance, while photoluminescence (PL) spectra revealed suppressed

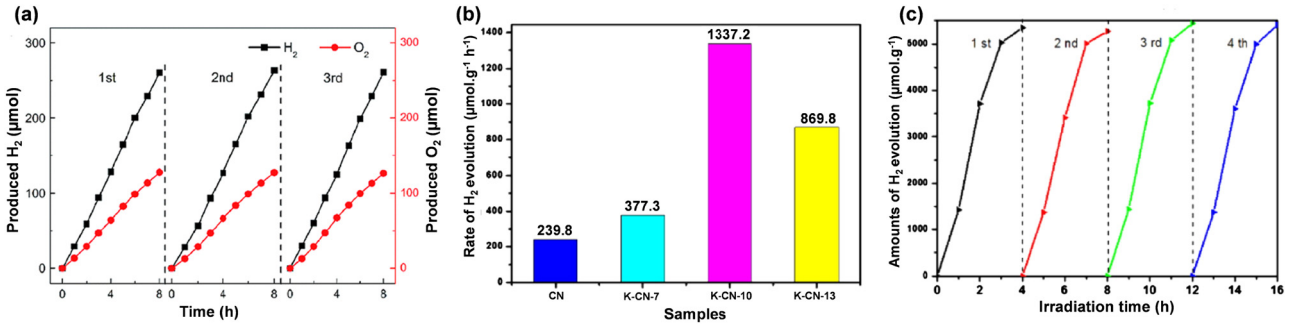

Fig. 19 (a) Cyclic test for H_2 and O_2 evolution over Na–CN. Reproduced with permission from ref. 86. Copyright 2016, Royal Society of Chemistry. (b) Photocatalytic activity towards H_2 production from water, and (c) photostability test over K–CN-10. Reproduced with permission from ref. 88. Copyright 2018, Elsevier.

radiative recombination. Collectively, these results demonstrate that Na is the most effective alkali dopant in g-C_3N_4 for boosting the photocatalytic H_2 generation under visible light.

Strategic co-doping of alkali metals with complementary metal or non-metal dopants into the g-C_3N_4 host framework tailors its electronic configuration, leading to band gap modulation and boosting charge separation kinetics, which can lead to superior photocatalytic efficiency. For instance, Guo *et al.* reported K, I co-doped mesoporous g-C_3N_4 (MP–CN–KI) for photocatalytic H_2 production, synthesized by one-pot thermal polymerization of dicyandiamide, SBA-15 hard-template, and KI (Fig. 20a).[135] The successful formation of mesoporous g-C_3N_4 co-doped with K and I was validated through the combined characterization of BET, XRD, SEM, TEM, and XPS analyses. The resultant MP–CN–KI exhibited a type IV isotherm with H1 and H3 hysteresis loops and a BET surface area of 71.48 $m^2\ g^{-1}$, which was around 8.6 times higher than that of the bulk g-C_3N_4. FT-IR analysis suggested the existence of the azide group, which could be due to the SBA-15-mediated synthesis and K, I doping. Furthermore, the SBA-15 driven mesopores led to the formation of numerous uncondensed surface exposed amine groups as confirmed from the broadening of the N–H stretching frequency in the range of 2900–3500 cm^{-1}. The microstructure analysis from SEM and TEM measurements suggested a rod-like morphology with numerous porous channels decorated on the surface of MP–CN–KI, suggesting better charge diffusion by reducing

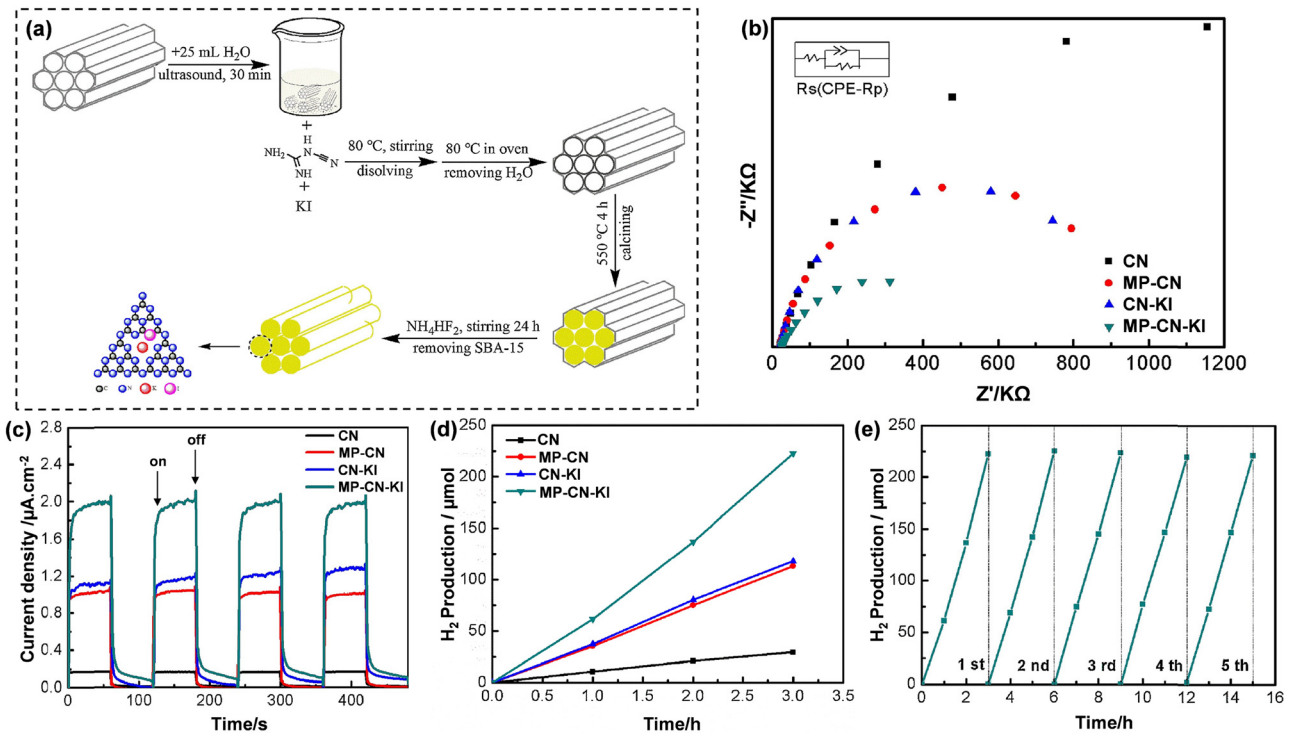

Fig. 20 (a) Diagrammatic sketch for the formation of MP–CN–KI, (b) EIS Nyquist plots, (c) transient photocurrent response, (d) photocatalytic H_2 evolution of all the synthesized samples, and (e) cyclic stability of MP–CN–KI under visible light illumination. Reproduced with permission from ref. 135. Copyright 2018, Elsevier.

the paths and easing the migration of charges from the bulk to the surface. Moreover, the K and I incorporation led to the improved charge conductance; hence, the combination of the mesoporous framework with appropriate K and I doping resulted in a significant quenching in the PL-emission peak for MP–CN–KI compared to the pristine CN. MP–CN–KI exhibited improved light harvesting with a narrowed band gap energy and a red shift in light absorption, due to the synergistic effect of mesoporous creation along with the K and I co-doping. Overall, the ease of charge diffusion, better charge separation, improved optoelectronic features, and enhanced charge carriers' lifetimes due to the mesoporous framework, along with the K, I doping, synergistically enhanced the photocatalytic H_2 evolution rate to 81 μmol h^{-1} for MP–CN–KI, which is 10-fold greater than bulk CN (Fig. 20b–e). The robust framework of MP–CN–KI exhibited an impressive photostability even after 5 consecutive cycles.

Again, Fang *et al.* demonstrated Na, O-co-doped g-C_3N_4 synthesized *via* the solvothermal method, followed by the calcination to amplify the H_2 production rate.[136] The resultant Na, O-co-doped g-C_3N_4 is a highly crystalline material having enhanced optoelectronic features relative to bulk g-C_3N_4. The successful incorporation of the O-atom modified the band gap energy level by creating structural defect states due to the interference of the O 2p orbitals, which have a potential lower than the N 2p orbitals. Furthermore, the substitutional doping of N atoms by O atoms liberated additional electrons, which were restricted within the range of π-delocalization and contributed to the defect states. Na,O-co-doped g-C_3N_4 exhibited a visible-light-mediated H_2 production rate of 810 μmol h^{-1} with a quantum yield of 22.3%. Similarly, another report of co-doping by Cao *et al.* demonstrated the synthesis of P and Na co-doped g-C_3N_4 (Na–P co-doped g-C_3N_4) through pyrolysis of melamine with a very low amount of sodium tripolyphosphate as the precursor for Na and P.[137] The controlled doping (0.01 wt%) of Na and P resulted in an interstitial doping of Na and P, which can be evidenced by DFT calculation (Fig. 21a). The two non-equivalent C-atoms and three non-equivalent N-atoms of the tri-*s*-triazine of g-C_3N_4 can accommodate the Na and P atoms in two interstitial sites. Although trace amounts of doping (below 0.1%) didn't show any remarkable change in absorption edge, with increasing the amount of doping (1–3%), the absorption edge was progressively red-shifted. XPS analysis comprises a peak at 133.7 eV, attributed to the P–N bonding, while another peak at 1070.33 eV, representing the Na 1s species, existed as Na–N binding sites in Na–P co-doped g-C_3N_4. A slight negative shift in the binding energy of the Na–N bond was observed, which was due to the strong coordination of the lone pair of the N-atom and the Na atoms during thermal treatment, confirming the interstitial doping of Na in Na–P co-doped g-C_3N_4. Furthermore, the in-depth electronic structure was estimated by DFT calculations, where the TDOS analysis revealed that the valence band maxima of both g-C_3N_4 and Na–P co-doped g-C_3N_4 were composed of N atoms, while the conduction band minima of g-C_3N_4 was composed of the contributions of C and N atoms. However, the conduction band minima of Na–P co-doped g-C_3N_4 were constructed by P, C, and N atoms, resulting in the extended π delocalization of the photoexcited e^- *via* a charge transport channel due to 'P'

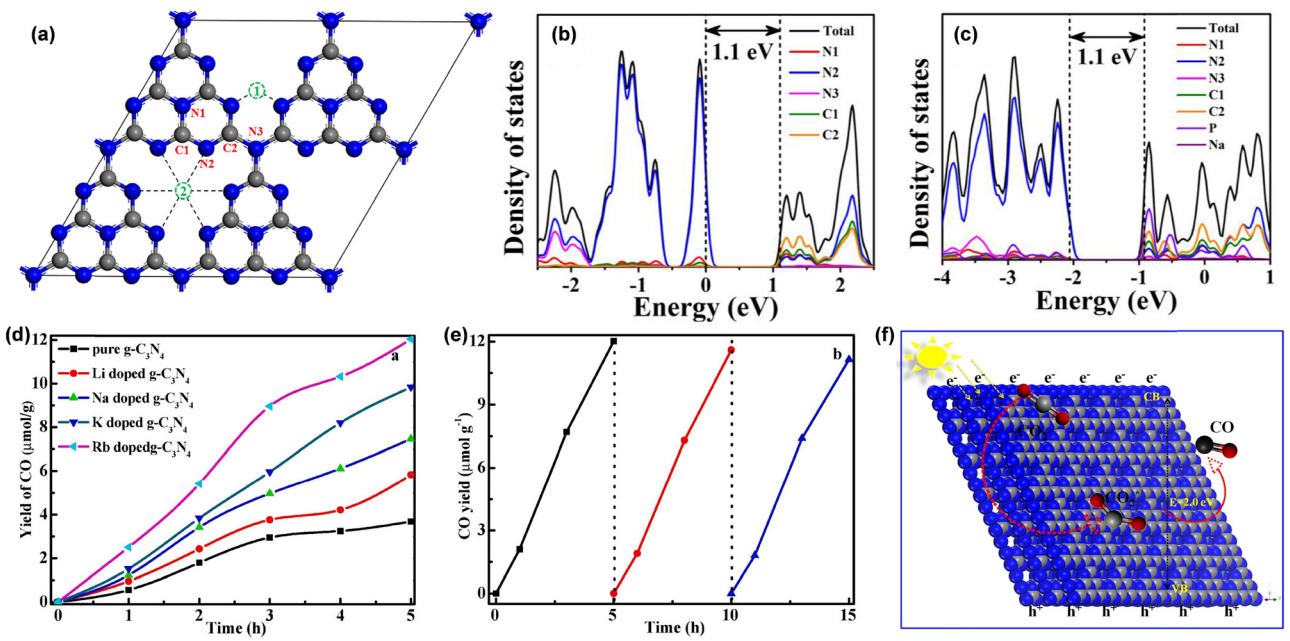

Fig. 21 (a) Optimized model of g-C_3N_4 demonstrating the interstitial doping sites (positions 1 and 2 represent the doping sites for P and Na, respectively) and the calculated density of states (DOS) for (b) g-C_3N_4 and (c) Na–P co-doped g-C_3N_4. Reproduced with permission from ref. 137. Copyright 2017, Elsevier. (d) CO generation rate of pure g-C_3N_4 and various alkali metal-doped g-C_3N_4 photocatalysts, (e) cycling stability performance of Rb–CN, and (f) a schematic figure showing how the charge transfer pathway in Rb–CN for CO_2 photoreduction. Reproduced with permission from ref. 96. Copyright 2020, Elsevier.

bridging (Fig. 21b and c). In contrast, Na doping facilitated the increase in the charge density due to its electron donation ability to adjacent N atoms in Na–P co-doped g-C_3N_4. Overall, the controlled dual doping of Na and P in Na–P co-doped g-C_3N_4 led to exposed surface-active sites, excellent charge migration, better charge separation, and high surface charge density, caused the directional flow of photogenerated e^- and minimized the reaction barrier for H_2 evolution, thereby displaying an enhanced H_2 production of 191.0 μmol h^{-1} (2.2 times higher than that of g-C_3N_4) under visible light.

Zhu *et al.* synthesized a series of K and halogen (F, Cl, Br, and I) co-doped g-C_3N_4 photocatalysts by a simple single-pot thermal condensation to evaluate their hydrogen evolution performance.[138] Among all the synthesized doped systems, K, F co-doped g-C_3N_4 (F–K–C_3N_4) demonstrated the highest photocatalytic activity, with a H_2 evolution rate of 1039 μmol h^{-1}, approximately 8.5 times more than bulk g-C_3N_4. This amplification in the photoactivity was primarily attributed to the combined effect of K^+ and F^- dopants. The construction of robust C–F and C–K bonds not only induced a red shift in the light absorption but also effectively tuned the band structure and improved charge carrier separation. Furthermore, the introduction of K^+ ions created an internal electric field within the g-C_3N_4 matrix, which promotes the directional charge transport in the resultant material.

3.1.2. Photocatalytic CO_2 reduction. The photo-assisted CO_2 reduction to produce a wide range of sustainable hydrocarbon fuels presents a significant strategy to mitigate various environmental issues, including global warming.[139–141] However, the inherent thermodynamic stability of the CO_2 molecule is attributed to its strong C═O bond, with its high bond strength of 750 kJ mol^{-1}, which impedes adsorption and activation on the photocatalytic surface. Hence, high energy is required to activate the C═O bond for respective hydrocarbon conversion.[25,78,140–144] The efficacy of a semiconductor photocatalyst in this process is governed by band structure alignment, *i.e.*, the CB minima position must be more negative to thermodynamically drive the CO_2 reduction reaction, and the VB maxima must be more positive to promote hole scavenging. The photocatalytic CO_2 reduction can be either a single-electron or a multi-electron reduction process. In the former case, *i.e.*, the single-electron CO_2 reduction process ($CO_2 + e^- \rightarrow CO_2^{\bullet -}$) is thermodynamically infeasible, as this process is associated with a highly negative redox potential of 1.85 V *vs.* NHE.[141–145] However, a viable photocatalytic pathway typically involves a multi-electron, proton-coupled reaction that requires relatively less negative reduction potential. The product selectivities for CO_2 photoreduction and conversion efficiency are further complicated by competing kinetic and thermodynamic factors. For instance, the photoreduction of CO_2 to CH_4 by $8e^-$ reduction is thermodynamically favorable and is kinetically constrained. Conversely, reduction pathways involving a lower number of e^-, such as CO or HCOOH production, often exhibit faster kinetics but may be less thermodynamically favorable.[143–145] Various photoreduced products of CO_2 photoreduction with respect to the number of photogenerated e^- and reduction potential values are given below (eqn (4)–(12)),

$$CO_2 + e^- \rightarrow CO_2^{\bullet -}, \quad E^\circ = -1.85\ V \tag{4}$$

$$CO_2 + 2H^+ + 2e^- \rightarrow HCOOH, \quad E^\circ = -0.61\ V \tag{5}$$

$$CO_2 + 2H^+ + 2e^- \rightarrow CO + H_2O, \quad E^\circ = -0.53\ V \tag{6}$$

$$CO_2 + 4H^+ + 4e^- \rightarrow HCHO + H_2O, \quad E^\circ = -0.48\ V \tag{7}$$

$$CO_2 + 6H^+ + 6e^- \rightarrow CH_3OH + H_2O, \quad E^\circ = -0.38\ V \tag{8}$$

$$CO_2 + 8H^+ + 8e^- \rightarrow CH_4 + 2H_2O, \quad E^\circ = -0.24\ V \tag{9}$$

$$2H_2O + 4h^+ \rightarrow O_2 + 4H^+, \quad E^\circ = +0.81\ V \tag{10}$$

$$H_2O + h^+ \rightarrow OH^\bullet + H^+, \quad E^\circ = +2.31\ V \tag{11}$$

$$2H^+ + 2e^- \rightarrow H_2, \quad E^\circ = -0.42\ V \tag{12}$$

It can be seen that the relative energies of key intermediates significantly influence the product selectivity. Moreover, the optimum photocatalyst surface dictates the CO_2 adsorption extent and the respective band structure favors the specific multi-electron reduction process to achieve better selectivities for the CO_2 photoreduction process.[146–149] The g-C_3N_4 surface facilitates optimum adsorption and activation of CO_2, but due to its unsuitable CB position, the photoreduction is not that effective. Therefore, the rational design of g-C_3N_4 *via* alkali metal doping precisely engineers its band edge positions to provide sufficient overpotential for the desired multi-electron CO_2 reduction, which is also considered a low-cost and environmentally benign technique. Several studies from the literature are discussed over alkali metal-doped g-C_3N_4-based photocatalysts.[80,91,96,114,150] For example, Zhang and coworkers demonstrated the photoelectric properties of pristine and alkali-doped (Li, Na, K, Rb) g-C_3N_4 and conducted a comparative study of photocatalytic CO_2 reduction.[96] Among all synthesized alkali-doped materials, Rb–g-C_3N_4 (Rb–CN) formed thin mesoporous nanosheets and showed red-shifted absorption with reduced band gap. Furthermore, Rb–CN displayed maximum photoconductivity and lowest electron transport resistance (confirmed from the EIS study), compared to other synthesized photocatalysts. The CO yields were 3.6, 5.8, 7.4, 9.8, and 12.1 μmol g^{-1} for bulk g-C_3N_4 and all the synthesized alkali-doped g-C_3N_4 (Fig. 21d). Among all, Rb–CN exhibited the maximum photoactivity and maintained excellent catalytic stability towards CO_2 photoreduction (Fig. 21e). The photoreduction process was accomplished with multiple reaction steps, where the CO_2 molecules got adsorbed onto the Rb-doped–g-C_3N_4, activated by the photoexcited charge carriers on the surface of Rb-doped–g-C_3N_4. As a result, the CO_2 molecule converted to a surface adsorbed $*CO_2$ active intermediate, which underwent a $2e^-$ reduction process to generate CO, as shown in Fig. 21f.

Similarly, to enhance CO_2 photoreduction activity, flaky g-C_3N_4 with Na-doped and N-defects, designated as bmw-DCN-*x* (where *x* = 10, 20, 30, 40, NaCl: DCDA mass ratio), was fabricated using NaCl and DCDA as precursors (Fig. 22a).[151] NaCl acted both as a Na source and a structure-directing agent to generate N defects at the interlayer edges while creating a flaky morphology of g-C_3N_4. FT-IR revealed that bmw-DCN-*x*

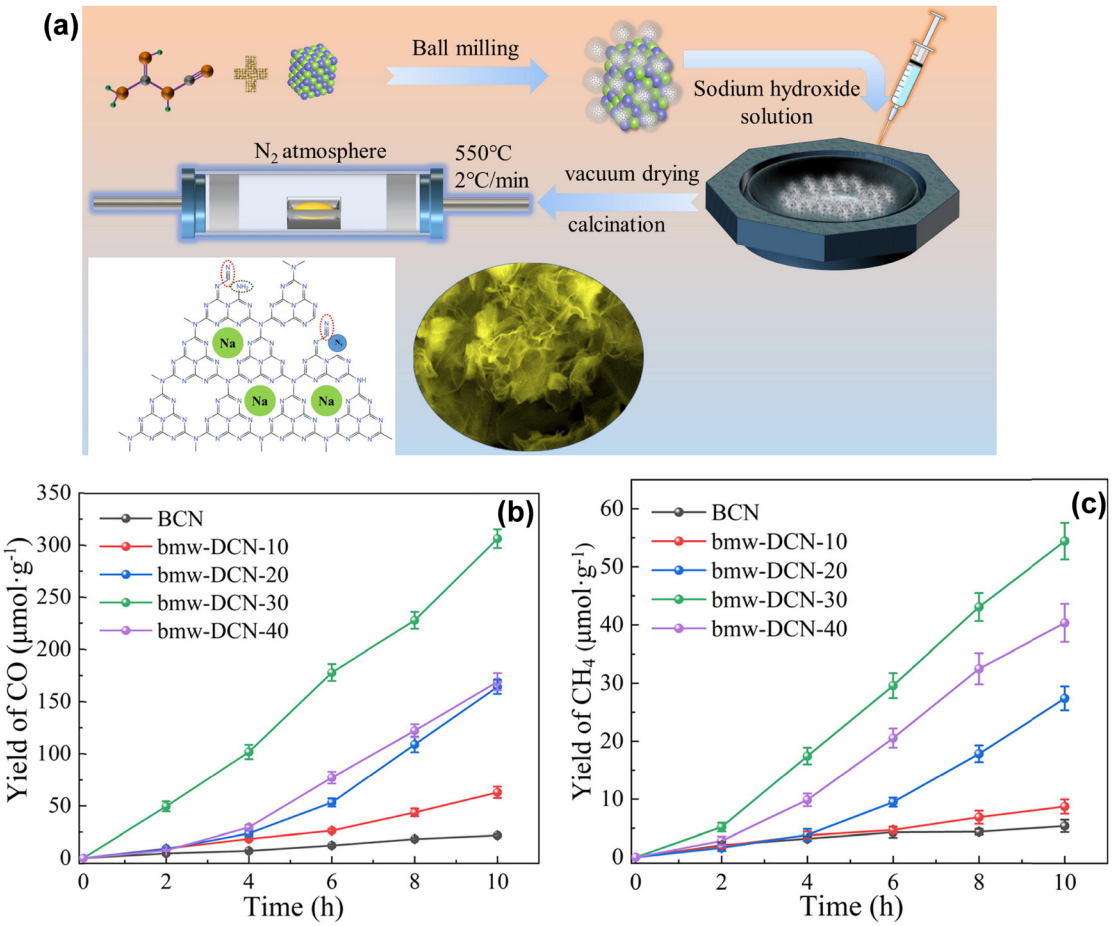

Fig. 22 (a) Diagrammatic illustration of the synthesis of Na-doped flaky g-C_3N_4 with N-defects, (b) CO and (c) CH_4 evolution rates of BCN and bmw-DCN-*x*. Reproduced with permission from ref. 151. Copyright 2021, Elsevier.

exhibited an additional band at 2177 cm^{-1}, corresponding to the existence of –C≡N groups. In contrast, this peak was absent in bulk g-CN. The formation of Na-doping and N-defect was evidenced by XPS and EPR analyses. The combinational effect of Na doping and N-defect led to optimization of the microstructure of bmw-DCN-30, which further endowed a narrower band gap, improved light harvesting, efficient charge separation, and excellent photoexciton migration. CO_2 adsorption capacity (both physical adsorption and chemical adsorption) substantially increased in bmw-DCN-30, compared to bulk-CN (BCN), attributed to the increase in surface basic sites on the photocatalyst. Similar to Lewis acid adsorption, CO_2 adsorbed on these basic sites with Na atoms and N defects likely serve as the active basic position, thereby improving the CO_2 adsorption and activation on the bmw-DCN-30 photocatalyst. This resulted in an optimal CO_2 photoreduction performance for bmw-DCN-30, achieving CO and CH_4 production rates of 30.6 μmol g^{-1} h^{-1} and 5.4 μmol g^{-1} h^{-1}, respectively, which were 15 and 11 times higher than that of BCN (Fig. 22b and c).

In another example, Debnath and coworkers presented a photocatalytic CO_2 conversion using K-doped g-C_3N_5 (g-C_3N_5):K(0.01) fabricated by thermal polymerization of 3-AT and KBr (Fig. 23a).[114] K-doped g-C_3N_5 exhibited an enhanced CO_2 photoreduction in visible light irradiation with a Pt cocatalyst. The CH_4 production rate reached 0.46 μmol g^{-1}, approximately 1.7 times and 2.7 times higher than that of g-C_3N_5 and g-C_3N_4, respectively. The azo linkage and K-doping reduced the band gap energy to about 1.9 eV, resulting in an enhanced visible light harvesting, as confirmed by UV-vis DRS analysis and DFT analysis (Fig. 23b). Additionally, K-doped g-C_3N_5 showed PL quenching, indicating suppressed e^-/h^+ recombination, facilitating better charge carrier separation and transfer (Fig. 23c and d). Furthermore, doping of K^+ in g-C_3N_5 provided more active sites for the CO_2 adsorption, contributing to higher photocatalytic CO_2 reduction activity, and maintained its performance stability over four consecutive cycles. According to the structure optimization analysis, as shown in Fig. 23e–g, the larger radius of K^+ didn't favor substitutional doping but resulted in an ion–dipole interaction between the N atom of g-C_3N_5 and K^+. This interaction augments optimized electronic adjustment and better charge transfer efficiency to boost the enhanced charge separation. As a result, K-doped g-C_3N_5 exhibited photoreduction of CO_2 to CH_4 with 100% selectivity. Likewise, a K^+ intercalated ultrathin g-C_3N_4 nanosheet (denoted as CNS K) was reported for CO_2 reduction.[150] The photocatalyst was synthesized *via* H-bonding self-assembly followed by thermal condensation of DCDA and KOH. CNS K

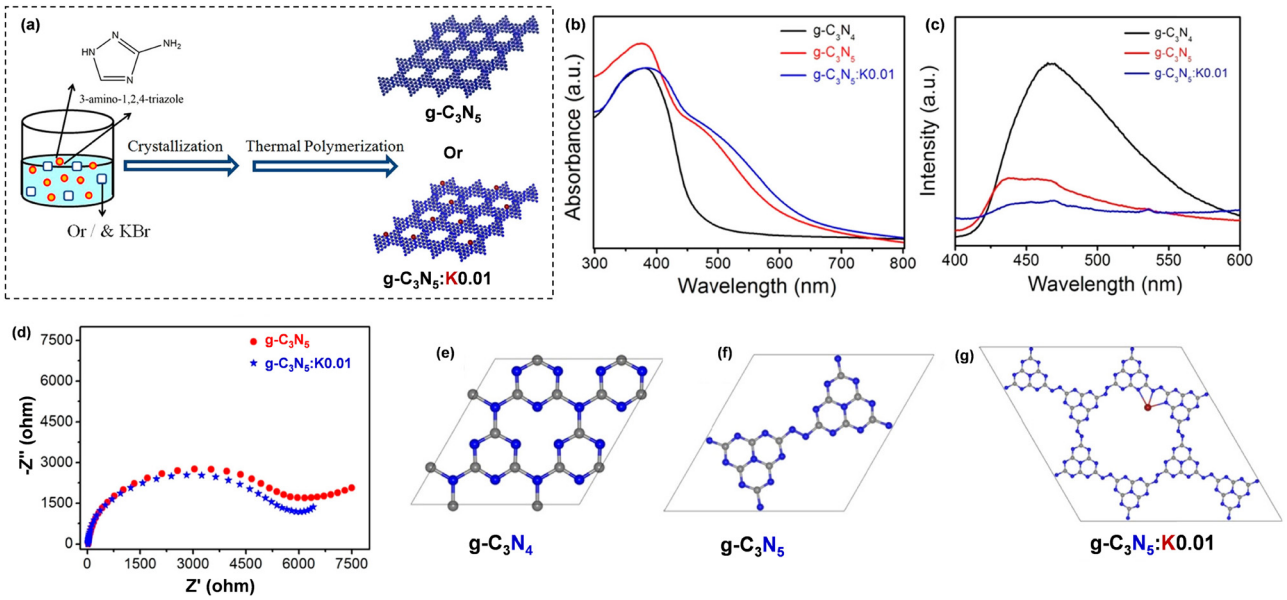

Fig. 23 (a) Schematic depiction of the synthesis of g-C_3N_5 and g-C_3N_5:K(0.01), (b) UV-vis DRS, (c) PL spectra, (d) EIS Nyquist plots of the synthesized samples, and (e)–(g) crystal structure models of g-C_3N_4, g-C_3N_5, and g-C_3N_5:K(0.01), respectively. Reproduced with permission from ref. 114. Copyright 2022, American Chemical Society.

exhibited an enhanced photocatalytic performance, achieving CO and CH_4 at a production rate of 1.65 μmol g^{-1} h^{-1} and 0.15 μmol g^{-1} h^{-1}, respectively. The introduction of K^+ into the g-C_3N_4 interlayers broadens the optical absorption, thereby modifying the band energy structure and also shortening the charge carrier migration to accelerate e^- transfer. Additionally, K^+ intercalation created built-in electric fields that restrained the charge recombination and increased surface amino groups, enhancing CO_2 adsorption. The *in situ* DRIFT analysis evidenced that the infrared absorption peaks correspond to the intermediates such as b-CO_3^{2-}, m-CO_3^{2-}, CO_3^{2-}, and HCO_3^-, confirming stronger CO_2 adsorption and activation on the CNS K surface.

3.1.3. Photocatalytic H_2O_2 production. The photocatalytic production of H_2O_2 from H_2O and O_2 is an endergonic process, requiring a Gibbs free energy of 117 kJ mol^{-1}, which proceeds *via* two photochemical pathways: (a) the water oxidation reaction (WOR) and (b) the oxygen reduction reaction (ORR). The WOR is a thermodynamically challenging process because it is associated with more complex kinetics and requires a much higher positive oxidation potential to achieve. In contrast, the photocatalytic H_2O_2 production is usually achieved *via* the ORR pathway over an alkali metal-doped g-C_3N_4 photocatalyst. The ORR pathway can be accomplished by two distinct routes: (i) a two-electron single-step reduction process and (ii) a one-electron two-step reduction process. In the first pathway, O_2 is converted directly to H_2O_2 by accepting $2e^-$ and $2H^+$ in a single step known as the concerted $2e^-$ ORR (eqn (13)). In the other way, the second pathway involves the formation of the superoxide radical ($O_2^{\bullet-}$) by the reduction of O_2 with one e^-, as shown in eqn (14). Finally, the generated $O_2^{\bullet-}$ active species reacts with $2H^+$ and e^- to produce H_2O_2 (eqn (15)).[25,152–155]

Two-electron single-step ORR:

$$O_2 + 2H^+ + 2e^- \rightarrow H_2O_2 \quad (E^\circ = +0.68\ \text{V } \textit{vs.}\ \text{NHE}) \tag{13}$$

One-electron two-step ORR:

$$O_2 + e^- \rightarrow O_2^{\bullet-} \quad (E^\circ = -0.33\ \text{V } \textit{vs.}\ \text{NHE}) \tag{14}$$

$$O_2^{\bullet-} + 2H^+ + e^- \rightarrow H_2O_2 \quad (E^\circ = +1.44\ \text{V } \textit{vs.}\ \text{NHE}) \tag{15}$$

The presence of appropriate surface-active sites and a necessary band structure in alkali-doped g-C_3N_4 is crucial to accomplish both the reaction pathways for efficient H_2O_2 production.[43,156–161] For instance, the Na-doped g-C_3N_4 photocatalyst (BNCN) was reported by Gou *et al.*, which acted as a three-dimensional charge carrier transport channel to facilitate efficient H_2O_2 production.[156] BNCN was fabricated by a double pyrolysis method where dicyandiamide and NH_4Cl were first calcined to produce g-C_3N_4, which was subsequently pyrolyzed under an Ar atmosphere with $NaBH_4$ and sodium acetate to form BNCN (Fig. 24a). The resultant BNCN, having Na intercalation and –C≡N anchoring moieties, possessed a lamellar curly-like structure, as analyzed from the SEM analysis. The successful –C≡N anchoring was understood from the FT-IR, solid state NMR, and XPS analyses. The Na intercalation was estimated by PXRD analysis, which observed the shifting of the (002) plane towards a lower angle, suggesting the positioning of Na within the interlayers of g-C_3N_4. As a whole, the respective modification could form a 3D charge carrier transport channel in BNCN, as demonstrated in Fig. 24b. Due to this, an enhanced degree of electronic delocalization and promotional effects of interlayer charge transportation can be experienced. The synergistic effect of the Na doping and –C≡N grafting led to modifying the band structure of BNCN, due to which it exhibited an extended

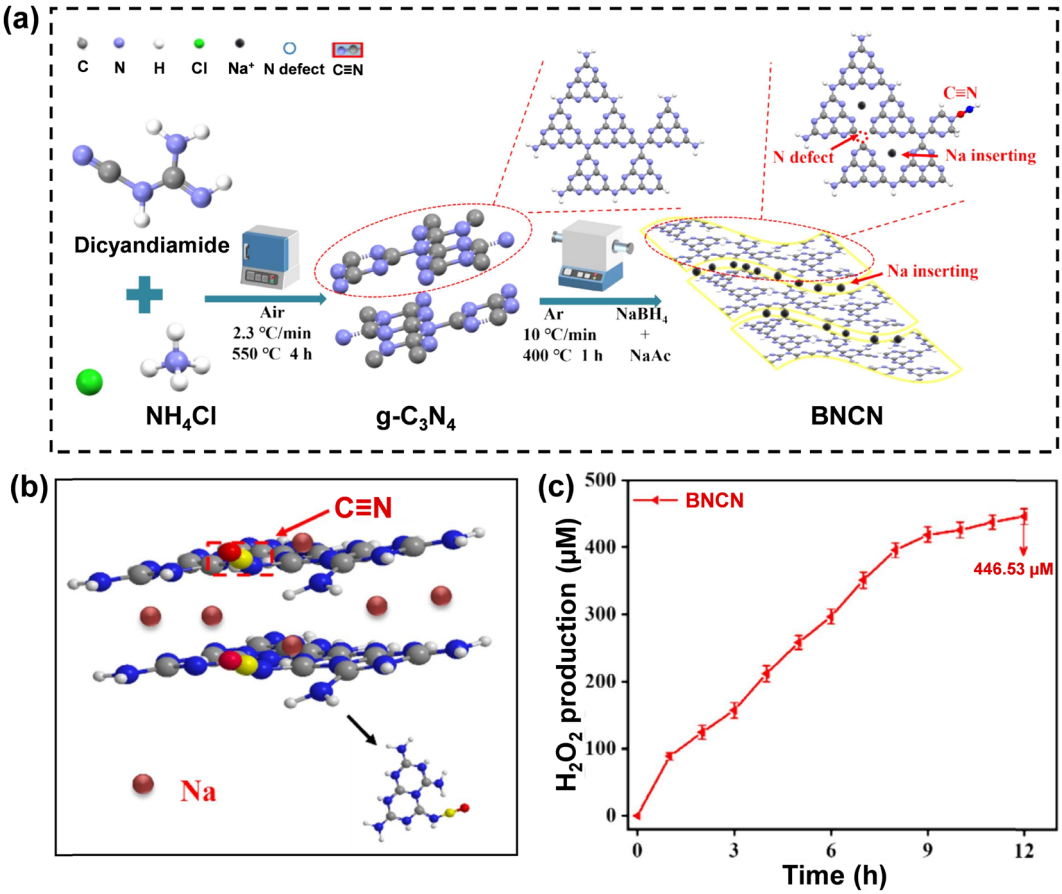

Fig. 24 (a) Diagrammatic sketch of BNCN formation, (b) a schematic showing the 3D charge transport pathway, and (c) photocatalytic H_2O_2 production in 12 h. Reproduced with permission from ref. 156. Copyright 2025, Elsevier.

light absorption ability with a narrower band gap. The modified band structure in BNCN has a more negative CB potential, which suitably facilitates the reduction of O_2 to H_2O_2. The 3D transport channel, due to the –C≡N moiety and Na intercalation, directed the charge density to form an internal electric field (IEF), which promoted the charge separation efficiency. Furthermore, O_2-TPD analysis suggested that BNCN exhibited better O_2 adsorption efficiency, which is a key step of the O_2 reduction. Various trapping experiments and controlled reactions confirmed that the $O_2^{\bullet-}$ was the active intermediate in H_2O_2 formation, which was obtained by the reduction of O_2 by photogenerated e^-. Fig. 24c demonstrates that the efficient H_2O_2 production was dominated by the 3D transport channel of BNCN, where the effective IEF could efficiently separate the charge pairs and the intercalated Na atoms, further triggering the charge transportation longitudinally to promote further charge separation. As a result, more photoexcited e^- were involved in the O_2 reduction and exclusively formed H_2O_2.

Another example demonstrated that the 'K' doping promotes faster space charge transmission, followed by the efficient charge carrier separation to exhibit better H_2O_2 production.[157] KBr guided calcination of thiourea led to the formation of K and Br doped g-C_3N_4 (K–CN). The K^+ was reported to be retained in the interstitial cavity of the heptazine ring, which was confirmed from the PXRD analysis. KBr-mediated synthesis modified the framework structure, which can be understood from the FT-IR and XPS analyses. FT-IR analysis demonstrated that after the K doping, a stretching frequency at 2177 cm^{-1} corresponding to –C≡N linkage was observed in the K–CN framework. Moreover, the bending frequency at 805 cm^{-1} corresponding to the heptazine ring gradually diminished due to the increasing content of K, suggesting that the heptazine ring transformed into –C≡N moieties. The C 1s spectra of K–CN exhibited a new peak at 286.4 eV, which was attributed to –C≡N and was absent in PCN, without K-doped material. This further clarifies that the –C≡N linkages were formed due to K doping. Furthermore, the peak position of C 1s and N 1s of K–CN was noticeably changed to that of the PCN, suggesting that the electronic structure got altered due to the K doping. K–CN exhibited a redshift light absorption because of the electron-withdrawing nature of –C≡N linkages present in the K–CN framework. The PL analysis suggested that the K doping significantly reduced the PL intensity by efficiently inhibiting the charge recombination process. The K present in the interlayers of K–CN promotes the charge separation by facilitating the flow of e^- among the interlayers of K–CN, while the –C≡N moieties, being electronegative in nature, could trap the photoexcited e^- and enhance the charge separation process. As a result, K–CN exhibited a smaller EIS radius and higher photocurrent density than PCN, indicating that K–CN possessed

better photogenerated electron mobility with efficient charge separation (Fig. 25a and b). The linear sweep voltammetry (LSV) curve using rotating disk electrode (RDE) test was carried out to reveal that the photocatalytic H_2O_2 process involved a $2e^-$ reduction process. Furthermore, the scavenging test confirmed that the photocatalytic H_2O_2 production was achieved by a two-step one-electron ORR process in which $O_2^{\bullet-}$ and $^1O_2$ were the sole reactive oxygen species (ROS). It was also reported that the Br^- in K–CN could promote the formation of $^1O_2$ to expedite the H_2O_2 production rate. Based on the control experiment, the photocatalytic H_2O_2 efficiency was governed by the O_2 adsorption ability, which was used as a feedstock. K–CN exhibited a comparatively stronger O_2-TPD signal and possessed a lower ΔG value of K–CN from DFT calculations, suggesting a better O_2 adsorption ability of KCN than PCN. The photocatalytic mechanism of H_2O_2 production over the K–CN photocatalyst involved a two-step single-electron oxygen reduction pathway and energy transfer pathway, which was initiated by the formation of photoinduced charge carriers upon light irradiation. As a result, the photogenerated h^+ oxidized the adsorbed ethanol to produce H^+, while the photogenerated e^- reduced O_2 to $O_2^{\bullet-}$. The resultant H^+ and $O_2^{\bullet-}$ reacted to produce $^\bullet$OOH reactive species, which were reduced to HO_2^- species and subsequently interacted with H^+ to produce H_2O_2. Additionally, the energy transfer process facilitated the conversion of O_2 to $^1O_2$ through intersystem crossing (ISC), which also participated in the H_2O_2 production, as shown in Fig. 25c.

Mandal *et al.* developed a photocatalyst (denoted as CKCN) by the simultaneous incorporation of K^+ ions and amorphous carbon in g-C_3N_4, significantly enhancing the photocatalytic production ability.[43] This dual-mode structural modification enhanced porosity, induced intra-band defects, and facilitated the distribution of exposed active sites, resulting in a H_2O_2 production of 9000 μmol g^{-1} h^{-1} with approximately 30% AQY under visible light irradiation. The elemental mapping analysis confirmed the homogeneous distribution of C, N, O, and K atoms, indicating successful doping of K atoms. The XRD analysis revealed the disordering of the CN framework and defect formation due to the dual incorporation effect. Furthermore, the EPR analysis suggested that CKCN exhibited an intensified signal of Lorentzian line compared to CN, which evidenced the formation of unpaired e^- due to N-vacancy and

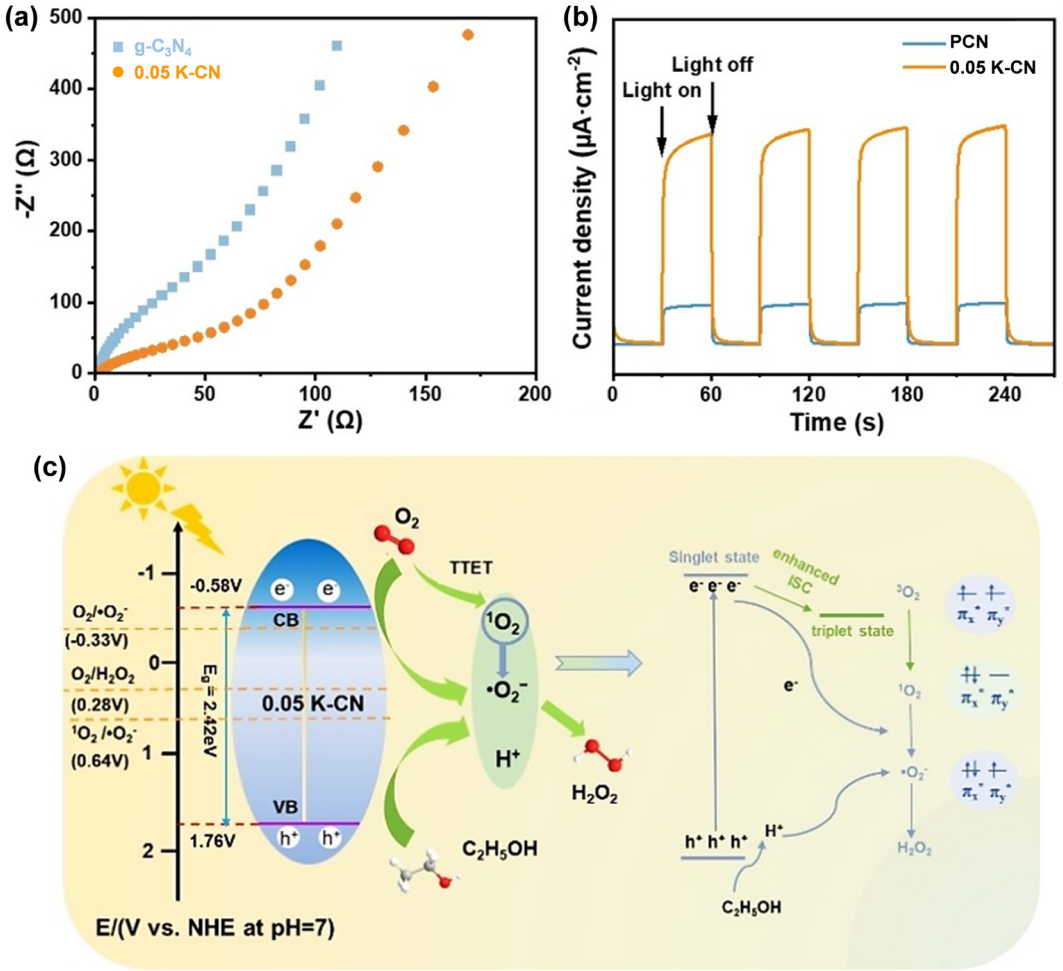

Fig. 25 (a) EIS curves, (b) transient photocurrent response of PCN and K–CN, respectively, (c) schematic representation of the proposed mechanism for photocatalytic H_2O_2 production. Reproduced with permission from ref. 157. Copyright 2025, Wiley-VCH.

the amorphous structure of CKCN. Again, CKCN exhibited a reduced band gap (2.68 eV), broader optical absorption, superior charge separation, and migration in CKCN, as evidenced through optoelectronic and electrochemical analyses. Moreover, the hole scavenger and spin trapping experiments confirmed that the H_2O_2 production over CKCN was dominated *via* the O_2 reduction pathway to form $O_2^{\bullet -}$ as an active intermediate. Furthermore, the band structure analysis found that the formation of CKCN was accomplished with a more negative CB level than g-C_3N_4, appropriate for the reduction of $O_2/O_2^{\bullet -}$, which augments the efficient H_2O_2 production.

3.1.4. Photocatalytic N_2 reduction. Photocatalytic N_2 fixation offers a promising alternative pathway for NH_3 synthesis under ambient conditions compared to the energy-intensive Haber–Bosch process. The reduction of N_2 to NH_3 is a challenging reaction due to its high thermodynamic barrier, primarily stemming from the molecule's inherent stability.[162–164] The exceptionally high bond dissociation energy of the N≡N bond (941 kJ mol^{-1}) restrains its adsorption and subsequent activation on the photocatalyst surface, thereby causing a potential barrier in N_2 photoreduction. In contrast, photocatalytic N_2 reduction offers a promising alternative pathway for NH_3 production under ambient conditions (ΔG° = 339 kJ mol^{-1}).[165–167] The mechanism of N_2 photoreduction over a photocatalyst surface to synthesize NH_3 includes two simultaneous processes. Upon light irradiation, the photogenerated h^+ in the VB splits H_2O to H^+ and O_2; this H^+ migrates to the CB to produce H_2. Again, at the CB, this H^+ can be utilized by the photogenerated e^- and N_2 to produce NH_3. The photoreduction of N_2 to NH_3 is a multi-electron reduction process that requires 6 e^- to be reduced, which is kinetically unfavorable. It is more crucial to drive the N_2 photoreduction over H_2O splitting. The redox potential of N_2/NH_3 is −0.922 V, which can be theoretically achieved due to the favorable CB position (approx. ∼0.9 V) of alkali-doped g-C_3N_4. Besides, the competitive photocatalytic process of H_2O splitting and N_2 reduction usually brings complexity to efficient N_2 reduction.[165–169] Moreover, the recombination of the exciton pair further slows down the N_2 reduction kinetics. However, the optimized microstructure and modulated defect engineering *via* alkali metal doping offer better N_2 photoreduction by overcoming the above bottlenecks.[170–172] The alkali-doped g-C_3N_4 photocatalytic systems also extend to the photocatalytic N_2 fixation due to the conducive band alignment and acceptable optoelectronic features.

Photoexcited electron–hole recombination can significantly hinder the rate of N_2 photofixation. By tailoring the microstructure environment and introducing alkali metal-induced defect sites, charge separation is exceptionally improved by mitigating their rapid recombination, which accelerates the photoreduction kinetics of N_2. Therefore, alkali-doped g-C_3N_4-based photocatalysts exhibit favorable band alignment and enhanced optoelectronic characteristics that support their ability to drive efficient photocatalytic N_2 fixation. For example, Gu *et al.* reported that three-dimensional microporous g-C_3N_4 with Li doping (Li-3D-GCN) was synthesized *via* an efficient template-free method.[173] The resultant Li-3D-GCN was characterized by PXRD analysis, suggesting the phase purity of the material. The (002) diffraction plane exhibited a noticeable shift towards a lower 2-theta value due to the expansion of the interlayer spacing after the Li doping (Fig. 26a). Furthermore, the Li doping caused a significant red shift in the optical absorption, as illustrated in Fig. 26b. The Li doping, along with porous and high surface area in Li-3D-GCN, reduced the band gap compared to bulk g-C_3N_4 and Li doped in bulk g-C_3N_4 (Li-GCN). The SSA of Li-3D-GCN was 59.5 $m^2\ g^{-1}$, which was very high compared to 7.9 $m^2\ g^{-1}$ for bulk g-C_3N_4 and 8.4 $m^2\ g^{-1}$ for Li-GCN, suggesting the unlocking of easy diffusion and accessible charge transportation in the Li-3D-GCN framework (Fig. 26c). The porous structure of Li-3D-GCN was further revealed by the morphology analysis. The formation of Li–N bonding sites was analyzed by the XPS analysis, which acted as the active center for the photocatalytic N_2 reduction. The N 1s peak was distinctly shifted after the Li doping, suggesting that the unsaturated e^- on the N atom is more localized towards the Li atom due to the Li–N coordinate interaction. N_2-TPD analysis and DFT calculation confirmed the potential N_2 adsorption ability of Li-3D-GCN (Fig. 26d and e). The porous framework in Li-3D-GCN allowed more exposed Li–N bonding sites, which efficiently adsorbed N_2 molecules. Furthermore, the Hirshfeld charge analysis showed that the Li doping can significantly increase the Hirshfeld charge of C and N atoms, which facilitates the efficient charge carrier flow in Li-3D-GCN to facilitate the more intense charge carrier separation. The charge density analysis also showed that the flow of e^- occurred from the Li atom of the Li–N bonding sites to N_2 to accomplish the photoreduction process (Fig. 26f). As a result, Li-3D-GCN exhibited a superior NH_4^+ production of 4.8 mg $L^{-1}\ h^{-1}\ g_{cat}^{-1}$, which was 2.5 and 20 times higher than that of Li-GCN and bulk g-C_3N_4, respectively.

Similarly, another example demonstrates that the effect of appropriate co-doping can significantly boost the N_2 photoreduction process.[174] A series of alkali-doped g-C_3N_4 crystalline materials, such as LK-HTCN (Li–K co-doping), KN-HCN (K–Na co-doping), LKN-HTCN (Li–K–Na co-doping), and LN-HTCN (Li–Na co-doping), were synthesized using the systematic combination of appropriate alkali metal precursors (Fig. 27a). The phase purity and crystallinity of the synthesized material were determined by the PXRD analysis, which suggested that Li doping promoted the construction of the triazine phase, whereas K and Na promoted the development of the heptazine phase (Fig. 27b). FT-IR analysis confirmed the existence of –C≡N linkages, and its peak intensity was comparatively higher in KN-HCN than that in LK-HTCN, LKN-HTC, and LN-HTCN, corroborating the influential nature of K^+ optimizing the microstructure and promoting more –C≡N linkages for enhanced optical properties and better charge carrier separation (Fig. 27c). Furthermore, the N vacancy was attributed to the strong EPR signal of KN-HCN, associated with a greater number of free e^- (Fig. 27d). The morphological analysis suggested that KN-HCN possessed a bulk structure, while LK-HTCN, LKN-HTCN, and LN-HTCN possessed nanorod structures. Moreover, the (002) in KN-HCN was wider than that of LK-HTCN, LKN-HTCN, suggesting the presence of heptazine phases due to the

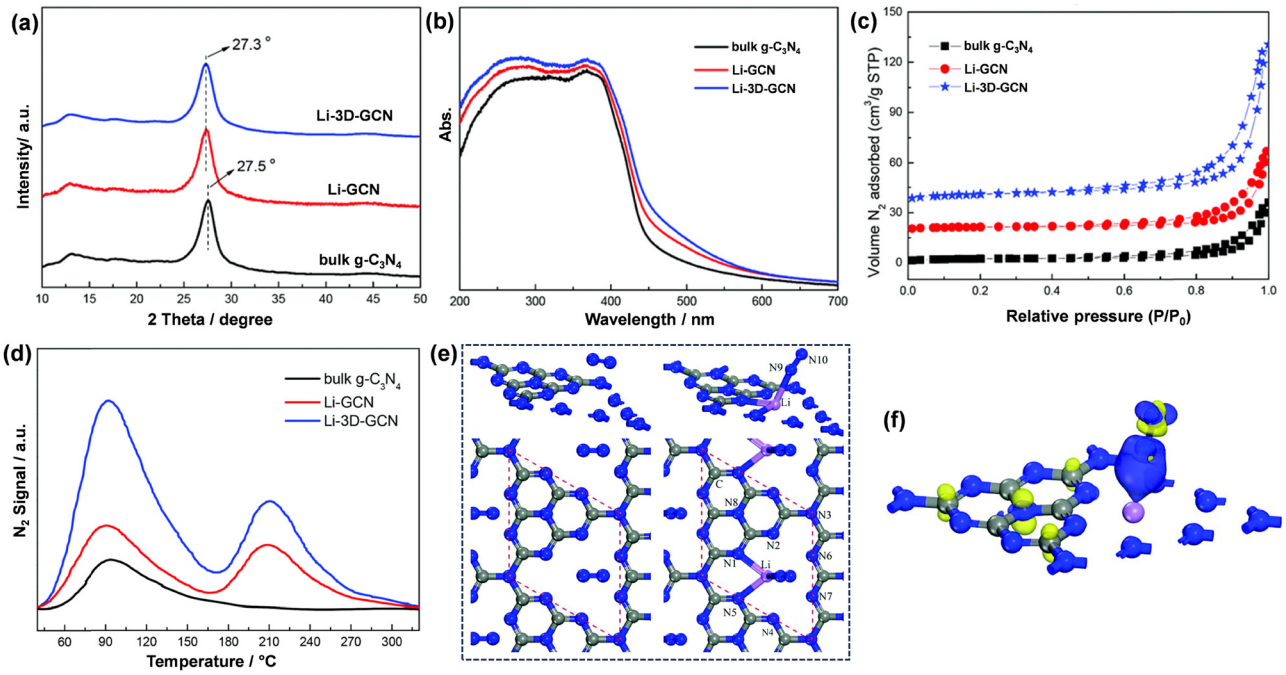

Fig. 26 (a) XRD patterns, (b) UV-vis absorption spectra, (c) N_2 adsorption–desorption isotherms, and (d) N_2-TPD of the synthesized catalysts, schematic representation of (e) optimized configuration of N_2 adsorption on bulk g-C_3N_4 and Li-3D-GCN, (f) charge density distribution for N_2 adsorption on Li-3D-GCN, where the yellow and blue regions denote charge accumulation and depletion, respectively. Reproduced with permission from ref. 173. Copyright 2019, Royal Society of Chemistry.

incomplete condensation process. The XPS analysis was employed to further confirm the existence of the –C≡N moieties as well as the formation of K–N bonding sites through ion–dipole interactions in the CN interlayers and in KN-HCN, which could act as charge transport channels and bridging layers for promoting the transportation and separation of charge carriers. The effective charge separation was further understood from the lower PL intensity of KN-HCN. The light absorption was significantly enhanced after the alkali doping and the formation of –C≡N linkages with crystalline phases in all the samples; however, KN-HCN exhibited a strong absorption edge with noticeable red shift in the optical absorption, which could be due to the relatively higher content of –C≡N linkages in its framework. The potential role of K and Na co-doping endowed KN-HCN with a stronger photocurrent density and better charge separation ability. As a result, among all the synthesized photocatalysts, KN-HCN exhibited the highest ammonia yield of 17.01 μmol g^{-1} h^{-1} while maintaining the photostability even after the fourth cycle, suggesting the robustness of KN-HCN in photocatalytic ammonia production (Fig. 27e). Furthermore, the variation of wavelength led to production of different amounts of NH_3, coinciding with the UV-vis analysis (Fig. 27f). The combinational effect of the –C≡N linkage and K–Na co-doping for the efficient ammonia production is demonstrated in Fig. 27g. In the photocatalytic N_2 reduction process, the photogenerated h^+ oxidized H_2O to O_2 and H^+, while the photoexcited e^-, upon coupling with H^+, reduced the surface-adsorbed N_2 to produce NH_3.

The demonstration of a wide range of the above-discussed case studies shows the promising aspects of the alkali metal doping approach in the g-C_3N_4 matrix for efficient solar energy conversion for sustainable fuel production. Besides these examples, Table 4 further summarizes a list of alkali-doped g-C_3N_4-based photocatalysts governing the production of a wide range of solar fuels.

3.2. Applications of alkali metal-doped g-C_3N_4 towards degradation and removal of contaminants

Over recent decades, the escalating contamination of water, soil and air has become a critical global challenge, driven significantly by industrial discharge and domestic wastewater. Various organic and inorganic contaminants, such as dyes (for example, methyl orange, methylene blue, RhB, *etc.*), antibiotics, insecticides, and other chemical pollutants, pose widespread concern to the ecosystem. Conventional methods, such as adsorption, membrane-based filtration, enzymatic degradation, and coagulation, are often incompetent to eradicate these potential pollutants or may generate harmful secondary by-products. Photocatalysis offers a promising and sustainable approach for degrading such pollutants. This process involves the acceleration of a photoreaction over a semiconductor photocatalyst under UV or visible light. g-C_3N_4 has emerged as a prominent photocatalyst for the degradation of pollutants.[181–184] When g-C_3N_4 absorbs photons possessing energy equal to or greater than its band gap, it generates photoexcitons, and these charge carriers initiate a series of redox reactions, forming reactive oxygen species (ROS) such as $OH^•$ and $O_2^{•-}$. These ROS are highly active and are capable of derivatizing the complex pollutants into simpler, non-toxic compounds. Precisely, the critical aspect of heterogeneous photocatalysis is photo-

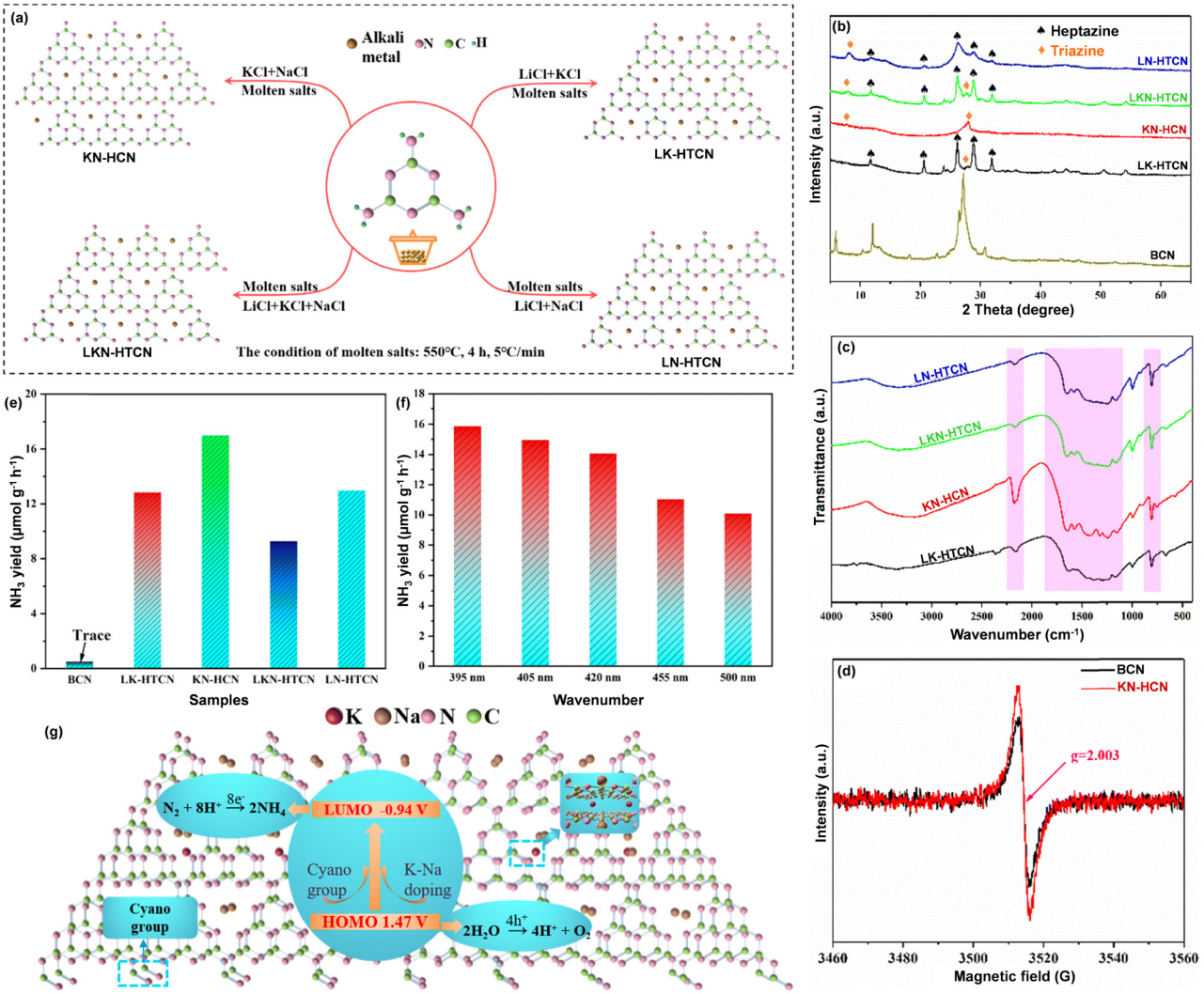

Fig. 27 (a) Diagrammatic sketch for the synthesis routes for the obtained samples, (b) XRD, (c) FT-IR spectra of LK-HTCN, KN-HCN, LKN-HTCN, and LN-HTCN, respectively, (d) EPR spectra of BCN and KN-HCN, (e) NH_3 production rate of all the prepared samples, (f) NH_3 production of KN-HCN at different wavelengths, and (g) illustration of the proposed photocatalytic N_2 reduction over KN-HCN. Reproduced with permission from ref. 174. Copyright 2022, Royal Society of Chemistry.

assisted oxidation of pollutants to benign substances. The underlying mechanism encompasses the generation of excitons and the subsequent pollutant degradation, depicted by the following equations (eqn (16)–(22)):

$$GCN + h\nu \rightarrow e^- + h^+ \quad (16)$$

$$h^+ + OH^- \rightarrow OH^\bullet \quad (17)$$

$$h^+ + H_2O \rightarrow OH^\bullet + H^+ \quad (18)$$

$$e^- + O_2 \rightarrow O_2^{\bullet -} \quad (19)$$

$$h^+ + \text{pollutants} \rightarrow \text{Oxidation products} \quad (20)$$

$$e^- + \text{pollutants} \rightarrow \text{Reduction products} \quad (21)$$

$$OH^\bullet + \text{pollutants} \rightarrow \text{Degradation products} \quad (22)$$

As mentioned in the earlier section, the pristine structure of g-C_3N_4 lacks structural demerits, causing limited optoelectronic features, but the recent studies demonstrate that the alkali metal ion incorporation can effectively provide more exposed active sites, suppress the charge recombination rates, and create transport channels for photoexcited e^- to boost the photocatalytic activity.[185–188]

As demonstrated by Ma *et al.*, the Li-doping, along with variable concentration of Ag nanoparticles deposition, effectively tuned the optical absorption and altered the band alignment of g-C_3N_4.[83] Li-doping and Ag deposition exhibited significantly higher photocatalytic performance, degrading RhB around 85% within 30 min while maintaining high photostability compared to pristine g-C_3N_4, Li-doped g-C_3N_4, and Ag/g-C_3N_4. The enhanced photodegradation efficiency of RhB was primarily ascribed to the improved charge separation induced by the modified band alignment due to Li incorporation, causing a positive shift of the valence band potential (from +1.57 V to +1.99 V), thereby promoting a more favorable oxidation process. Ag nanoparticles shrank

Table 4 List of alkali-doped g-C_3N_4-based photocatalysts employed for various solar fuel production

Photocatalysts	Precursors	Synthesis method	Type of solar fuel production	Light source	Yield	Ref.
NaK20-CN	Melamine, NaCl, KCl	Calcination	H_2 evolution	300 W Xe lamp	4502 μmol h^{-1} g^{-1}	58
KCN-75	Melamine, KCl flux	Thermal polymerization	H_2 evolution	300 W Xe lamp	382 mmol h^{-1}	75
CM-K_{12}	Melamine, cyanuric acid, potassium hydrogen phthalate	Supramolecular self-assembly, cross-linking polymerization	H_2 evolution	300 W Xe lamp ($\lambda \geq 420$ nm)	127.78 μmol h^{-1}	76
K–CN/ZCS	Urea, KCl, Cd $(CH_3COO)_2{\cdot}2H_2O$, Zn $(CH_3COO)_2{\cdot}2H_2O$, thioacetamide	Calcination, hydrothermal	H_2 evolution	300 W Xe lamp	9.606 mmol h^{-1} g^{-1}	93
2.5CCNC	Melamine, cesium acetate	Thermal polymerization	H_2 evolution	Xe lamp, 300 mW cm^{-2}	9.02 mmol g^{-1} h^{-1}	134
K(0.05)–CN	Melamine, C_2H_3KOS	Calcination	H_2 evolution	300 W Xe lamp ($\lambda \geq 420$ nm)	1319 μmol h^{-1} g^{-1}	175
K–CN/DFNS-2	Melamine, KOH, DFNS	Calcination	CO_2 reduction	300 W Xe lamp	1.7 mmol g^{-1} (CH_4)	80
g-C_3N_5:K0.01	3-Amino-1,2,4-triazole, KBr	Calcination	CO_2 reduction	300 W Xe lamp (λ = 385–740 nm)	0.752 μmol g^{-1} (CH_4)	114
CNS K	DCDA, KOH, poly-ethylene glycol	Calcination	CO_2 reduction	—	1.65 μmol g^{-1} h^{-1} (CO)	150
bmw-DCN-30	DCDA, NaCl	Calcination	CO_2 reduction	300 W Xe arc lamp ($\lambda > 400$ nm)	30.6 μmol g^{-1} h^{-1}	151
3 Na–CN	Dicyandiamide, $NaHSO_3$	Thermal polymerization	CO_2 reduction	300 W Xe lamp	21.5 μmol g^{-1} h^{-1} (CO)	176
K-gCN	DCDA, KOH	Calcination	CO_2 conversion	5 W LED bulb	1192 mg L^{-1} (formate)	177
CKCN	Urea, KNO_3	Calcination	H_2O_2 production	300 W Xe lamp	9000 μmol g^{-1} h^{-1}	43
10 wt% K–g-C_3N_4	DCDA, KI	Thermal polymerization	H_2O_2 production	Direct sunlight	200 μmol g^{-1} h^{-1}	46
KCN/ZnO	Melamine, KCl, LiCl, ZIF-8	Calcination	H_2O_2 production	AM 1.5	4.76 mM	50
MPCN	Urea, HCCP, KCl, LiCl	Thermal polymerization	H_2O_2 production	300 W Xe lamp ($\lambda > 420$ nm)	4424 μmol g^{-1} h^{-1}	107
0.05 K–CN	Thiourea, KBr	Calcination	O_2 reduction	10 W blue lamp (λ = 420–430 nm)	26 mmol g^{-1} h^{-1}	157
Li–C_3N_4	Urea, Li_2CO_3	Thermal polymerization	O_2 reduction	300 W Xe lamp, AM	920 mmol g^{-1}	158
KCT5-5	Urea, KCl, Ti_3AlC_2	Calcination, hydrothermal	H_2O_2 production	500 W Xe (λ = 420–780 nm)	3401 mmol L^{-1}	159
KCN-6	Melamine, KCl	Thermal polycondensation	H_2O_2 production	300 W Xe lamp ($\lambda > 420$ nm)	818.9 μmol g^{-1} h^{-1}	178
CN-KI_3-KI-MV	Melamine, KI	Oil bath reflux calcination	H_2O_2 production	300 W Xe lamp ($\lambda > 420$ nm)	46.40 mmol g^{-1} h^{-1}	179
K–g-C_3N_{4-x}	Melamine, potassium oxalate	Calcination	H_2O_2 production	300 W Xe lamp ($\lambda \geq 420$ nm)	706.9 μmol L^{-1}	180
Li-3D-GCN	Urea, LiCl	Thermal polymerization	N_2 fixation	250 W sodium lamp (λ = 400–800 nm)	4.8 mg L^{-1} h^{-1} g_{cat}^{-1}	173
KN-HCN	Melamine, KCl, NaCl	Calcination	N_2 fixation	300 W Xe lamp	17.01 μmol g^{-1} h^{-1}	174

the photogenerated e^- from the CB level of g-C_3N_4 by forming a Schottky barrier at the Ag/g-C_3N_4 interface. These e^- readily reacted with adsorbed O_2 to generate $O_2^{\bullet-}$ radicals, contributing to pollutant degradation.

Another example of photodegradation and mineralization of RhB by utilizing visible light active Na-doped g-C_3N_4 was reported by Zhang *et al.*[84] Their study includes Na-doped g-C_3N_4 exhibiting a promotional effect in the photoactivity, achieving a RhB degradation rate 3.5 times higher than the pristine g-C_3N_4. This could be ascribed to the incorporation of Na-doping, which facilitated enhanced surface area, a shift in band edge potential, reduced band gap, and the photogenerated charge separation. The mineralization efficiency was determined by estimating the total organic carbon (TOC). The improved mineralization efficiency was attributed to the tuning of the band structure, altering the optical energy level and expanding π-delocalization upon Na doping. As a result, Na-doped g-C_3N_4 exhibited a 3.5-fold enhancement in the RhB degradation rate over pristine g-C_3N_4.

In the next study, Sudrajat *et al.* reported the visible-light-driven photocatalytic mineralization of 17α-ethynylestradiol (EE2) over a highly photo-active Na-doped g-C_3N_4.[85] The Na-doped g-C_3N_4 displayed a remarkable enhancement in the photoactivity compared to the neat g-C_3N_4, achieving 95.7% EE2 degradation with 89.4% mineralization efficiency in the first cycle. This enhancement resulted from electronic modification in g-C_3N_4 induced by Na-doping, which generated a new energy state in between the CB and VB, thereby altering the band structure, facilitating the separation of photogenerated charge carriers, and reducing their recombination. These combined effects drove the superior degradation and mineralization of EE2. The CB of Na-doped g-C_3N_4 favored the conversion of O_2 into $O_2^{\bullet-}$ radicals as the active species. This demonstrated the beneficial role of Na in enhancing EE2 mineralization. Another case study suggested that the incorporation of K in g-C_3N_4 effectively reduced the recombination tendency of excitons and enabled the degradation of naphthalene efficiently.[87] This advancement in photoactivity was primarily attributed to the

cooperative effect of K doping and the integration of biochar. Biochar often acts as a cocatalyst, offering effective charge transportation and open active sites for adsorption of pollutants, providing a promotional effect of dispersion in polar solvents due to its hydrophilic nature. It also functioned as an electron acceptor to mitigate the charge recombination. An optimized mass ratio of K-doped g-C_3N_4/biochar (1 : 0.8) achieved 82.19% naphthalene degradation within 180 min, demonstrating excellent photostability for more than five cycles. Similarly, Zhang *et al.* demonstrated a K-doped g-C_3N_4 photocatalyst for the photo-assisted degradation of MB and phenol.[89] It was found that the K-doping altered the electronic structure as well as improved the overall photocatalytic performance, resulting in a 3.3 and 5.8-fold higher photodegradation activity of MB and phenol, respectively, than pristine g-C_3N_4 (Fig. 28a). By the K incorporation in K-doped g-C_3N_4, the flat band potential was uplifted by 0.2 V, exhibiting an anodic shift in the valence level, which enhanced the oxidizability nature of the photocatalyst for efficient photodegradation activity. Moreover, MB degradation activity increased with increasing 'K' content up to 22%. Later, the photodegradation activity got reduced upon further increasing the K content as more defective sites were generated, which might cause the rapid charge recombination and hinder the condensation process. The smaller arc radius observed in the EIS Nyquist plots (Fig. 28b) indicated the improved charge distribution and transfer efficiency in K-doped g-C_3N_4. This is corroborated by the photocurrent response along with reduced PL intensity (Fig. 28c).

K-doped g-C_3N_4 also exhibited efficient RhB degradation activity under visible light irradiation.[90] The photo-degradation activity followed first-order kinetics with a rate constant of approximately 6.4 times greater than that of neat g-C_3N_4. The enhanced photo-degradation was due to the synergistic effect of K-doping, which increased the surface area, decreased the band gap energy, and promoted easy charge separation. Similarly, Xu *et al.* compared the photodegradation of RhB using various alkali metal-doped (Na, K, Rb, and Cs) g-C_3N_4 samples.[95] Under identical experimental conditions, neat g-C_3N_4 decomposed 45% of RhB in 40 min; in contrast, GCN-Na, GCN-K, GCN-Rb, and GCN-Cs exhibited degradation efficiencies of 16%, 83%, 79%, and 52%, respectively (Fig. 28d). GCN-K demonstrated the most pronounced enhancement in activity among all alkali metal-doped samples. From the analysis of band gap energy and UPS spectra, a negative shift in both CB and VB potentials was detected, which favored the photoreduction process of O_2, generating superoxide radicals ($O_2^{\bullet-}$), along with excellent stability. In contrast, GCN-Na showed the least efficiency, attributed to the negligible structural, optical, and electronic modifications by Na doping (Fig. 28e and f). Another example demonstrated the utilization of an Na, Cl-co-doped photocatalyst in the photodegradation of RhB.[109] The resultant Na, Cl-co-doped g-C_3N_4 (CN–NaCl-0.5) photocatalyst was synthesized by one-step thermal condensation of dicyandiamide and NaCl. The dual incorporation of Na and Cl led to several promotional effects, such as improved crystallinity of the material, increased inter-spacing distance of the adjacent layers, red-shift optical absorption, a

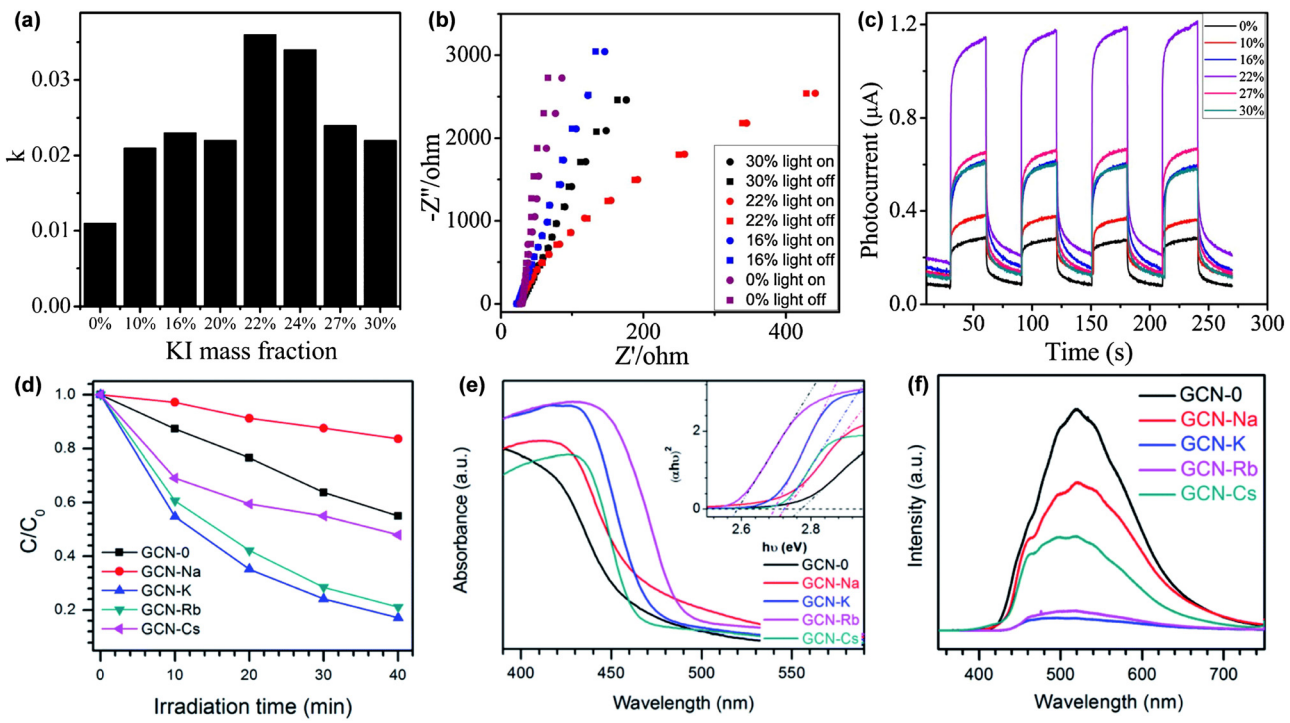

Fig. 28 (a) Rate constants of photocatalytic degradation of phenol, (b) EIS Nyquist plots, and (c) photocurrent responses of pure g-C_3N_4 and K-C_3N_4 with varying KI concentrations. Reproduced with permission from ref. 89. Copyright 2015, Elsevier. (d) Photocatalytic degradation of RhB over the synthesized catalysts, (e) UV-vis DRS spectra, and (f) PL spectra of GCN-0, GCN-Na, GCN-K, GCN-Rb and GCN-Cs samples. Reproduced with permission from ref. 95. Copyright 2017, Royal Society of Chemistry.

narrow band gap with positive shifting of the CB and VB band positions, reduced charge recombination, and better charge separation for maximum photoresponse. As a result, CN–NaCl-0.5 exhibited 97.5% of visible light-mediated RhB degradation in 50 min, whereas neat g-C_3N_4 exhibited a degradation rate of 55.5% only. The next study demonstrated the co-doping of both K and Na into the lattice of g-C_3N_4 for the photodegradation and mineralization of RhB.[189] In this work, melamine was mixed with the different contents of the eutectic mixture of NaCl and KCl (at their melting point ~476 °C) and underwent thermal condensation at 520 °C for 2 h. The resultant K, Na co-doped g-C_3N_4 showed excellent textural properties, due to the template effect of the employed molten solution of NaCl–KCl. Both Na and K were coordinated into the g-C_3N_4 lattice *via* ion–dipole interaction between the alkali metals and triazine moieties of g-C_3N_4. The ionic radii of Na (100 pm) and K (150 pm), which are higher than that of C (70 pm) and N (65 pm), didn't facilitate the substitutional doping; however, the nitrogen pot having an in-planar distance of 0.71 nm facilitated the interstitial doping of Na and K by forming Na–N and K–N binding sites *via* ion–dipole interaction. Furthermore, the band structure was optimized due to the co-doping of Na and K, resulting in a favorable CB and VB edge potential for smooth generation of $O_2^{\bullet-}$ and $^{\bullet}OH$ active intermediates to catalyze the oxidative degradation of RhB, with 10 times higher photoreactivity than pristine g-C_3N_4.

Sun *et al.* reported alkali metal-doped g-C_3N_4 nanosheets (M–CN, M = L, Na, K) synthesized through copolymerization of melamine and alkali metal hydroxides for photocatalytic degradation of organic pollutants.[42] PXRD confirmed the increased interlayer spacing and reduced crystallinity due to alkali ion intercalation. SEM and TEM analyses revealed that doping reduced the grain boundaries and introduced a porous structure, which alters the morphology of g-C_3N_4, thereby enhancing the SSA. This increased SSA of M–CN provides more active sites to facilitate diffusion and mass transfer of reactants. XPS analysis revealed a strong M–N coordination within the g-C_3N_4 framework, altering the electronic structure and charge distribution. UV-vis DRS spectra (Fig. 29a) indicated that M–CN exhibited enhanced visible light absorption and a higher absorbance and tuned the band structure by reducing the band gap and charge carrier recombination, which was demonstrated by PL and TRPL spectra. Transient photocurrent and EIS data further confirmed that K–CN has a superior conductivity and lower charge-transfer resistance. The integration of M^+ into the g-C_3N_4 framework increased the local negative charge density, attracting h^+ and repelling e^-, thereby impeding the

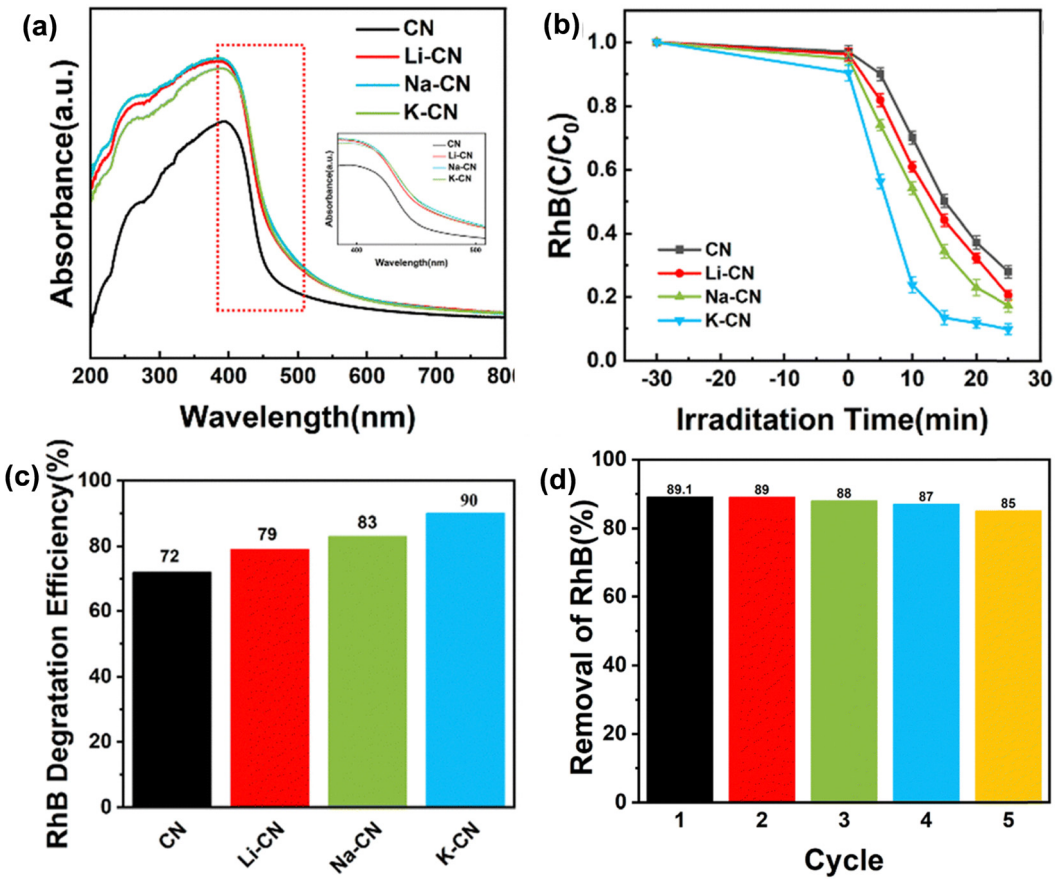

Fig. 29 (a) UV-vis absorption spectra of CN and M–CN samples, (b) photocatalytic degradation kinetics of RhB, (c) comparison of RhB degradation rates by CN and M–CN, and (d) evaluation of catalytic stability of K–CN over five consecutive degradation cycles. Reproduced with permission from ref. 42. Copyright 2024, Royal Society of Chemistry.

photoexcited charge carrier's recombination. These structural, electronic, and optical properties collectively improve the photoactivity of M–CN. The RhB degradation efficiency of all the synthesized catalysts under visible light irradiation followed the order: K–CN (90%), Na–CN (83%), Li–CN (79%), with K–CN exhibiting an enhanced photocatalytic performance and retaining 85% efficiency after 5 cycles, with structural stability (Fig. 29b–d).

Taking advantage of oxygen functionalization, enhanced charge transport through K-intercalation was investigated in the activity of K, O co-doped g-C_3N_4 samples towards photocatalytic NO removal, investigated by Li and coworkers.[190] Due to oriented charge flow across the layers, there is an accumulation of photoelectrons required for the generation of active species for photocatalytic redox reactions. The intercalated K-atom as a mediator exhibited oriented charge transfer to strengthen the interlayer interaction (Fig. 30a). Based on DFT calculations, the band structure of g-C_3N_4 (CN) and O-doped g-C_3N_4 (OCN), as shown in Fig. 30b and c, indicated the role of O atoms as adjusters and K-atoms as a mediator, resulting in a favorable band offset and spatial charge carrier separation. The potential energies of neat g-C_3N_4 and K, O co-doped g-C_3N_4, as shown in Fig. 30d and e, indicated an increase after the incorporation of O and K atoms. This difference in potential energy provides a driving force to transfer e^- between the layers through the K-atom as a channel. Furthermore, the role of O-adjuster atoms was further studied using Bader effective charge analysis, suggesting the change in the local charge density in OCN layers due to the continuous flow of charge from adjacent C and N to the O atom (Fig. 30f and g). This electron accumulation near the O atom and the promotional role of the intercalated K atom could alter the internal vdW force to strengthen the interlayer charge transfer for better charge separation (Fig. 30h and i). Hence, the availability of a greater number of e^- on K, O co-doped g-C_3N_4 samples favored the generation of $O_2^{\bullet-}$ for the photooxidation of NO. Furthermore, according to ref. 39, K-doping in g-C_3N_4 experienced a more positive shifting of the VB edge potential position than Na-doping, and thereby the VB level of K-doped g-C_3N_4 possessed a stronger oxidizability, resulting in a higher NO removal efficiency than Na-doped g-C_3N_4.

One of the major problems in the food industry and drinkable water bodies is the contamination of nitrite (NO_2^-), which usually occurs due to the reckless dumping of various inorganic and organic pollutants into the environment. Moreover, its over-concentration can lead to various potential threats and health hazards to mankind. Therefore, it is absolutely necessary to detect the NO_2^- *via* a facile route. For instance, Na and K-doped g-C_3N_4 was utilized for the electrochemical sensing of NO_2^-.[191] The experimental outcomes suggested that Na-doping created abundant electroactive sites, which were responsible for the highest redox current response, facilitated high conductivity, and very good electron transfer ability that enabled efficient electrochemical oxidation of NO_2^-. Similarly, uranium(VI) contamination is currently becoming a global threat due to the enormous increase in nuclear activity, mining, industrialization, *etc.* Among various decontamination approaches, photocatalytic reduction of a highly soluble U(VI) contaminant to the less soluble U(VI) is a relatively promising approach to mitigate the uranium contamination. For instance, a K-doped, –C≡N functionalized defective g-C_3N_4 (KHCN) photocatalyst was fabricated *via* a facile alkali etching process with KOH for the removal of U(VI).[44] The alkali etching enhanced the SSA of KHCN, which improved the adsorption of uranium, significantly accelerating the photocatalytic process. The XRD analysis revealed a notable attenuation in the intensity of the (002) plane of KHCN, suggesting a reduction in the interplanar stacking distance and diminished crystallinity. Additionally, the (100) plane became Table 5 weaker and broader, indicating structural disorder of tri-*s*-triazine units and the presence of defects in the CN framework. Furthermore, the structural modification due to doping and defect creation was confirmed by SEM, FT-IR, and

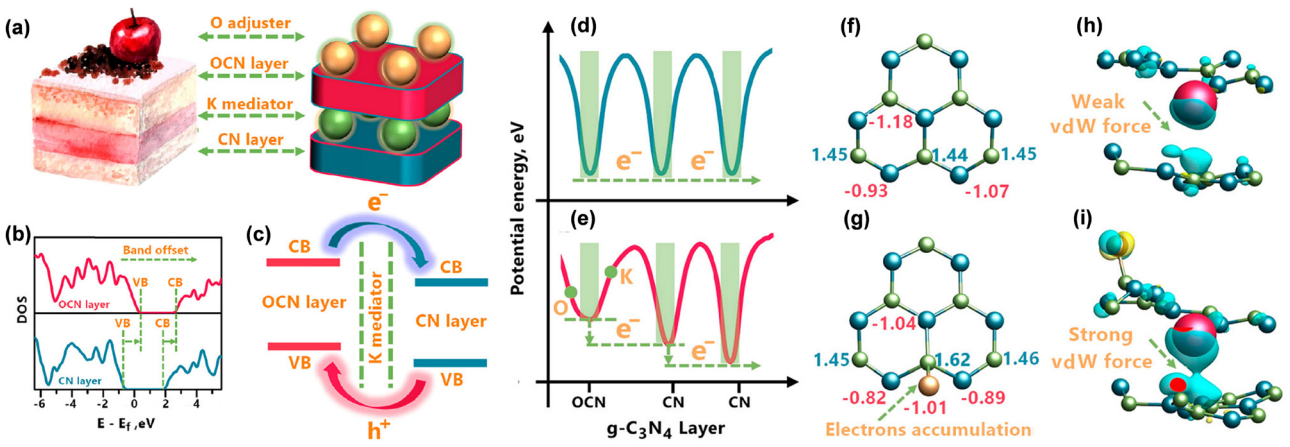

Fig. 30 (a) Schematic representation of the internal van der Waals heterostructure (IVDWH): illustrating the "Cake Model" and structural framework of OCN-K-CN, (b) calculated total density of states (TDOS), (c) band alignment diagram of the OCN-K-CN IVDWH, (d) and (e) layered electrostatic potential distribution, (f) and (g) Bader charge distribution for pristine CN and OCN-K-CN, (h) and (i) charge density difference mapping of K-CN and OCN-K-CN, where blue, green, red, and gold spheres correspond to N, C, K, and O atoms, respectively. Reproduced with permission from ref. 190. Copyright 2018, American Chemical Society.

Table 5 List of alkali metal-doped g-C_3N_4-based photocatalysts for efficient pollutant degradation

Photocatalysts	Precursors	Synthesis method	Reaction condition	Pollutants	% of Degradation	Ref.
K–CN	Melamine, KOH	Thermal polymerization	500 W Xe lamp	RhB	90%	42
LiK15:5	Urea, LiCl, KCl	Calcination	500 W Xe lamp	Methylamine	93.1%	79
KTCN/ZnO NWs	Melamine, KCl, 2,4,6-triaminopyrimidine ($C_4H_7N_5$)	Calcination	Xe lamp	MB	99.25%	192
ZnO/NaTCN	Melamine, NaCl, -triaminopyrimidine ($C_4H_7N_5$), $Zn(CH_3COO)_2{\cdot}2H_2O$	Calcination	Xe lamp	MB	98.54%	193
CsGCN1	DCDA, CsCl	Thermal condensation	20 W CFL bulbs	AR 94 dye	93.4%	115
0.4-PCN	Melamine, K_2CO_3	Thermal polymerization	300 W Xe lamp	RhB, CFH	RhB (93%), CFH (33.4%)	185
K–g-C_3N_4	Melamine, KCl	Thermal polymerization	8 W VUV lamp	TMP	91%	187
3-CN	Urea, $(Fe(NO_3)_3{\cdot}9H_2O)$, $NaNO_3$	Calcination	Dark	MB	100%	188
Ni-MOF/Na–CN-4@MS	Melamine, NaCl, $Ni(NO_3)_2{\cdot}6H_2O$, H_2BDC	Calcination	300 W Xe lamp	MB	99%	194
KPCN/GO/$ZnFe_2O_4$	Melamine, $(NH_4)_2HPO_4$, KCl	Thermal polymerization, hydrothermal	500 W halogen lamp	RhB, MB, TC	RhB (96%), MB (93%), TC (87%)	195

XPS analyses. Compared to CN, KHCN samples exhibited surface corrosion and abundant voids due to –C≡N induced defects. KHCN-2.5 showed a ladder-like thin-layered edge structure, implying partial layer exfoliation, confirmed by TEM. This suggested that –C≡N groups interrupted heptazine growth, forming fragmented nanosheets or debris. PL analysis revealed that KHCN exhibited a reduced intensity compared to pristine CN, indicating suppressed recombination of charge carriers due to the introduction of K^+ ions and –C≡N groups. KHCN also exhibited a red-shift absorption edge compared to CN, extending visible-light absorption due to a narrow band gap (2.28 eV). Furthermore, from XPS-VB spectra, the more negative CB potential of KHCN facilitated the O_2 reduction to $O_2^{\bullet-}$, which favors the formation of an immobilized $(UO_2)O_2{\cdot}2H_2O$ adduct on the catalyst surface to execute the photocatalytic removal of U(VI). Hence, synergistic incorporation of K^+ ions and –C≡N groups in the CN framework effectively augmented the electronic structure, improved charge dynamics, and boosted visible light absorption, enabling superior U(VI) removal efficiency.

In addition to the above examples, several studies on alkali metal-doped–g-C_3N_4-based photocatalysts have demonstrated excellent activity in pollutant degradation and removal of hazardous species as outlined in Table 5.

3.3. Miscellaneous applications

This review also demonstrates how the influence of the alkali metal in g-C_3N_4 can stretch the opportunities in various exciting applications other than solar fuel production and contaminant degradation to justify its practicality. Several research groups have already demonstrated the advantageous aspects of g-C_3N_4 in the photocatalytic oxidation process.[196–203] However, alkali doping further exhibits a promotional impact due to the appropriate band alignment and electron transport channel, which efficiently facilitates the photocatalytic oxidation of various biomass compounds and organic molecules. A binary composite of K intercalated g-C_3N_4 and Bi_2MoO_6 (BMO/K–CN) forming a Z-scheme heterojunction was reported for the oxidation of *para*-methoxybenzyl alcohol under simulated solar irradiation.[204] The successful composite formation was confirmed from the PXRD observation (Fig. 31a). Furthermore, the FESEM analysis suggested the hexagonal Bi_2MoO_6 (BMO) deposited on the lamellar-type sheets of K-doped g-C_3N_4 (K–CN). The successful interfacial contact was confirmed by the XPS analysis, suggesting that K doping occurred in the interstitial position beset with the heptazine unit and coordinated with N as N–K bonding sites, due to which K–CN experienced charge delocalization, encompassing better charge separation. Comparing the O 1s XPS profiles of

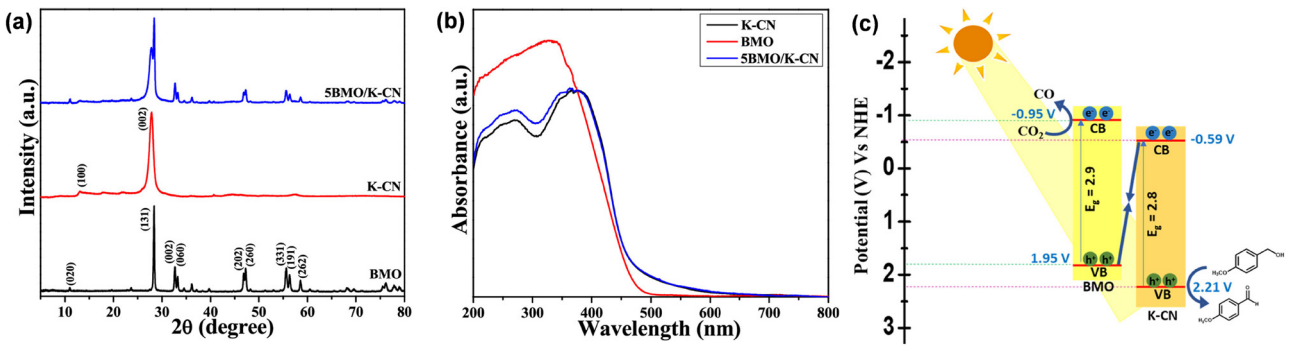

Fig. 31 (a) XRD profile and (b) UV-vis DRS spectra of K–CN, BMO, and 5BMO/K–CN, and (c) picture illustrating the mechanism for CO_2 photoreduction coupled with *p*-MeOBA oxidation over the 5BMO/K–CN photocatalyst. Reproduced with permission from ref. 204. Copyright 2025, American Chemical Society.

K–CN and BMO/K–CN, the latter experienced a down shift, which clearly suggested the chemical interaction of BMO and K–CN. Similarly, after the composite formation, the up shift in the binding energies of C, N, and the down shift in the binding energies of Bi, Mo, and O of BMO/K–CN strongly suggest the flow of e^- from K–CN to BMO in BMO/K–CN. As a result, an appropriate band structure corresponding to the Z-scheme heterojunction of BMO/K–CN was constructed. The Z-scheme heterojunction was further confirmed by the terephthalic acid and DMPO test. BMO/K–CN exhibited red-shift light absorption with respect to BMO but maintained a similar type of light absorption trend with K–CN, as confirmed by the DR UV-vis analysis (Fig. 31b). The large interfacial contact area between BMO and K–CN promoted enhanced electron transfer ability as well as better charge separation efficiency. As a result, BMO/K–CN exhibited a one-pot conversion of *para*-methoxybenzyl alcohol oxidation and CO_2 reduction without any additional oxidant or co-catalyst. BMO/K–CN could be able to achieve 31% *para*-methoxybenzaldehyde as the oxidation product and 21 mmol g^{-1} h^{-1} of CO as the CO_2 reduction product in 6 h under simulated solar light irradiation. All spectroscopic evidence and control experiments suggested that, upon photoexcitation, the photoexcited e^- in the CB of K–CN moved towards the h^+ in the VB of BMO; therefore, the remaining e^- in the CB of BMO utilized in the reduction of CO_2, while the h^+ in the VB of K–CN oxidized *para*-methoxybenzyl alcohol (Fig. 31c).

Another example of efficient photooxidation of substituted benzylamine and simultaneous production of H_2O_2 was demonstrated by Liu *et al.*[116] The K and Na-doped g-C_3N_4 nanosheet (K/Na/PCN) was first synthesized *via* ionothermal polycondensation of KCl, NaCl, and DCDA, in which K and Na ions were stabilized by the N atoms of heptazine units. Being a promising photoactive material with appropriate CB and VB edge potential, cobalt phthalocyanine (CoPc), having a planar structure, efficiently formed a Z-scheme heterojunction with K/Na/PCN through π–π stacking and H-bonding between the hydroxyl units of K/Na/PCN and CoPc (Fig. 32a). The resultant CoPc/K/Na/PCN, having an effective interfacial Z-scheme heterojunction interaction, experienced a strong interfacial intrinsic electric field, which significantly improved the charge carrier separation efficiency and thereby possessed enhanced redox ability of separated charge carriers to execute the efficient photoredox reaction. The photogenerated e^- of CoPc and the h^+ of K/Na doped g-C_3N_4 combined, while the h^+ of VB of CoPc and e^- of CB of the K/Na doped g-C_3N_4 remained separated to be utilized in the reduction of O_2 to $O_2^{\bullet-}$ and abstraction of H^+ from benzyl amine ($PhCH_2NH_2$) to $PhCH_2NH_2^{\bullet+}$ respectively. The $O_2^{\bullet-}$ coupled with H^+ to form H_2O_2, and the resultant $PhCH_2NH_2^{\bullet+}$ further reacted with the h^+ to release another H^+ and formed PhCH═NH as an intermediate species. The PhCH═NH underwent an addition reaction with another molecule of $PhCH_2NH_2$ to form *N*-benzylidenebenzylamine (*N*-BDBA) and NH_3 as the final product (Fig. 32b). Similarly, Dong *et al.* reported a highly efficient alkali-doped g-C_3N_4 photocatalyst, which was enriched with triune active sites such as alkali metal doping, –C≡N linkage, and N-vacancies for efficient ozone activation and atrazine degradation.[72] Na, K and Li doped g-C_3N_4, designated as CN–M, M = Na, K and Li, facilitated the ozone adsorption and exhibited an enhanced electron transfer phenomenon due to the intercalation of alkali metals, which were reported to reduce the layer distance and acted as an electronic bridge. Moreover, the alkali doping created the –C≡N defect and N vacancies in the M–CN framework. The electron-withdrawing effect due to the –C≡N linkage facilitated the light harvesting by modulating the electronic structure, and the N vacancies promoted optimized charge distribution in M–CN. Therefore, the combinational effect of alkali metal doping, –C≡N linkage, and N-vacancies stimulated the M–CN framework for better ozone oxidation and atrazine degradation than undoped g-C_3N_4.

Furfural is a useful biomass-derived platform chemical that acts as a potential precursor for the production of various sustainable chemicals and fuels. The selective oxidation of furfural to furoic acid is an interesting and important transformation due to the wide range of applicability of furoic acid as a building block in the food industry, pharmaceuticals, and biofuel additives. Wang *et al.*[205] and Liu *et al.*[206] demonstrated the photocatalytic approach for furfural oxidation reaction using a composite of K-doped g-C_3N_4 and a photoactive NH_2-UIO-66 MOF ($K_{0.1}$-CN/UN-20). The former used Er doping as the promoter, and the latter used an aqueous solution of Na_2CO_3 externally as the mediator and promoter for the photooxidation process. Er and K doped g-C_3N_4 (Er@K–C_3N_4/UIO-66NH_2) exhibited 90.4% furfural oxidation with 63.4% furoic acid selectivity. The successful formation of the heterostructure and the K and Er doping not only enhanced the light harvesting ability but also promoted the electron transfer process to boost the charge carrier separation efficiently for efficient oxidation reaction (Fig. 33a). Similarly, the type II heterostructure between the K-doped g-C_3N_4 and NH_2-UIO-66 provided a strong interfacial contact in the heterostructure, accelerating excellent electron transfer ability. Again, the strategically tuned band gap width of the resultant heterostructure, when combined with the aqueous solution of Na_2CO_3, efficiently generated the desired reactive oxygen species (ROS) to facilitate the photocatalytic oxidation process of furfural. The photocatalytic process began with the excitation of charge carriers upon light irradiation, and the formation of the interfacial heterojunction promoted the charge separation by exhibiting band bending phenomena due to the generation of an interfacial intrinsic electric field (Fig. 33b). The photoexcited e^- in the CB of K–CN reduced O_2 present in air to $O_2^{\bullet-}$ and subsequently formed H_2O_2 by reacting with aqueous H^+. The *in situ* generated H_2O_2 preferentially oxidized furfural to furoic acid with 70.7% yield, while the Na_2CO_3 avoided the formation of unwanted ROS by selectively quenching the h^+ in the VB of NH_2-UIO-66.

Being a nitrogen-rich material, g-C_3N_4 possesses appropriate basicity and active sites for various types of biomass oxidation reactions and glucose isomerization reaction. The fabrication of alkali-doped g-C_3N_4-based active catalysts can be achieved by a molten salt-assisted synthesis method, which can induce the appropriate basicity in the g-C_3N_4 structure, to potentially

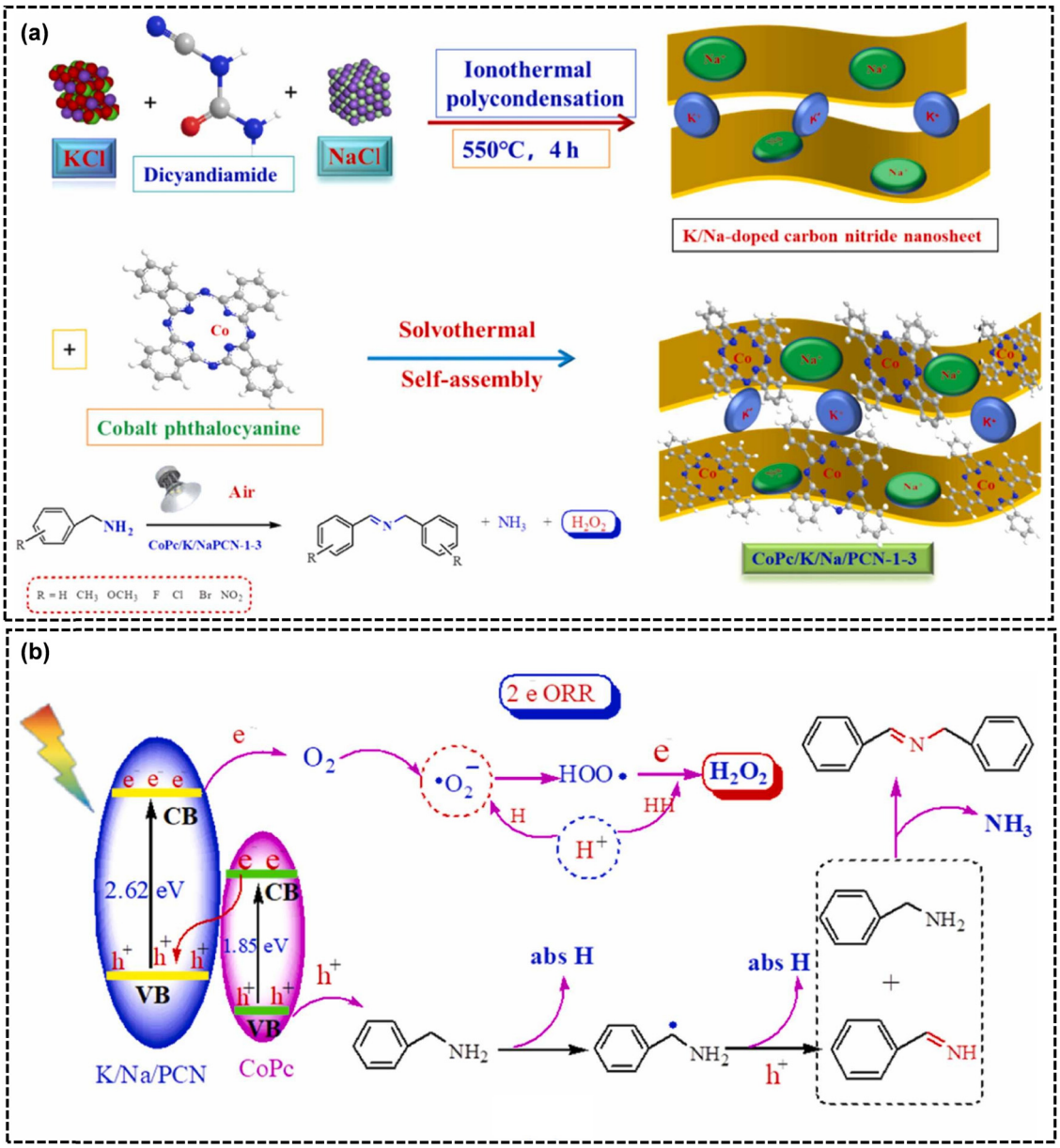

Fig. 32 (a) Schematic depiction of the preparation process and structural configuration of CoPc/K/Na/PCN Z-scheme heterojunction composites and (b) illustration of the proposed mechanism of the photooxidation of benzyl amine to *N*-BDBA. Reproduced with permission from ref. 116. Copyright 2025, Elsevier.

enable the glucose to fructose isomerization reaction.[207] The glucose to fructose isomerization was generally achieved in the presence of the Brønsted basic sites *via* a proton transfer mechanism. Based on this, several alkali metal-doped g-C_3N_4 materials were synthesized *via* the thermal condensation of urea and respective alkali/alkaline metal chlorides, as shown in Fig. 34a. The resultant materials were evaluated for the glucose to fructose isomerization reaction, and the K-doped (K–C_3N_4) and Mg-doped g-C_3N_4 (Mg–C_3N_4) exhibited the best activity in the glucose to fructose transformation. The PXRD and FT-IR analyses indicated the successful doping of alkali metal in g-C_3N_4 (Fig. 34b and c). The CO_2-TPD analysis confirmed that the basicity of the alkali/alkaline-doped material was significantly higher than that of the undoped g-C_3N_4 (Fig. 34d). Among various samples, Mg–C_3N_4 and K–C_3N_4 exhibited a broad CO_2 desorption peak at higher temperature (370–480 °C), suggesting that their stronger basic sites and higher overall basicity chemisorbed the CO_2 molecules. The time and temperature dependent catalytic activity test suggested that the Mg–C_3N_4 exhibited 32.5% fructose yield after 240 min at 90 °C, while Na–C_3N_4, K–C_3N_4, and Ca–C_3N_4 afforded 23.2%, 28.7%, and 28.4%, respectively.

Similarly, another work achieved glucose to fructose isomerization *via* a photocatalytic approach using the Li and K co-doped g-C_3N_4 (CM-molten) synthesized *via* the molten salt-assisted thermal condensation of a melamine-cyanuric acid (MCA) supramolecular precursor (Fig. 35a).[208] For comparison, the MCA

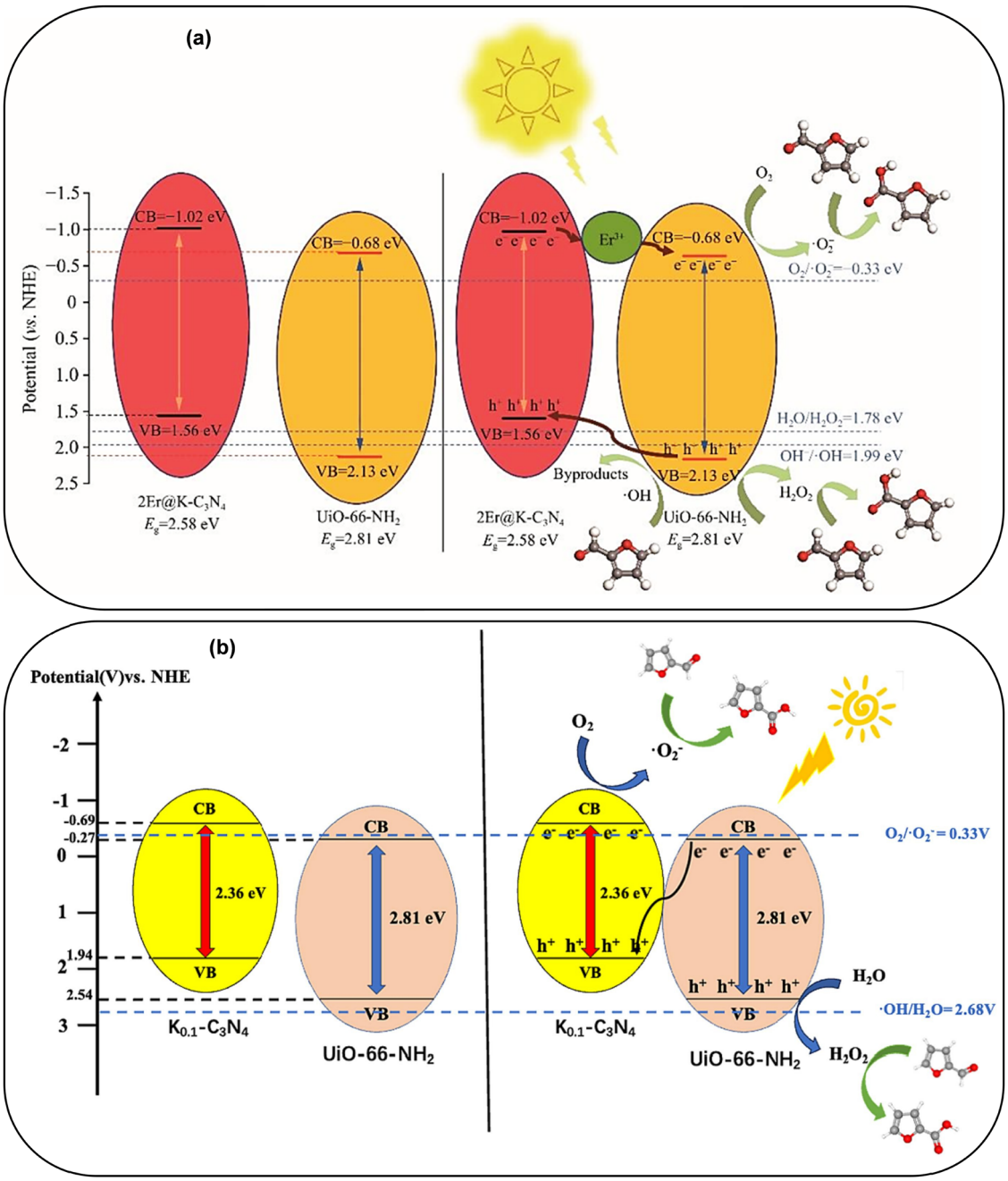

Fig. 33 Schematic illustration of the proposed reaction mechanism of furfural photo-oxidation over (a) Er@K–C_3N_4/UIO-66NH_2. Reproduced with permission from ref. 205. Copyright 2024, Elsevier and (b) $K_{0.1}$-CN/UN-20. Reproduced with permission from ref. 206. Copyright 2024, Elsevier.

supramolecular precursor was also pyrolyzed without the molten salt and designated as CM-air. The effect of the molten salt-driven pyrolysis was studied through several characterization processes. CM-air exhibited small-sized nanosheet morphology, whereas CM-molten exhibited a curled tubular shape consisting of micro-sized nanosheets with high crystallinity, confirmed by the existence of a well-defined (002) crystalline phase (Fig. 35b). High crystallinity of CM-molten was analyzed by PXRD analysis, suggesting the existence of various diffraction planes corresponding to poly(triazine imide). Additionally, the successful intercalation of Li^+ in CM-molten was also validated by the PXRD analysis. In contrast, such crystalline phases were absent in the PXRD pattern CM-air, which demonstrated that the molten-assisted pyrolysis induced a high degree of crystallinity in the material (Fig. 35c). The molten-assisted synthesis was also responsible for the existence of –C≡N linkages, confirmed by the FT-IR and XPS analyses. This resulted in the enhanced light harvesting ability with red shift light absorption and a narrow bandgap energy compared to the CM-air (Fig. 35d). Moreover, these structural changes led to the existence of N vacancies and excess unpaired e^- in CM-molten as confirmed by the EPR analysis (Fig. 35e). As a result of the combinational effect of

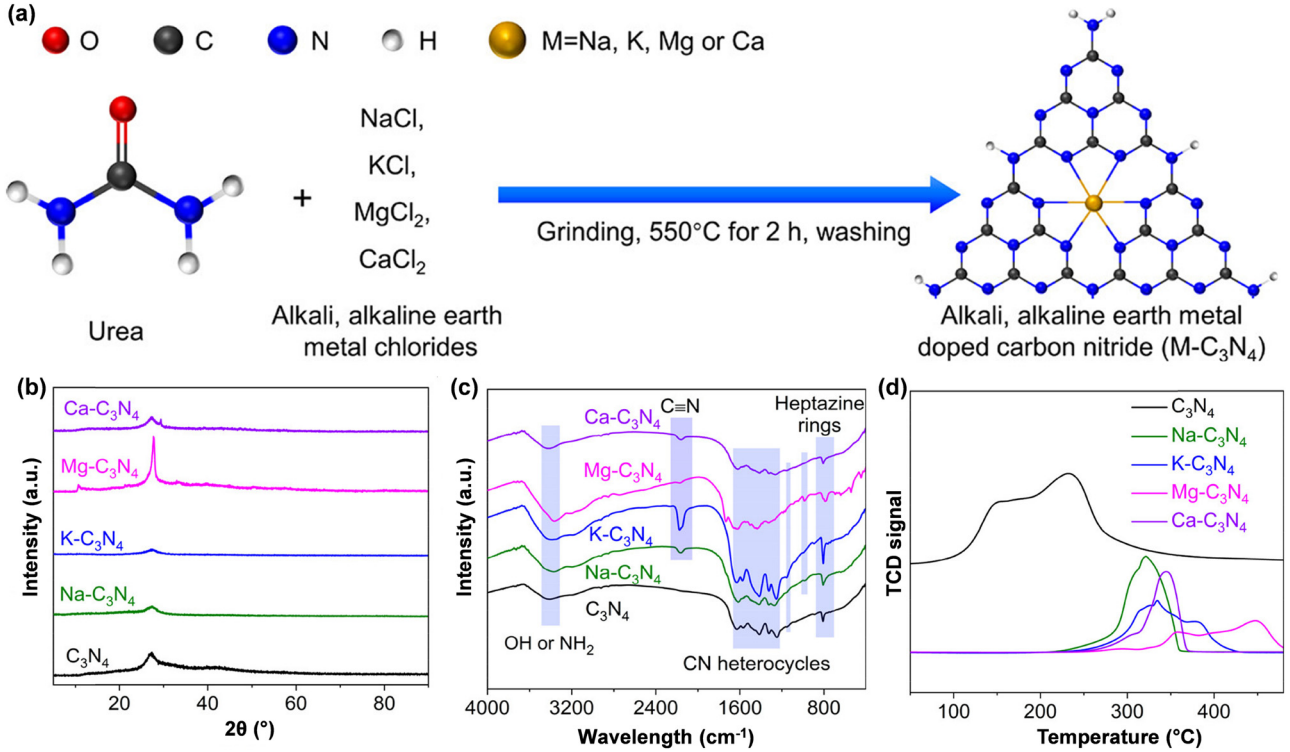

Fig. 34 (a) Diagrammatic illustration of the synthesis of M-C_3N_4, (b) XRD patterns, (c) FT-IR spectra, and (d) CO_2-TPD of all the prepared samples. Reproduced with permission from ref. 207. Copyright 2022, American Chemical Society.

better light harvesting, improved charge separation, and extended functionalities due to the –C≡N linkages and N vacancies, the transient Lewis acid–base active sites could be created in CM-molten to accomplish the photocatalytic glucose to fructose isomerization (more than 25% conversion and ~70% fructose selectivity) under visible light while CM-air exhibited very negligible activity of the glucose isomerization. As a result of the combinational effect of better light harvesting, improved charge separation, extended functionalities due to the –C≡N linkages and N vacancies, an efficient charge transfer pathway was achieved, as demonstrated in Fig. 35f. As a consequence, the transient Lewis acid–base active sites could be created in CM-molten to accomplish the photocatalytic glucose to fructose isomerization (more than 25% conversion and ~70% fructose selectivity) under visible light, while CM-air exhibited very negligible activity of the glucose isomerization. The overall mechanism involved the activation of the aldehyde group by the Lewis acid sites, while the O atom at C-2 was activated by the Lewis base sites, resulting in the formation of an H-bonding intermediate, which further underwent deprotonation and H^+ transfer pathways to produce fructose (Fig. 35g).

Exceptionally, Li, among all the alkali metals, when doped in g-C_3N_4, exhibited excellent hydrogen adsorption efficiency and was suitable for hydrogen storage applications. Thus, Li-doped g-C_3N_4 sheets suitably drove efficient hydrogen adsorption. For instance, based on first-principles calculations on density functional theory, Zhu *et al.* reported the application of Li-doped g-C_3N_4 towards hydrogen storage under ambient thermodynamic conditions.[67] Their study revealed that porous open hollow sites of g-C_3N_4 sheets are found to be favorable to dope Li-atoms by coordinating with the N-atoms. The high electronegativity value of N-atoms not only induces a positive charge on Li-atoms but also polarizes H_2, enabling a strong binding (3.26 eV) with the substrate. The energy of hydrogen adsorption by Li-doped g-C_3N_4 was calculated as 3.48 kcal mol^{-1} and studied as a good system having potential in energy storage. Similarly, another report by Song *et al.* proposed the first principles calculations for the reversible storage of H_2 over a super alkali NLi_4 cluster decorated g-C_3N_4 sheet ($(NLi_4)_2$@g-C_3N_4).[209] The calculation results demonstrated that two NLi_4 'superalkali' clusters stably anchored on a 2 × 2 g-C_3N_4 supercell in $(NLi_4)_2$@g-C_3N_4, having a total binding energy of −4.39 eV, and exhibited a total of 18 H_2 molecules adsorption with an adsorption energy of −0.29 eV at 200 K and 1 atm pressure. Charge analysis indicated that the optimized structure containing the NLi_4 cluster, which accommodated Li as Li^+, temporarily polarized the H_2 and enhanced non-dissociative adsorption without forming strong chemical interactions. However, the temperature-dependent simulations further demonstrated that about 83.3% of the adsorbed H_2 got desorbed at 300 K and 1 atm, demonstrating a temperature-responsive, reversible storage behavior of H_2 that favored uptake at lower temperatures and promoted effective release near room temperature at atmospheric pressure, fulfilling a desirable combination for reversible H_2 storage applications. Besides, Li-doped graphitic carbon nitrides such as (g-C_3N_4 and g-C_4N_3) are also explored in Li ion batteries.[210] Melamine-derived triazine-based g-C_3N_4 having a single-layer nanosheet with a small pore size distribution can accommodate Li single atoms rather than cluster accumulation.

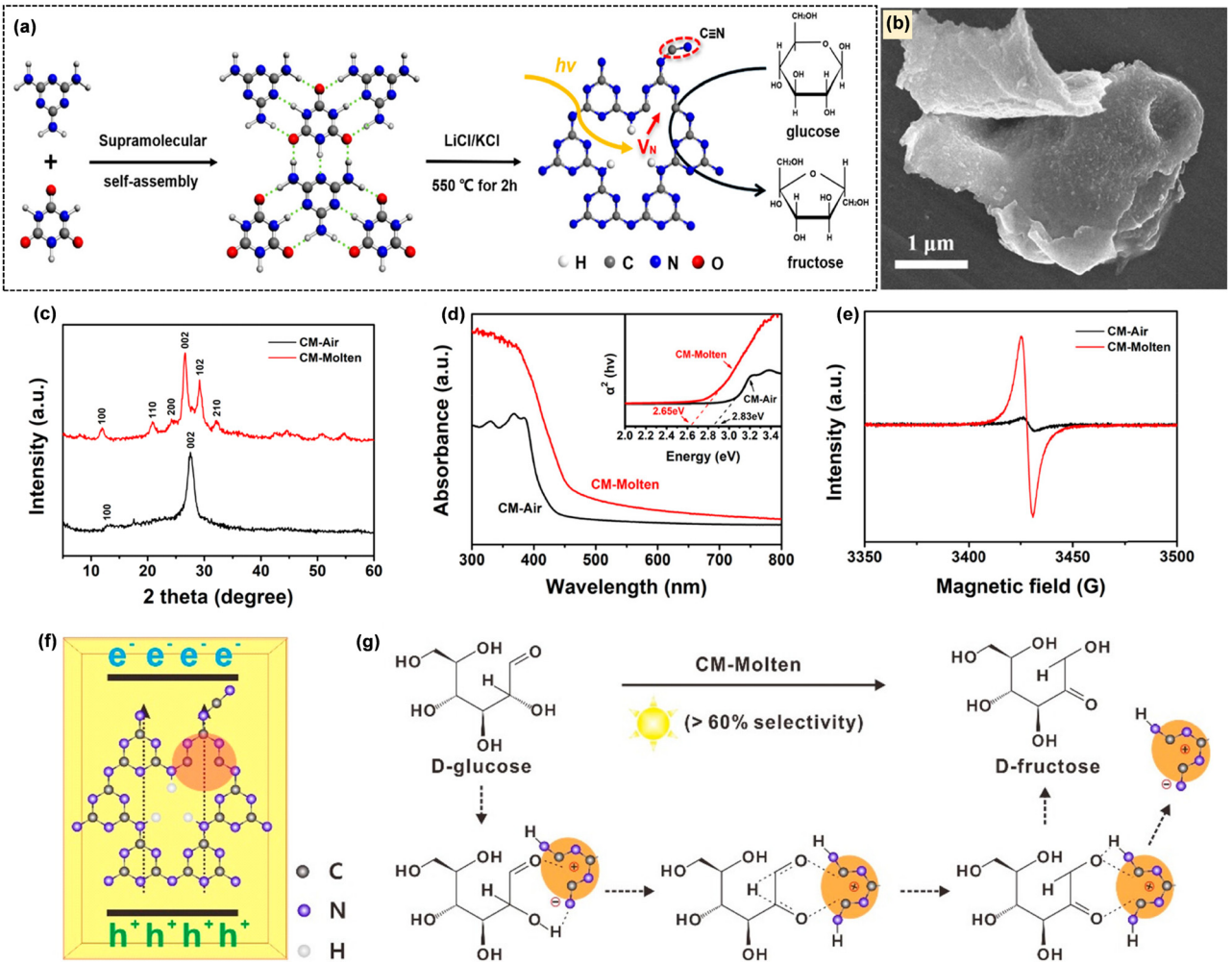

Fig. 35 (a) Schematic representation of CM-molten synthesis *via* supramolecular self-assembly assisted by a molten-salt approach for photocatalytic glucose isomerization, (b) FESEM image of CM-molten, (c) XRD, (d) UV-vis absorption spectra, (e) EPR spectra of CM-air and CM-molten, (f) picture illustrates the enhanced charge separation in CM-molten with oriented N-vacancies and –C≡N functionalities, and (g) glucose-to-fructose isomerization mechanism over CM-molten. Reproduced with permission from ref. 208. Copyright 2021, American Chemical Society.

According to the report, mono-layered Li-doped g-C_3N_4 acted as an anode material, while the bulk Li-doped g-C_4N_3 acted as a cathode material. Optimized Li-doped g-C_3N_4 can adsorb hydrogen in quasi-molecular form, having the H–H distance of 0.76 Å. The distance between the hydrogen molecule and the Li-atom was 2.5 and 2.18 Å in $Li_2C_3N_4$ and $Li_2C_4N_3$ systems, respectively, while the average distance between the H_2 molecule and the Li-atom was 2.86 Å and 2.43 Å. Every Li-atom has a tendency to adsorb three hydrogen molecules. Gravimetric densities of H_2 adsorption over $Li_2C_3N_4$ and $Li_2C_4N_3$ are 10.2 and 10.3 wt%, respectively, whereas the volumetric density is 100.2 g L^{-1} in both cases.

4. Conclusion and future perspectives

This review consolidates current advancements in the design and functional tuning of alkali-metal-modified g-C_3N_4, emphasizing how these dopants reshape its structural, electronic, and photocatalytic behaviour (Fig. 36). The discussion highlights how mono-doping and co-doping have proven highly effective in tailoring the electronic structure, interfacial characteristics, and photoresponse behavior of g-C_3N_4-based materials. Smaller ions tend to substitute into the lattice, while larger ions more commonly intercalate into the layers or occupy cavity sites, generating increased porosity, disturbed stacking, and reduced crystallite size due to modified polycondensation paths. An in-depth demonstration of theoretical modellings and DFT studies is also provided in this review to underscore the charge density distribution, band structure analysis, and charge transfer mechanism, confirming that alkali ion incorporation leads to structural reorganizations that extend the optical absorption to red shift, narrowing the band gap, and optimizing the VB and CB levels for efficient utilization of charge carriers. Simultaneously, nitrogen vacancies are often formed during doping, acting as complementary active sites, enabling more efficient electron migration. By leveraging these synergistic effects, alkali-metal-doped g-C_3N_4 shows considerable promise for various sustainable and environmentally friendly photocatalytic processes, including solar fuel

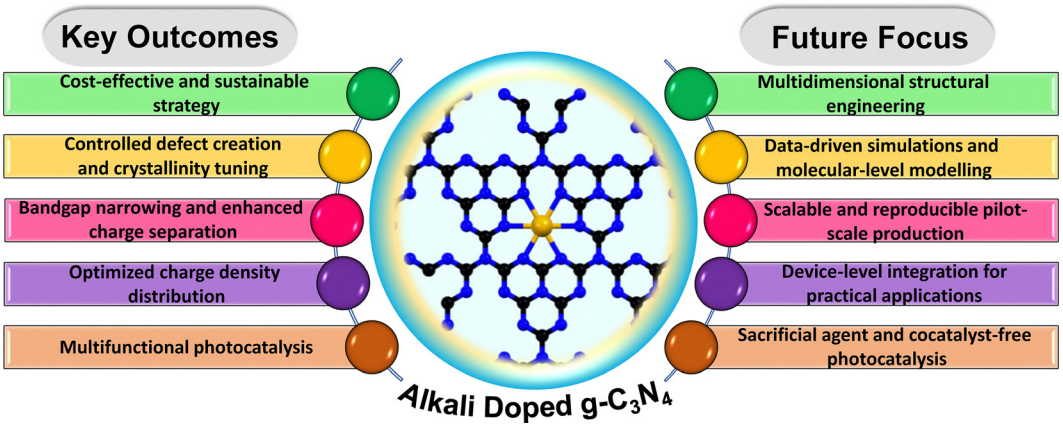

Fig. 36 Schematic depiction of the key outcomes and future prospects of alkali metal-doped g-C_3N_4.

production, organic pollutant decomposition, biomass conversion, and energy-related applications. Insights drawn from case studies integrating morphological analysis, spectroscopic characterization, and mechanistic evaluation underscore the versatility and practical potential of these materials for efficient photocatalysis and energy harvesting. The insights summarized here provide a foundation for rational design of high-performance, energy-efficient photocatalytic systems based on alkali metal-engineered g-C_3N_4 nanostructures. Overall, we trust this review can become a reference tool for the fabrication of advanced and highly efficient alkali-doped g-C_3N_4-based energy harvesting materials.

In contrast, several unsolved hitches and research challenges are highlighted as future prospects for advancing the alkali-doped g-C_3N_4-based photocatalysts in solar energy harvesting applications (Fig. 36). The respective research gaps need to be well addressed by making continuous efforts through extensive research in the domain of alkali doping in g-C_3N_4. Some of the points are highlighted below.

4.1. Rationalization of dopant behaviour

A deeper mechanistic insight into dopant location, bonding environment, and framework stability is needed. Since the appropriate doping of alkali metals provides a polarized charge density distribution for enhanced charge separation efficiency, a thorough investigation of advanced theoretical modellings, DFT calculations, simulations, and machine-learning-assisted design can help to predict the structure–property relationships, guide ideal dopant selection, and minimize trial-and-error experimentation.

4.2. Development of doping databases

Integrating such rationalized results from computational predictions with detailed experimental metadata (selection of precursors, synthesis parameters, defect states, morphology difference, structural outcomes, and photoactivity metrics) into a standardized database platform would accelerate the data-driven rational design of alkali-doped g-C_3N_4. Combining the database with an advanced high-throughput simulation process enables molecular-level estimation of control of dopant sites, structural configurations, photocatalytic performances, and product selectivity while maintaining very high reproducibility.

4.3. Device-level integration

The introduction of alkali metal causes substantial electronic, structural, and interfacial modifications. Moreover, considering the non-toxic, economic, and easily synthesizable nature of alkali metal-doped g-C_3N_4-based materials, it will be advantageous to expand their practical implementation in terms of progressive device design for different types of energy-related applications, such as PC and PEC electrodes, hybrid solar-driven reactors, ion storage and electrochemical energy-storage devices, and membranes, owing to their facile fabrication of device-grade films and composites using various promising techniques (powder suspensions, immobilized thin films and heterostructure formation).

4.4. Multi-parameter structural tuning

Currently, many research groups are continuously working on advancing the structural features of g-C_3N_4-based materials to achieve highly efficient, multifunctionality-integrated energy materials. However, more research is needed to fine-tune the structure and optoelectronic properties through multiple modifications and tailor the morphology to achieve highly efficient alkali-doped g-C_3N_4-based photocatalytic materials with the inherent quality of best photostability. In this regard, it is also crucial to develop a comprehensive database and advanced simulation methodologies that can serve as useful tools for future researchers to engineer at the molecular level of alkali-doped g-C_3N_4 materials, thereby precisely predicting and controlling their structural configurations, photoactivity, and product selectivity.

4.5. Multifunctional active site installation

Semiconductor photocatalysis has the potential to mimic natural photosynthesis; however, the major solar energy conversion process, such as CO_2 reduction, N_2 reduction, and water splitting reaction, often requires co-catalysts or sacrificial agents, which create complexities and difficulties, causing industrial infeasibility. Therefore, it is essential to modulate the structure and optoelectronic parameters in alkali metal-doped g-C_3N_4 to install

multifunctional active sites by rationalizing the co-doping, precise defect management, and modifying physico-chemical properties for efficient solar fuel production with a co-catalyst and sacrificial agent-free condition, which is a more facile, sustainable, and economic pathway.

4.6. Scaling up sustainable synthesis

The development of alkali metal-doped g-C_3N_4 materials *via* a facile molten salt-assisted synthesis approach is one of the most straightforward, cheap, and sustainable approaches to advance the bulk g-C_3N_4. Therefore, it is crucial to optimize and advance this straightforward approach by rationalizing the experimental parameters (experimental conditions, types of precursors, *etc.*), process designing, and reactor modelling for the large-scale synthesis of alkali metal-doped g-C_3N_4-based materials in pilot plants with high reproducibility.

The precursors (melamine, urea, and dicyandiamide) used for the preparation of alkali metal-doped g-C_3N_4 are abundantly available and are of low-cost. Likewise, the synthesis process involves an energy-efficient one-pot thermal co-polymerization method, which involves simple equipment and a continuous feed process, demonstrating the high scalability. But the homogeneous distribution of alkali metals and the formation of ammonia gas during synthesis on a large scale is a challenge. Compared to the other doping systems, such as non-metal doping associated with control synthesis, transition metal doping attributed to the toxicity and leaching issues, alkali-metal-doped g-C_3N_4 ranks the best among various modification strategies, for industrial scale-up.

4.7. Collaboration and cross-disciplinary

Furthermore, it is essential to perform multi-collaborative research to strengthen future research by fabricating these structurally modified functionally rich alkali metal-doped g-C_3N_4 based materials using solar cell technologies for sustainable energy production applications.

Author contributions

Pratikshya Dash and Sulagna Patnaik share equal contribution for conceptualization, draft writing – review and editing; Sonali Panda and Bhagyashree Priyadarshini Mishra: review and editing: Kulamani Parida: supervision and review.

Conflicts of interest

There are no conflicts to declare.

Data availability

This review article only utilizes data assessment of the published articles by various researchers in this domain, which can be found from the sources referenced in the manuscript. No new data were generated during the preparation of this review. The required copyright permission has also been taken.

Acknowledgements

All the authors are thankful to Siksha 'O' Anusandhan (Deemed to be University) management for providing the necessary facilities and their constant support and motivation.

References

1 M. R. Hoffmann, S. T. Martin, W. Choi and D. W. Bahnemann, *Chem. Rev.*, 1995, **95**, 69–96.
2 A. L. Linsebigler, G. Lu and J. T. Yates Jr, *Chem. Rev.*, 1995, **95**, 735–758.
3 C. Gao, J. Low, R. Long, T. Kong, J. Zhu and Y. Xiong, *Chem. Rev.*, 2020, **120**, 12175–12216.
4 J. L. Holechek, H. M. Geli, M. N. Sawalhah and R. Valdez, *Sustainability*, 2022, **14**, 4792.
5 S. Parida and D. P. Dutta, in *Biorenewable Nanocomposite Materials, Vol. 1: Electrocatalysts and Energy Storage*, ed. D. Pathania and L. Singh, ACS Symposium Series, American Chemical Society, Washington, DC, 2022, vol. 1410, pp. 307–366.
6 A. Behera, A. K. Kar and R. Srivastava, *Mater. Horiz.*, 2022, **9**, 607–639.
7 M. Ashraf, M. Ayaz, M. Khan, S. F. Adil, W. Farooq, N. Ullah and M. Nawaz Tahir, *Energy Fuels*, 2023, **37**, 6283–6301.
8 A. D. A. Bin Abu Sofian, H. R. Lim, H. Siti Halimatul Munawaroh, Z. Ma, K. W. Chew and P. L. Show, *Sustain. Dev.*, 2024, **32**, 3953–3978.
9 B. Weng, M.-Y. Qi, C. Han, Z.-R. Tang and Y.-J. Xu, *ACS Catal.*, 2019, **9**, 4642–4687.
10 S.-K. Lee, A. Mills and C. O'Rourke, *Chem. Soc. Rev.*, 2017, **46**, 4877–4894.
11 F. Wang, Q. Li and D. Xu, *Adv. Energy Mater.*, 2017, **7**, 1700529.
12 K. Mishra, N. Devi, S. S. Siwal, V. K. Gupta and V. K. Thakur, *Adv. Sustainable Syst.*, 2023, **7**, 2300095.
13 P. Kumari, N. Bahadur, L. Kong, L. A. O'Dell, A. Merenda and L. F. Dumée, *Mater. Adv.*, 2022, **3**, 2309–2323.
14 S. S. Mani, S. Rajendran, T. Mathew and C. S. Gopinath, *Energy Adv.*, 2024, **3**, 1472–1504.
15 A. Balapure, J. R. Dutta and R. Ganesan, *RSC Appl. Mater. Interfaces*, 2024, **1**, 43–69.
16 F. Chen, T. Ma, T. Zhang, Y. Zhang and H. Huang, *Adv. Mater.*, 2021, **33**, 2005256.
17 M. Liras and M. Barawi, *Chem. Soc. Rev.*, 2019, **48**, 5454–5487.
18 L. Ding, Z.-D. Yu, X.-Y. Wang, Z.-F. Yao, Y. Lu, C.-Y. Yang, J.-Y. Wang and J. Pei, *Chem. Rev.*, 2023, **123**, 7421–7497.
19 P. Reiss, E. Couderc, J. De Girolamo and A. Pron, *Nanoscale*, 2011, **3**, 446–489.
20 S. Ma, L. Jiang, W. Yang, F. Liu, D. Wang, F. Wang and J. Huang, *Mater. Today Sustain.*, 2025, **29**, 101023.
21 J. Fu, J. Yu, C. Jiang and B. Cheng, *Adv. Energy Mater.*, 2018, **8**, 1701503.
22 B. P. Mishra and K. Parida, *J. Mater. Chem. A*, 2021, **9**, 10039–10080.
23 J. Wang and S. Wang, *Coord. Chem. Rev.*, 2022, **453**, 214338.

24 X. Qian, W. Li, X. Wang, H. Guan, Q. Bao, B. Zhao, B. Wulan, S. Liu, D. Zhu and X. Feng, *Adv. Funct. Mater.*, 2025, **35**, 2416946.
25 P. Dash, A. K. Kar, R. Srivastava and K. Parida, *Mater. Horiz.*, 2025, **12**, 6485–6557.
26 M. A. Khan, S. Mutahir, I. Shaheen, Y. Qunhui, M. Bououdina and M. Humayun, *Coord. Chem. Rev.*, 2025, **522**, 216227.
27 F. He, Z. Wang, Y. Li, S. Peng and B. Liu, *Appl. Catal., B*, 2020, **269**, 118828.
28 X. Liu, R. Ma, L. Zhuang, B. Hu, J. Chen, X. Liu and X. Wang, *Crit. Rev. Environ. Sci. Technol.*, 2021, **51**, 751–790.
29 M. Rizwan, A. Zada, S. Azizi, P. Fazil, M. Naeem, G. Murtaza, N. A. Ibrahim, N. S. Basher, Z. Liu and M. H. Eisa, *Int. J. Hydrogen Energy*, 2025, **97**, 1126–1152.
30 W. Zhang, D. Xu, F. Wang and M. Chen, *Nanoscale Adv.*, 2021, **3**, 4370–4387.
31 Y. Pang, P. Li, X. Ma, L. Sun, Y. Liu, D. Qu, L. An and Z. Sun, *EES Catal.*, 2023, **1**, 810–831.
32 Y. Zhang, J. Hou, J. Hu, H. Yu, M. Xu, Q. Chen, L. Liu, W. Yan and L. Shi, *Appl. Surf. Sci.*, 2025, 164223.
33 C. Ma, Z. Hu, T. Zhao, Z. Gu, Q. Yuan and B. Chen, *J. Mater. Chem. B*, 2025, **13**, 7528–7553.
34 X. Zhang, T. Li, C. Hu, X. Yan, K. Qiao and Z. Chen, *Nanomaterials*, 2022, **12**, 2929.
35 Z. Gu, M. Jin, X. Wang, R. Zhi, Z. Hou, J. Yang, H. Hao, S. Zhang, X. Wang and E. Zhou, *Catalysts*, 2023, **13**, 192.
36 A. Akhundi, A. Zaker Moshfegh, A. Habibi-Yangjeh and M. Sillanpää, *ACS EST Engg.*, 2022, **2**, 564–585.
37 J. Chen, S. Fang, Q. Shen, J. Fan, Q. Li and K. Lv, *Catalysts*, 2022, **12**, 962.
38 H. M. Tofil, R. Ghazi, F. A. Ghaib, R. N. Dara, I. Kebaili, I. Boukhris, H. Ding and Z. Rehman, *Sustainable Energy Fuels*, 2025, **9**, 2900–2927.
39 T. Xiong, W. Cen, Y. Zhang and F. Dong, *ACS Catal.*, 2016, **6**, 2462–2472.
40 L. Chen, S. Ning, R. Liang, Y. Xia, R. Huang, G. Yan and X. Wang, *Int. J. Hydrogen Energy*, 2022, **47**, 14044–14052.
41 X. Zhong, Y. Zhu, M. Jiang, Q. Sun and J. Yao, *Energy Fuels*, 2023, **37**, 5448–5456.
42 X. Sun, G. Zhao, S. Li, J. Liu and M. Huang, *New J. Chem.*, 2024, **48**, 9231–9242.
43 R. Mandal and S. Bhattacharyya, *J. Phys. Chem. C*, 2024, **128**, 17342–17352.
44 Z. Dai, L. Chen, W. Zhang, B. Liang, Y. Gao and L. Li, *Sep. Purif. Technol.*, 2024, **338**, 126537.
45 J. Jiang, S. Cao, C. Hu and C. Chen, *Chin. J. Catal.*, 2017, **38**, 1981–1989.
46 P. Haripriya, T. Anjana, K. Sreelakshmi, N. T. Madhu, M. Anjana, P. V. Suneesh and D. V. R. Kumar, *Catal. Commun.*, 2024, **187**, 106909.
47 H. Liang, A. Wang, R. Cheng, F. Chen, P. Kannan, C. Molochas and P. Tsiakaras, *Chem. Eng. J.*, 2024, **489**, 151145.
48 J. Wu, J. Yu, F. Fan, R. Li, M. Wang, G. Li, Y. Wang, Y. Cui, D. Liu and Y. Wang, *Green Chem. Eng.*, 2025, **6**, 388–397.
49 N. Bai, J. Yin, X. Huo, Y. Ma, D. Guo and A. Wang, *ScienceAsia.*, 2022, **48**, 202.
50 H. Liang, J. Zhao, A. Brouzgou, A. Wang, S. Jing, P. Kannan, F. Chen and P. Tsiakaras, *J. Colloid Interface Sci.*, 2025, **677**, 1120–1133.
51 V. Bem, M. C. Neves, M. R. Nunes, A. J. Silvestre and O. C. Monteiro, *J. Photochem. Photobiol. Chem.*, 2012, **232**, 50–56.
52 M. Qamar, C. R. Yoon, H. J. Oh, N. H. Lee, K. Park, D. H. Kim, K. S. Lee, W. J. Lee and S. J. Kim, *Catal. Today*, 2008, **131**, 3–14.
53 A. Turki, H. Kochkar, C. Guillard, G. Berhault and A. Ghorbel, *Appl. Catal., B*, 2013, **138**, 401–415.
54 S. Patnaik, D. P. Sahoo and K. Parida, *Carbon*, 2021, **172**, 682–711.
55 Y. Yang, W. Niu, L. Dang, Y. Mao, J. Wu and K. Xu, *Front. Chem.*, 2022, **10**, 955065.
56 D. Liu, A. Barbar, T. Najam, M. S. Javed, J. Shen, P. Tsiakaras and X. Cai, *Appl. Catal., B*, 2021, **297**, 120389.
57 B. Li, T. Tian, Y. Zheng, D. Jiang, G. Xu, Y. Sun, Z. Li and Y. Yuan, *Chem. – Eur. J.*, 2025, **31**, e202500297.
58 J. Li, F. Xing, S. Liu, Z. Xiong, C. Wang, N. Li, H. Jin, Y. Su, C. Feng and J. Li, *J. Colloid Interface Sci.*, 2025, 138565.
59 J. Li, W. Cui, Y. Sun, Y. Chu, W. Cen and F. Dong, *J. Mater. Chem. A*, 2017, **5**, 9358–9364.
60 T. T. H. Nguyen, M. C. Le and N. N. Ha, *Mol. Simul.*, 2021, **47**, 10–17.
61 Y. Xia, H. Yang, W. Ho, B. Zhu and J. Yu, *Appl. Catal., B*, 2024, **344**, 123604.
62 X. Wei, J. Shen, Z. Chen, H. Li, K. Zong, L. Yang, M. Jin, Z. Chen, X. Wang and Z. Chen, *Int. J. Hydrogen Energy*, 2025, **161**, 150465.
63 H. Yu, R. Shi, Y. Zhao, T. Bian, Y. Zhao, C. Zhou, G. I. Waterhouse, L.-Z. Wu, C.-H. Tung and T. Zhang, *Adv. Mater.*, 2017, **29**, 1605148.
64 L. Zhu, X. Ma, N. Liu, G. Xu and C. Huang, *Acta Phys.-Chim. Sin.*, 2016, **32**, 2488–2494.
65 C. C. Nnadiekwe, U. Mustapha, I. Abdulazeez, K. Alhooshani and A. A. Al-Saadi, *Surf. Interfaces*, 2023, **38**, 102852.
66 Q. Zhang, B. Wang, H. Miao, J. Fan, T. Sun and E. Liu, *Chem. Eng. J.*, 2024, **482**, 148844.
67 G. Zhu, K. Lü, Q. Sun, Y. Kawazoe and P. Jena, *Comput. Mater. Sci.*, 2014, **81**, 275–279.
68 Z. Shu, Y. Wang, W. Wang, J. Zhou, T. Li, X. Liu, Y. Tan and Z. Zhao, *Int. J. Hydrogen Energy*, 2019, **44**, 748–756.
69 N. Jasni, A. Iqbal, M. N. Ahmad, H. Pauzi and M. H. Hussain, *Mater. Today Proc.*, 2022, **57**, 1154–1161.
70 B. Liu, X. Nie, Y. Tang, S. Yang, L. Bian, F. Dong, H. He, Y. Zhou and K. Liu, *Langmuir*, 2021, **37**, 4859–4868.
71 Y. Zhang, S. Zong, C. Cheng, J. Shi, X. Guan, Y. Lu and L. Guo, *Int. J. Hydrogen Energy*, 2018, **43**, 13953–13961.
72 S. Dong, L. Liu, W. Xu, H. Cheng, Z. He, J. Tang, D. Wang, L. Wang, S. Song and J. Ma, *ACS EST Engg.*, 2024, **4**, 3105–3117.
73 H. Li, Q. Wei, K. Lu, R. Tang, Z. Xiao, X. Liu, X. Cheng, P. Han, Z. Wang and N. Shang, *Appl. Surf. Sci.*, 2024, **643**, 158712.
74 W. Wang, P. Xu, M. Chen, G. Zeng, C. Zhang, C. Zhou, Y. Yang, D. Huang, C. Lai and M. Cheng, *ACS Sustainable Chem. Eng.*, 2018, **6**, 15503–15516.

75 J. Hu, X. Wu, X. Kong, S. Uemura, T. Kusunose, Y. Tanaka and Q. Feng, *J. Mater. Chem. A*, 2025, **13**, 11605–11616.
76 X.-J. Lu, C.-Z. Yuan, S. Chen, J.-H. Li, I. Ullah, M. Qi and A.-W. Xu, *Langmuir*, 2024, **40**, 11067–11077.
77 Q. Qi, Y. Li, H. Liu, B. Li, H. Wang, Y. Lu, W. Gao, Y. Tian, B. Guo and X. Jia, *Appl. Catal., B*, 2022, **319**, 121864.
78 J. Tang, C. Guo, T. Wang, X. Cheng, L. Huo, X. Zhang, C. Huang, Z. Major and Y. Xu, *Carbon Neutralization*, 2024, **3**, 557–583.
79 P. Xiong, Q. Li, Q. Tang, H. Wang and Z. Wu, *RSC Adv.*, 2023, **13**, 31820–31834.
80 S. A. Rawool, Y. Kar and V. Polshettiwar, *Mater. Adv.*, 2022, **3**, 8449–8459.
81 L. Yuan, W. Liu and W. Zhang, *Environ. Sci. Pollut. Res.*, 2023, **30**, 58276–58281.
82 L. Ruan, G. Xu, L. Gu, C. Li, Y. Zhu and Y. Lu, *Mater. Res. Bull.*, 2015, **66**, 156–162.
83 W. Ma, X. Wang, F. Zhang, X. Fei, X. Zhang, H. Ma and X. Dong, *Mater. Res. Bull.*, 2017, **86**, 72–79.
84 J. Zhang, S. Hu and Y. Wang, *RSC Adv.*, 2014, **4**, 62912–62919.
85 H. Sudrajat, *J. Solid State Chem.*, 2018, **257**, 26–33.
86 F. Guo, J. Chen, M. Zhang, B. Gao, B. Lin and Y. Chen, *J. Mater. Chem. A*, 2016, **4**, 10806–10809.
87 F. Li and M. Lin, *Int. J. Environ. Res. Public Health*, 2020, **17**, 2065.
88 Y. Wang, S. Zhao, Y. Zhang, J. Fang, Y. Zhou, S. Yuan, C. Zhang and W. Chen, *Appl. Surf. Sci.*, 2018, **440**, 258–265.
89 M. Zhang, X. Bai, D. Liu, J. Wang and Y. Zhu, *Appl. Catal., B*, 2015, **164**, 77–81.
90 S. Hu, F. Li, Z. Fan, F. Wang, Y. Zhao and Z. Lv, *Dalton Trans.*, 2015, **44**, 1084–1092.
91 S. Wang, J. Zhan, K. Chen, A. Ali, L. Zeng, H. Zhao, W. Hu, L. Zhu and X. Xu, *ACS Sustainable Chem. Eng.*, 2020, **8**, 8214–8222.
92 J. Fan, H. Wang, G. Liao, C. Song and J. Zou, *Sci. China: Technol. Sci.*, 2025, **68**, 1620206.
93 C. Ye, P. Guo, X. Chen, Z. Zhang, Y. Guo, Z. Chen, H. Yang, D. Luo and X. Liu, *Battery Energy*, 2025, **4**, 20240033.
94 B. Aoudi, J. Kahkeci, I. Sánchez-Montes, Y. Boluk and M. G. El-Din, *Sep. Purif. Technol.*, 2025, **364**, 132523.
95 Y. Xu, Y. Gong, H. Ren, W. Liu, L. Niu, C. Li and X. Liu, *RSC Adv.*, 2017, **7**, 32592–32600.
96 H. Zhang, Y. Tang, Z. Liu, Z. Zhu, X. Tang and Y. Wang, *Chem. Phys. Lett.*, 2020, **751**, 137467.
97 X. Leng, Y. Li, G. Xu, R. Ramaraghavulu, S. V. P. Vattikuti, N. Nguyen Dang and J. Shim, *J. Alloys Compd.*, 2025, **1039**, 182808.
98 G. Fu, W. Zhen, H. Wang, X. Zhou, L. Yang and J. Zhang, *Molecules*, 2024, **29**, 5339.
99 W. Guo, J. Zhang, G. Li and C. Xu, *Appl. Surf. Sci.*, 2019, **470**, 99–106.
100 Y. Wu, W. Xu, Z. Wang, Y. Wang, Y. Zhang, W. Zhong, H.-L. Cai and X. S. Wu, *Appl. Surf. Sci.*, 2021, **542**, 148620.
101 Y. Wu, D. Yang, W. Xu, R. Song, M. Li, Y. Wang, B. Zhou, N. Wu, W. Zhong and H. Cai, *Appl. Catal., B*, 2020, **269**, 118848.
102 K.-L. Chen, S.-S. Zhang, J.-Q. Yan, W. Peng, D.-P. Lei and J.-H. Huang, *Int. J. Hydrogen Energy*, 2019, **44**, 31916–31929.
103 J.-M. Lee, Y.-J. Lee, J. H. Lee, R. Tan, J.-S. Kim, I. S. Cho, S.-J. Park and C.-G. Lee, *Environ. Res.*, 2025, **264**, 120314.
104 F. Bi, G. Ba, J. Yu, H. Hu, J. Ye and D. Wang, *Nanomaterials*, 2025, **15**, 1021.
105 J. Gao, X. Lin, B. Jiang, H. Zhang and Y. Li, *Hydrogen*, 2025, **6**, 45.
106 Q. Qian, X. Chen, G. Li, C. Zhang, Q. Bi and S. Xu, *Appl. Surf. Sci.*, 2025, **709**, 163839.
107 J. Yuan, N. Tian, Z. Zhu, W. Yu, M. Li, Y. Zhang and H. Huang, *Chem. Eng. J.*, 2023, **467**, 143379.
108 X. Xia, C. Xie, Q. Che and P. Yang, *Langmuir*, 2023, **39**, 1250–1261.
109 K.-L. Wang, Y. Li, T. Sun, F. Mao, J.-K. Wu and B. Xue, *J. Mater. Sci.: Mater. Electron.*, 2019, **30**, 4446–4454.
110 J. Duhan, A. Bisht, H. Kumar and S. Obrai, *Surf. Interfaces*, 2024, **52**, 104927.
111 D. Wang, S. Pu, Y. Chen, K. Lei, Y. Duan, L. Mao, X. Zeng, X. Luo, Y. Zhang, Y. Dong, J. Z. Zhang and Y. Sun, *Sci. China: Chem.*, 2025, **68**, 192–200.
112 N. Wahab, M. Shahab, M. U. Haq, A. U. Rahman, M. Israr, Z. Iqbal, R. Khan and A. Ali, *Mater. Res. Bull.*, 2026, **194**, 113801.
113 L. Yan, H. Gao and Y. Chen, *ACS Appl. Nano Mater.*, 2021, **4**, 7746–7757.
114 B. Debnath, S. Singh, S. M. Hossain, S. Krishnamurthy, V. Polshettiwar and S. Ogale, *Langmuir*, 2022, **38**, 3139–3148.
115 A. Kumar, S. Kashyap, M. Sharma and V. Krishnan, *Chemosphere*, 2022, **287**, 131988.
116 Y.-A. Liu, J.-F. You, Q.-X. Shi, X.-Z. Li, J.-R. Xia and Y.-H. Yang, *Appl. Catal. Gen.*, 2025, **689**, 120005.
117 H. Shen, M. Li, W. Guo, G. Li and C. Xu, *Appl. Surf. Sci.*, 2020, **507**, 145086.
118 Y. Wang, M. Wang, X. Zhang, X. Pan, Y. Cui, D. Liu, Y. Wang and W. Yao, *J. Catal.*, 2024, **440**, 115807.
119 D. K. Gorai, S. K. Kuila, A. Kumar, Md. I. Ahmad and T. K. Kundu, *Appl. Surf. Sci.*, 2023, **623**, 157031.
120 M. Fronczak, E. Tálas, Z. Pászti, G. P. Szijjártó, J. Mihály, A. Tompos, P. Baranowski, S. K. Tiwari and M. Bystrzejewski, *Diamond Relat. Mater.*, 2022, **125**, 109006.
121 H. Lu, X. Li, F. Li, X. Xu, R. Zhao, C. Xiong, Q. Hu, Z. Miao and M. Tian, *J. Mol. Liq.*, 2022, **352**, 118655.
122 J. Zheng, Z. Xu, S. Xin, B. Zhu and L. Nie, *Dalton Trans.*, 2022, **51**, 12883–12894.
123 D. R. Paul, R. Sharma, S. Singh, P. Singh, P. Panchal, A. Sharma, P. Devi and S. P. Nehra, *Int. J. Hydrogen Energy*, 2023, **48**, 37746–37761.
124 H. Yang, Y. Zhou, Y. Wang, S. Hu, B. Wang, Q. Liao, H. Li, J. Bao, G. Ge and S. Jia, *J. Mater. Chem. A*, 2018, **6**, 16485–16494.
125 B. Zhu, B. Cheng, L. Zhang and J. Yu, *Carbon Energy*, 2019, **1**, 32–56.
126 M. Z. Rahman and C. B. Mullins, *Acc. Chem. Res.*, 2019, **52**, 248–257.
127 X. Li, C. Zhang, J. Geng, S. Zong and P. Wang, *Molecules*, 2025, **30**, 630.

128 Y. Miseki and K. Sayama, *Adv. Energy Mater.*, 2019, **9**, 1801294.
129 A. Mishra, A. Mehta, S. Basu, N. P. Shetti, K. R. Reddy and T. M. Aminabhavi, *Carbon*, 2019, **149**, 693–721.
130 V. Hasija, A. Kumar, A. Sudhaik, P. Raizada, P. Singh, Q. Van Le, T. T. Le and V.-H. Nguyen, *Environ. Chem. Lett.*, 2021, **19**, 2941–2966.
131 A. Augustin, P. Ganguly, S. Shenoy, C. Chuaicham, S. C. Pillai, K. Sasaki, A. F. Lee and K. Sekar, *Adv. Sustainable Syst.*, 2024, **8**, 2400321.
132 S. Sun, J. Li, J. Cui, X. Gou, Q. Yang, Y. Jiang, S. Liang and Z. Yang, *Int. J. Hydrogen Energy*, 2019, **44**, 778–787.
133 J. Ma, W. Zhou, X. Tan and T. Yu, *Nanotechnology*, 2018, **29**, 215706.
134 M. Ma, J. Li, X. Zhu, K. Liu, K. Huang, G. Yuan, S. Yue, Z. Wang and S. Qu, *Carbon Energy*, 2024, **6**, e447.
135 Y. Guo, Q. Liu, Z. Li, Z. Zhang and X. Fang, *Appl. Catal., B*, 2018, **221**, 362–370.
136 W. Fang, J. Liu, L. Yu, Z. Jiang and W. Shangguan, *Appl. Catal., B*, 2017, **209**, 631–636.
137 S. Cao, Q. Huang, B. Zhu and J. Yu, *J. Power Sources*, 2017, **351**, 151–159.
138 Q.-H. Zhu, Z. Chen, L.-N. Tang, Y. Zhong, X.-F. Zhao, L.-Z. Zhang and J.-H. Li, *Int. J. Hydrogen Energy*, 2019, **44**, 27704–27712.
139 N. S. Lewis, *Science*, 2016, **351**, aad1920.
140 K. Zhong, P. Sun and H. Xu, *Small*, 2025, **21**, 2310677.
141 S. A. Fors and C. A. Malapit, *ACS Catal.*, 2023, **13**, 4231–4249.
142 D. Li, K. Wang, J. Li, Z. Li, H. Wang and Y. Wang, *Nano Energy*, 2025, **133**, 110460.
143 R. J. Detz, J. N. H. Reek and B. C. C. Van Der Zwaan, *Energy Environ. Sci.*, 2018, **11**, 1653–1669.
144 X. Chang, T. Wang and J. Gong, *Energy Environ. Sci.*, 2016, **9**, 2177–2196.
145 Z. Kovacic, B. Likozar and M. Hus, *ACS Catal.*, 2020, **10**, 14984–15007.
146 K. Lai, Y. Sun, N. Li, Y. Gao, H. Li, L. Ge and T. Ma, *Adv. Funct. Mater.*, 2024, **34**, 2409031.
147 T. Wang, J. Lu, J. Chen, C. Wang, K. Li and Y. Mei, *Catal. Sci. Technol.*, 2025, **15**, 2938–2949.
148 H. Li and J. Sun, *ACS Appl. Mater. Interfaces*, 2021, **13**, 5073–5078.
149 S. Liu, J. Yu, X. Chen, N. Li and Q. Zhou, *Nanomaterials*, 2025, **15**, 1294.
150 R. Fang, Z. Yang, Z. C. Kadirova, Z. He, Z. Wang, J. Ran and L. Zhang, *Appl. Surf. Sci.*, 2022, **598**, 153848.
151 J. Wang, Y. Wang, G. Li, Y. Xiong, M. Zhang, S. Zhang and Q. Zhong, *J. Colloid Interface Sci.*, 2021, **603**, 210–219.
152 Z. Yong and T. Ma, *Angew. Chem.*, 2023, **135**, e202308980.
153 L. Wang, J. Zhang, Y. Zhang, H. Yu, Y. Qu and J. Yu, *Small*, 2022, **18**, 2104561.
154 Y. An, T. Cai, W. Jiang, T. Lei and H. Pang, *Green Chem.*, 2025, **27**, 10478–10509.
155 J. Song, C. Li, X. Zhang, P. Ma and K. Zheng, *ACS Catal.*, 2025, **15**, 9058–9088.
156 S. Gou, C. Wang, Z. Gong, Q. Wang, X. Li, X. Chen, J. Wang, J. Ma and Y. Zhu, *Sep. Purif. Technol.*, 2025, **354**, 128829.
157 Z. Liu, X. Wang, P. Zhang, H. Zhang, S. Wang, G. Jiao, W. Wu and M. Wu, *Chem. – Eur. J.*, 2025, **31**, e202404003.
158 C. Zhuang, Y. Chang, W. Li, S. Li, P. Xu, H. Zhang, Y. Zhang, C. Zhang, J. Gao, G. Chen, T. Zhang, Z. Kang and X. Han, *ACS Nano*, 2024, **18**, 5206–5217.
159 S. Zhou, S. Cheng, J. Han and M. Huang, *New J. Chem.*, 2023, **47**, 19063–19076.
160 S. Wu, H. Yu, S. Chen and X. Quan, *ACS Catal.*, 2020, **10**, 14380–14389.
161 Y. Pan, X. Liu, W. Zhang, B. Shao, Z. Liu, Q. Liang, T. Wu, Q. He, J. Huang and Z. Peng, *Chem. Eng. J.*, 2022, **427**, 132032.
162 M. Saniya, S. Shaheen, I. Sadiq and T. Ahmad, *Small*, 2025, **21**, 2505991.
163 T. Žibert, B. Likozar and M. Huš, *ChemSusChem*, 2024, **17**, e202301730.
164 S. L. Foster, S. I. P. Bakovic, R. D. Duda, S. Maheshwari, R. D. Milton, S. D. Minteer, M. J. Janik, J. N. Renner and L. F. Greenlee, *Nat. Catal.*, 2018, **1**, 490–500.
165 G. Zhang, Y. Li, C. He, X. Ren, P. Zhang and H. Mi, *Adv. Energy Mater.*, 2021, **11**, 2003294.
166 K. Ithisuphalap, H. Zhang, L. Guo, Q. Yang, H. Yang and G. Wu, *Small Methods*, 2019, **3**, 1800352.
167 G. Qing, R. Ghazfar, S. T. Jackowski, F. Habibzadeh, M. M. Ashtiani, C.-P. Chen, M. R. Smith III and T. W. Hamann, *Chem. Rev.*, 2020, **120**, 5437–5516.
168 S. Lin, X. Zhang, L. Chen, Q. Zhang, L. Ma and J. Liu, *Green Chem.*, 2022, **24**, 9003–9026.
169 Z. Wang, X. Hu, Z. Liu, G. Zou, G. Wang and K. Zhang, *ACS Catal.*, 2019, **9**, 10260–10278.
170 P. Praus, *ChemistrySelect*, 2023, **8**, e202204511.
171 L. Zhang, S. Hou, T. Wang, S. Liu, X. Gao, C. Wang and G. Wang, *Small*, 2022, **18**, 2202252.
172 L. Li, P. Zhang, N. Li, T. Reyila, Y. Yu, X. Su, C. Peng and L. Han, *J. Environ. Chem. Eng.*, 2024, **12**, 112142.
173 G. Gu, K. Wang, N. Xiong, Z. Li, Z. Fan, S. Hu and X. Zou, *Dalton Trans.*, 2019, **48**, 5083–5089.
174 Y. Li, B. Wang, Q.-J. Xiang, Q. Zhang and G. Chen, *Dalton Trans.*, 2022, **51**, 16527–16535.
175 X. Chang, H. Fan, S. Zhu, L. Lei, X. Wu, C. Feng, W. Wang and L. Ma, *Ceram. Int.*, 2023, **49**, 6729–6738.
176 W. Li, Z. Hu, L. Song, Y. Lv, J. Liu, C. Lu and C. Xu, *ChemistryOpen*, 2025, **14**, e202400431.
177 A. Singh, U. Alam, P. Chakraborty, B. Sundararaju and N. Verma, *Chem. Eng. J.*, 2023, **454**, 140303.
178 X. Tantai, Q. Zhou, L. Shi, M. Wu, P. Sun and X. Dong, *ACS Appl. Nano Mater.*, 2025, **8**, 19001–19011.
179 C.-W. Bai, L.-L. Liu, J.-J. Chen, F. Chen, Z.-Q. Zhang, Y.-J. Sun, X.-J. Chen, Q. Yang and H.-Q. Yu, *Nat. Commun.*, 2024, **15**, 4718.
180 L. Xu, L. Li, Z. Hu and J. C. Yu, *J. Catal.*, 2023, **418**, 300–311.
181 X. Yang, Y. Ye, J. Sun, Z. Li, J. Ping and X. Sun, *Small*, 2022, **18**, 2105089.
182 Y. Luo, Y. Zhu, Y. Han, H. Ye, R. Liu, Y. Lan, M. Xue, X. Xie, S. Yu, L. Zhang, Z. Yin and B. Gao, *Carbon Res.*, 2023, **2**, 14.
183 Z. Tong, D. Yang, T. Xiao, Y. Tian and Z. Jiang, *Chem. Eng. J.*, 2015, **260**, 117–125.

184 J. Xu, Z. Wang and Y. Zhu, *ACS Appl. Mater. Interfaces*, 2017, **9**, 27727–27735.
185 B. He, M. Feng, X. Chen, Y. Cui, D. Zhao and J. Sun, *Appl. Surf. Sci.*, 2022, **575**, 151695.
186 L. Wang, H. Yang, Q. Wu and R. Ma, *Int. J. Hydrogen Energy*, 2024, **80**, 495–506.
187 W. Lu, A. Wang, Y. Zhang, S. Ren and Z. Zhang, *Chem. Eng. J.*, 2024, **495**, 153192.
188 S. Meng and Z. Nan, *Sep. Purif. Technol.*, 2023, **309**, 123026.
189 J. Zhao, L. Ma, H. Wang, Y. Zhao, J. Zhang and S. Hu, *Appl. Surf. Sci.*, 2015, **332**, 625–630.
190 J. Li, Z. Zhang, W. Cui, H. Wang, W. Cen, G. Johnson, G. Jiang, S. Zhang and F. Dong, *ACS Catal.*, 2018, **8**, 8376–8385.
191 P. Jigyasa and J. K. Rajput, *J. Electroanal. Chem.*, 2020, **878**, 114605.
192 J. Xing, Z. Liu, Z. Ruan, J. Lou, X. Yang and B. Huang, *J. Mol. Struct.*, 2025, **1348**, 143536.
193 Z. Liu, Z. Ruan, X. Yang, Y. Huang and J. Xing, *Molecules*, 2024, **29**, 3240.
194 Z. Cao, H. Wu, S. Zhang, B. Zhai, Z. Qian, T. Wang, X. Zhou and C. Wang, *J. Colloid Interface Sci.*, 2026, **704**, 139312.
195 R. Kumar, A. Sudhaik, Sonu, P. Raizada, V.-H. Nguyen, Q. Van Le, T. Ahamad, S. Thakur, C. M. Hussain and P. Singh, *Chemosphere*, 2023, **337**, 139267.
196 M. Bellardita, E. I. García-López, G. Marcì, I. Krivtsov, J. R. García and L. Palmisano, *Appl. Catal., B*, 2018, **220**, 222–233.
197 X. Luo, B. Li, T. Su, X. Xie, Z. Qin and H. Ji, *ACS Catal.*, 2025, **15**, 1097–1111.
198 C. Xing, G. Yu, T. Chen, S. Liu, Q. Sun, Q. Liu, Y. Hu, H. Liu and X. Li, *Appl. Catal., B*, 2021, **298**, 120534.
199 C. Xiao, L. Zhang, H. Hao and W. Wang, *ACS Sustainable Chem. Eng.*, 2019, **7**, 7268–7276.
200 M. J. Lima, P. B. Tavares, A. M. T. Silva, C. G. Silva and J. L. Faria, *Catal. Today*, 2017, **287**, 70–77.
201 X. Sun, D. Jiang, L. Zhang and W. Wang, *Appl. Catal., B*, 2018, **220**, 553–560.
202 Q. Yang, T. Wang, Z. Zheng, B. Xing, C. Li and B. Li, *Appl. Catal., B*, 2022, **315**, 121575.
203 Y. Geng, D. Chen, N. Li, Q. Xu, H. Li, J. He and J. Lu, *Appl. Catal., B*, 2021, **280**, 119409.
204 A. Verma, D. K. Chauhan and K. Kailasam, *ACS Sustainable Chem. Eng.*, 2025, **13**, 46–55.
205 H. Wang, L. Liu, J. Bian and C. Li, *J. Fuel Chem. Technol.*, 2024, **52**, 1617–1628.
206 L. Liu, L. Wang, J. Tan, C. Yu, J. Bian and X. Wang, *J. Photochem. Photobiol. Chem.*, 2024, **451**, 115484.
207 M. Laiq Ur Rehman, Q. Hou, X. Bai, Y. Nie, H. Qian, T. Xia, R. Lai, G. Yu and M. Ju, *ACS Sustainable Chem. Eng.*, 2022, **10**, 1986–1993.
208 J. Wang, H. Zhao, B. Zhu, S. Larter, S. Cao, J. Yu, M. G. Kibria and J. Hu, *ACS Catal.*, 2021, **11**, 12170–12178.
209 Y. Song, M. Hu, X. Liu, H. Cheng and Y. Li, *Int. J. Hydrogen Energy*, 2024, **83**, 512–519.
210 M. Wu, Q. Wang, Q. Sun and P. Jena, *J. Phys. Chem. C*, 2013, **117**, 6055–6059.